Technische Universität München
TUM School of Engineering and Design

Flame Dynamics Investigation of the Lean Burnout Zone of an RQL Combustion Chamber

Julian Benedict Renner

Vollständiger Abdruck der von der TUM School of Engineering and Design der Technischen Universität München zur Erlangung eines

Doktors der Ingenieurwissenschaften (Dr.–Ing.)

genehmigten Dissertation.

Vorsitz:
Prof. Dr.-Ing. Christian Stemmer
Prüfer*innen der Dissertation:
1. Prof. Dr.-Ing. Thomas Sattelmayer
2. Prof. Dr. Nicolas Noiray, Ph.D.

Die Dissertation wurde am 11.04.2023 bei der Technischen Universität München eingereicht und durch die TUM School of Engineering and Design am 25.07.2023 angenommen.

Vorwort

Die vorliegende Arbeit entstand während meiner Tätigkeit als wissenschaftlicher Mitarbeiter am Lehrstuhl für Thermodynamik der Technischen Universität München im Rahmen des Projekts ViFlumiLu, mit Förderung des Bundesministeriums für Wirtschaft und Technologie (BMWi), unter dem Förderkennzeichen 20E1715. Die Forschung wurde innerhalb der Programmlinie "Ökoeffizientes Fliegen" durchgeführt, und für die finanzielle Unterstützung möchte ich an dieser Stelle meinen Dank aussprechen.

Mein besonderer Dank gilt meinem Doktorvater, Herrn Professor Dr.-Ing. Thomas Sattelmayer, der mir die Möglichkeit gegeben hat, diese Arbeit erfolgreich abzuschließen. Vielen Dank für Ihr Vertrauen und Ihre wertvollen fachlichen Impulse. Ebenso danke ich Herrn Dr.-Ing. Christoph Hirsch für den intensiven fachlichen Austausch und seine Unterstützung in allen Aspekten meiner akademischen Entwicklung.

Herrn Professor Dr. Nicolas Noiray danke ich herzlich für die Übernahme des Koreferats sowie die gründliche und zeitnahe Begutachtung meiner Arbeit. Herrn Professor Dr.-Ing. Christian Stemmer möchte ich ebenfalls für die Übernahme des Prüfungsvorsitzes danken.

Für die freundschaftliche Zusammenarbeit danke ich allen aktuellen und ehemaligen Kollegen des Lehrstuhls von Herzen. Ich bin dankbar, nicht nur Kollegen, sondern auch Freundschaften gefunden zu haben. Besonderer Dank gilt meinem Projektkollegen Martin March, mit dem ich viele Höhen und Tiefen durchleben durfte. Gemeinsam konnten wir einen modularen und zuverlässigen Prüfstand aufbauen und die Herausforderungen unseres Forschungsprojekts erfolgreich bewältigen. Danke für deine kollegiale Zusammenarbeit und deinen ausgeprägten Ordnungssinn im Labor. Ebenso möchte ich Moritz Merk und Philip Bonnaire für unsere intensiven Diskussionen, insbesondere am Ende meiner Promotion, danken.

Weiterhin gilt mein Dank allen Studierenden und wissenschaftlichen Hilfskräften, die an diesem Forschungsprojekt beteiligt waren. Vielen Dank für euren unermüdlichen Einsatz und die vielen Stunden, die ihr gemeinsam mit mir im Labor verbracht habt. Besonders möchte ich Jan-Andre Rosenkranz, Thuy An Do und Dominik König hervorheben, die durch ihre exzellenten Leistungen einen wesentlichen Beitrag zu dieser Arbeit geleistet haben. Es erfüllt mich mit Freude zu sehen, dass alle drei ebenfalls eine wissenschaftliche Laufbahn mit einer Promotion eingeschlagen haben.

Nicht zuletzt möchte ich der Mechanischen und der Elektrischen Werkstatt für ihre wertvolle Unterstützung beim Prüfstandsaufbau und den damit verbundenen praktischen Arbeiten danken. Ebenso gebührt Helga Bassett und Sigrid Schulz-Reichwald mein Dank für ihre Hilfe und Beratung in allen verwaltungstechnischen Aufgaben und dafür, dass sie die Mühlen des Lehrstuhls am Laufen halten.

Meinen Eltern und meiner Familie möchte ich von Herzen für ihre kontinuierliche Unterstützung und ihren unerschütterlichen Rückhalt danken. Sie haben nicht nur die Grundlage für meine Ausbildung geschaffen, sondern mir auch zu der starken charakterlichen Basis verholfen, die es mir ermöglichte, diese Arbeit zu verfassen. Von der ersten Station meiner Bildungsreise bis zur letzten haben sie mich ermutigt und begleitet. Ihre bedingungslose Unterstützung war ein entscheidender Faktor für meinen Erfolg.

Abschließend möchte ich meiner Jasmin meinen tiefsten Dank aussprechen. Sie hat mich während dieser langen Reise durch dick und dünn begleitet, mich ertragen und getragen. Ihre unermüdliche Unterstützung und ihre positiven Einflüsse haben mir stets die guten und schönen Seiten des Lebens aufgezeigt. Danke, meine Liebe!

Stephanskirchen, im September 2023 Julian Renner

Abstract

The current study focuses on elucidating the flame dynamics in the lean burnout zone of a Rich-Quench-Lean (RQL) combustion chamber. The lean burnout zone is spatially separated from the rich primary zone, and its thermoacoustic response to velocity fluctuations is investigated independently using a novel experimental approach.

The combustor dynamic response to acoustic forcing from the primary zone and the mixing air jets is characterized using the multi-microphone method. The lean secondary zone is treated as an acoustic 3-port network element connected to a 2-port flame element. Heat release fluctuations due to velocity fluctuations are described by two linear superimposed flame transfer functions (FTFs) as a function of the velocity fluctuations. The FTFs are extracted from the experimental data obtained from non-reacting and reacting measurements and compared with those obtained using chemiluminescence acquired with photomultiplier tube.

It is observed that the inverse diffusion flame in the burnout zone responds to velocity fluctuations from the primary zone in the low-frequency range, with a clear low-pass behavior. The mixing air jets velocity fluctuations produce a more broadband response resulting from an additional crossflow-to-jet-nozzle-coupling. The FTFs calculated from chemiluminescence match well with those obtained using the acoustic method.

In fuel-rich combustion, the secondary zone contributes to approximately $10 - 25\%$ of the total heat release, with most of the heat being released in the primary zone. The influence of the secondary zone on the overall system dynamics can be weighted according to its heat release rate relative to the primary zone, which leads to a relatively minor contribution of the secondary zone to the combined system dynamics.

Kurzfassung

Die vorliegende Studie fokussiert sich auf die Untersuchung der Flammendynamik in der mageren Ausbrandzone einer Rich-Quench-Lean (RQL)-Brennkammer. Durch eine räumliche Trennung von der fetten Primärzone kann ihr thermoakustisches Verhalten als Reaktion auf Geschwindigkeitsschwankungen mithilfe eines neuartigen experimentellen Ansatzes unabhängig untersucht werden.

Zur Charakterisierung der dynamischen Reaktion der Flamme auf akustische Einflüsse aus der Primärzone und den Mischluftlöchern wird die Multi-Mikrofon-Methode verwendet. Die magere Sekundärzone wird dabei als akustisches 3-Tor Netzwerkelement betrachtet, welches mit einem 2-Tor Rankine-Hugoniot Flammenelement verbunden ist. Die Wärmefreisetzungsschwankungen werden durch zwei überlagerte lineare Flammentransferfunktionen (FTFs) beschrieben, die als Funktion der Geschwindigkeitsschwankungen extrahiert werden. Basierend auf experimentellen Daten von nicht-reagierenden und reagierenden Messungen werden die FTFs ermittelt und mit denjenigen verglichen, die über die Chemilumineszenz mittels Photomultiplier gemessen wurden.

Es wird beobachtet, dass die inverse Diffusionsflamme in der Ausbrandzone auf Geschwindigkeitsschwankungen aus der Primärzone im niederfrequenten Bereich mit einem deutlichen Tiefpassverhalten reagiert. Die Geschwindigkeitsschwankungen an den Mischluftlöchern

erzeugen hingegen eine breitbandigere Reaktion, die aus einer zusätzlichen Kopplung von Querströmung zu Mischluftlöchern resultiert. Die FTFs, die mittels der akustischen Methode ermittelt wurden, stimmen gut mit denen überein, die aus der Chemilumineszenz berechnet wurden.

Die Ergebnisse zeigen, dass die Sekundärzone, bei einer brennstofffreichen Verbrennung in der Primärzone, zu etwa $10 - 25\%$ der gesamten Wärmefreisetzung beiträgt, wobei der Großteil der Wärme in der Primärzone freigesetzt wird. Der Einfluss der Sekundärzone auf die Gesamtsystemdynamik kann entsprechend ihrer Wärmefreisetzungsrate im Verhältnis zur Primärzone gewichtet werden, was zu einem vergleichsweise geringen Beitrag der Sekundärzone zur kombinierten Systemdynamik führt.

Contents

List of Figures

List of Tables

Nomenclature

Latin Letters

A	[m^2]	Area
c	[m/s]	Speed of sound
c_p	[J/(kg·K)]	Specific heat capacity at constant pressure
c_v	[J/(kg·K)]	Specific heat capacity at constant volume
$\mathbb{C}$	[ ]	Design constant
C_{ent}	[ ]	Entrainment rate constant
d	[m]	Diameter
f	[Hz]	Frequency
f	[ ]	Mixture fraction
$\widehat{f}, \widehat{g}$	[m/s]	Characteristic waves - Riemann invariants
h	[J/kg]	Enthalpy
$\mathbf{H}$	[ ]	Coefficient matrix
i	[ ]	Imaginary unit
I	[J/m^2]	Intensity
$\mathbf{I}$	[ ]	Identity matrix
J	[ ]	Momentum flux ratio
$k^{\pm}$	[rad/m]	Wave number
l	[m]	Length
L_F	[m]	Flame length
m	[kg]	Mass
$\dot{m}$	[kg/s]	Massflow rate
M	[ ]	Mach number
n	[ ]	Number of mixing air jets
$\mathbf{n}$	[ ]	Normal vector
p	[Pa]	Pressure

$\dot{q}_V$	[J/(m^3· s)]	Volumetric heat release rate
$\dot{Q}$	[W/m^2]	Heat release rate
r	[m]	Radius
$\mathbb{R}$	[J/(kg·K)]	Specific gas constant
R	[ ]	Velocity ratio
R_{ij}	[ ]	Reflection coefficient of scattering matrix
$R_{in,out}$	[ ]	Reflection coefficient at boundary
S	[ ]	Density ratio
Sr	[ ]	Strouhal number
Sc_t	[ ]	Turbulent Schmidt number
s	[J/(kg·K)]	Entropy
s_{norm}	[ ]	Standard deviation
t	[s]	Time
T_{ij}	[ ]	Transmission coefficient of scattering matrix
T	[K]	Temperature
$\mathbf{u}$	[m/s]	Velocity vector
u	[m/s]	Velocity in x direction
V	[m^3]	Volume
x_{COG}	[ ]	Center of gravity
x, y, z	[m]	Spatial coordinate
Z	[kg/(m^2·s)]	Impedance

Greek Letters

α_c	[ ]	Entrainment constant
β_c	[ ]	Entrainment constant
γ	[ ]	Ratio of specific heats
Γ	[ ]	Design factor JIC
δ	[ ]	Relative error
λ	[ ]	Air ratio
ρ	[kg/m^3]	Density
τ	[s]	Time delay
ϕ	[ ]	Arbitrary transport variable

ϕ	[ ]	Equivalence ratio
φ	[rad]	Phase angle
ω	[rad/s]	Real valued angular frequency
Ω	[ ]	Coordinate transformation matrix

Superscripts

$(\,)'$	Temporal perturbation
$\bar{(\,)}$	Temporally averaged field quantity
$\hat{(\,)}$	(Complex valued) spatial oscillation field
$(\,)^A$	Forcing location upstream
$(\,)^B$	Forcing location downstream
$(\,)^C$	Forcing location side
$(\,)^{fg}$	fg- Notation of matrix
$(\,)^\dagger$	Pseudo-inverse
$(\,)^{pu}$	pu- Notation of matrix
$(\,)^T$	Transposed

Indices

$(\,)_0$	Reference state
$(\,)_{\mathrm{I,II}}$	Jet row I and II
$(\,)_{2\times2}$	2×2 matrix
$(\,)_{\mathrm{2p}}$	2-port
$(\,)_{3\times3}$	3×3 matrix
$(\,)_{\mathrm{3p}}$	3-port
$(\,)_{\mathrm{B}}$	Burner
$(\,)_{\mathrm{CC}}$	Combustion chamber
$(\,)_{\mathrm{c/cold}}$	Cold
$(\,)_{\mathrm{con}}$	Convective velocity
$(\,)_{\mathrm{d}}$	Downstream
$(\,)_{\mathrm{eff}}$	Effective

$(\,)_{f}$	Forcing
$(\,)_{h/hot}$	Hot
$(\,)_{i}$	Intermediate state
$(\,)_{id}$	Ideal
$(\,)_{in}$	In-going state
$(\,)_{jet}$	Jet state
$(\,)_{...,M}$	MISO approach FTF
$(\,)_{max}$	Maximum
$(\,)_{min}$	Minimum
$(\,)_{mix}$	Mixture parameter
$(\,)_{multi}$	Multiple jets
$(\,)_{out}$	Out-going state
$(\,)_{pre}$	Preheating state
$(\,)_{qs}$	Quasi steady
$(\,)_{red}$	Reduced
$(\,)_{ref}$	Reference parameter
$(\,)_{...,RH}$	Rankine Hugoniot FTF
$(\,)_{s}$	Side state
$(\,)_{single}$	Single jet
$(\,)_{sz}$	Secondary zone
$(\,)_{tot}$	Total
$(\,)_{u}$	Upstream
$(\,)_{pr}$	Products from first stage combustion
$(\,)_{pz}$	Primary zone
$(\,)_{...,PMT}$	Photomultiplier FTF
$(\,)_{\infty}$	Crossflow state

Operators

$\langle \cdot \rangle$	Period average
$\langle \cdot, \cdot \rangle$	Inner product
$\mathcal{O}$	Landau operator (order of magnitude)

Abbreviations

BFTM / BFSM	Burner-flame transfer/- scattering matrix
BTM / BSM	Burner transfer/- scattering matrix
CFD	Computational fluid dynamics
CL	Chemiluminescence
CVP	Counter-rotating vortex pair
FTF	Flame transfer function
FTM / FSM	Flame transfer/- scattering matrix
HV	Horse shoe vortex
JIC	Jet in crossflow
LEE	Linearized euler equations
MMM	Multi-microphone method
MISO	Multiple-input-single-output system
OP	Operating point
PIV	Particle image velocimetry
PLIF	Planar laser-induced-fluorescence
PMT	Photomultiplier
POD	Proper orthogonal decomposition
RH	Rankine-Hugoniot
RJIC	Reactive jet-in-crossflow
RQL	Rich-quench-lean
SISO	Single-input-single-output system
SLV	Shear layer vortex
SM	Scattering matrix
TM	Transfer matrix
WV	Wake vortex

1 Introduction and Motivation

The aviation industry has a significant impact on the environment, and reducing its carbon footprint is essential for a sustainable future. In 2001, the Advisory Council for Aviation Research and Innovation in Europe (ACARE) was established to develop a long-term strategic research agenda for aeronautics in Europe [1]. In 2011, ACARE launched Flight Path 2050, a comprehensive plan to reduce aviation emissions and improve technology. Flight Path 2050 sets ambitious targets for the aviation industry to reduce carbon dioxide (CO_2) emissions by 75%, nitrogen oxide (NO_x) emissions by 90%, and noise levels by 65% compared to 2000 levels. One of the key priorities of Flight Path 2050 is the advancement of technologies to reduce emissions from aircraft engines. A crucial technology in this regard is the development of low-emission combustion chambers, which aim to improve the efficiency of fuel combustion, thereby reducing the emissions of harmful gases [2]. One such technology that has gained significant attention in recent years is the rich-quench-lean (RQL) combustion chamber. The RQL combustion chamber is a type of low-emission combustion chamber that has been shown to reduce nitrogen oxide emissions by up to 60% compared to traditional combustors. This is achieved by controlling the fuel-air mixture in three distinct zones: a fuel-rich primary zone, a quenching zone, and a lean-burn secondary zone.

In an RQL combustor, combustion starts in the primary zone, where fuel-rich mixtures with an equivalence ratio typically between $1.2 - 1.8$ are used to initiate combustion. The rich-burn approach offers two main benefits: it enhances combustion stability by generating a high concentration of potent hydrogen and hydrocarbon radical species; and diminishes NO_x production due to the low flame temperatures and

insufficient oxygen-containing intermediate species. The combustion process is completed in an additional burnout section, into which a large part of the dilution air is introduced downstream of the rich zone [3]. In order to limit NO_x levels, the primary zone exhaust must effectively mix with air and transition quickly from a rich to a lean burning mode to minimize thermal NO_x production. The lean-burn section is used to oxidize carbon monoxide (CO), hydrogen, and unburned hydrocarbons exhaustively (UHC) so that the exit of the combustor contains major byproducts of CO_2, N_2, O_2, and H_2O. This process helps to manage an optimal combustor exit temperature distribution and quality. Generally, a global equivalence ratio within the $0.5 - 0.7$ is usually preferred to limit the turbine inlet temperature.

One of the key characteristics of RQL combustor's secondary zone is their ability to rapidly and effectively mix the two gaseous streams. Geometrically simple yet remarkably effective, the jet-in-crossflow (JIC) is a popular flow configuration used in these combustors and in such circumstances. Research on jets in crossflow has been actively pursued for more than half a century due to their impressive mixing performance and the complex physics they are associated with. Their widespread adoption proves this in countless industrial applications. Karagozian [4, 5] and Mahesh [6] recently carried out comprehensive reviews on this topic.

Multiple experimental and numerical studies evaluated the ability of RQL combustors to achieve low emissions and focused on the secondary zone's flow-field and mixing and reaction processes. Holdeman [7] and Rosfjord et al. [8] investigated an RQL combustion chamber with a cylindrical flame tube and various JIC configurations to reduce emissions. The results showed that CO_2 and NO_x emissions were very sensitive to the performance of the JIC mixing zone and less sensitive to the performance of the used injector. Holdeman [7] discovered that the momentum-flux ratio $J = \rho_{\text{jet}} u_{\text{jet}}^2 / \rho_\infty u_\infty^2$, as well as the orifice geometry and spacing are critical parameters influencing mixing, combustion, and

emission processes. Developing staged fuel systems presents unique issues, particularly when anticipating and controlling mixing and flame stabilization in the secondary combustion zone. The local mixture within this region also greatly influences the temperature balance. Thus, it is essential to accurately predict these interactions and combustion dynamics to guarantee optimal engine performance.

Applying these low-emission combustion chamber solutions is restricted by the emergence of thermoacoustic instabilities, adversely affecting operational flexibility. Like all high-power density combustors, RQL combustors are prone to thermoacoustic instabilities resulting from dynamic interactions between acoustic oscillations, flow, and unsteady heat release in the combustion system. Thermoacoustic phenomena have been studied in-depth for decades, but their application to RQL combustion chambers, particularly the secondary JIC mixing zone, is relatively recent. The prediction of the thermoacoustic stability of the engine combustor is important for optimizing its design and performance. Understanding thermoacoustics within RQL combustion chambers can also help improve operation stability and reliability.

Eckstein et al. [9] was one of the first to study the dynamic behavior of RQL combustors. He investigated the excitation mechanisms of low-frequency instabilities in aero-engine combustors called "rumble" or "growl" through experiments and linear stability analysis. The experiments revealed that self-excited combustion instabilities occur when the atomizer is sensitive to changing air mass flows, resulting in oscillations between 80Hz and 135Hz. Observations reveal that entropy waves are convected towards the combustor outlet with bulk velocity, although their strength rapidly diminishes due to dispersion. Nevertheless, the quantitative determination of the systems's thermoacoustic response, e.g., captured as flame-transfer-matrix (FTM) or flame-transfer-function (FTF), was not possible with their setup.

The lean combustion zone's thermoacoustic behavior is believed to im-

pact the overall combustion dynamics of RQL combustors significantly. Recent research by Cai et al. [10] provides supporting evidence for this conjecture. The authors investigated the thermoacoustic characteristics of an RQL combustor operating with natural gas under ambient pressure. They identified various instabilities associated with different operational modes using chemiluminescence heat release images and dynamic pressure measurements within the combustion chamber. Cai et al. [10] showed that acoustic emissions during the RQL operation mode were correlated with the interaction between the fuel-rich mixture and the secondary air jets, thus highlighting the importance of this interaction in the combustion process.

Wilde [11] conducted a comprehensive study investigating the impact of near-field heat release and crossflow acoustics on JIC dynamics. The author employed simultaneous time-resolved Stereo Particle Image Velocimetry (SPIV) measurements, $OH^{\star}$ Planar Laser-Induced Fluorescence (PLIF) reaction zone imaging, and dynamic pressure measurements to analyze the flow structure and flame stabilization for both unforced and forced jets in crossflow under different J and density ratios $S = \rho_{\text{jet}}/\rho_{\infty}$. The study revealed that low-frequency crossflow forcing could significantly affect JIC behavior, even at relatively low amplitudes. The relative importance of asymmetric versus axisymmetric excitation depended on parameters such as J, S, and Mach number. Low J jets (≈ 5) exhibited significant exit velocity fluctuations, resulting in stronger jet flapping and altering both the mean and RMS velocity fields. In contrast, high J jets (≈ 25) experienced lower jet flapping due to increased resistance from jet nozzle impedance, which reduced crossflow-jet-nozzle-coupling effects. The study also highlighted that near-field heat release is crucial in affecting the shear layer stability of reacting jets in crossflow (RJIC), as combustion modifies the shear layer growth rate. For low S cases, the shear layer roll-up was significantly lower for reacting iso-density jets compared to non-reacting ones. When parameterizing density stratification effects on reactant jet in crossflow shear layers, parameters such as flame stabilization location and reaction

zone thickness relative to diameter need to be considered. However, it should be noted that the study only investigated density ratios of $S \leq 1$, whereas density ratios of $S > 1$ are expected in real engine applications.

In the study of Nair et al. [12], the author extended Wilde's research on RJIC. Specifically, Nair et al. investigated the impact of flame position on the shear layer dynamics and the reaction zone structure for reactive jets in crossflow with flames located outside or inside the shear layer. The experiments were conducted using OH^*-PLIF data, and a vortex identification technique was introduced to quantify swirling strength, circulation, and vortex area. The influence of jet parameters such as J and S on the dynamics of the shear layer was also assessed. High repetition rate SPIV measurements were also conducted to classify cases as globally or convectively unstable for different JIC and RJIC conditions based on spectral characteristics. Nair et al. presented Strouhal numbers based on a vorticity thickness and the convective velocity to calculate the dominant jet frequency in the convectively unstable regime. These Strouhal numbers represent the frequency at which the jets will likely "lock in" and alter the dynamic behavior. Despite the comprehensive investigations conducted by Wilde and Nair et al., the global response behavior of reactive jets in crossflow under forcing conditions and the quantification of flame dynamics response in terms of thermoacoustics remained elusive.

1.1 Jet in Crossflow Concept

In order to explain the significance of the research topic in this thesis, it is important first to provide an overview of the JIC and RJIC concepts utilized in RQL combustion chambers. The JIC, a versatile configuration widely used in industrial and commercial combustion systems, enables quick mixing between two streams within a compact space driven by a complex three-dimensional flow field. Its applications span across vari-

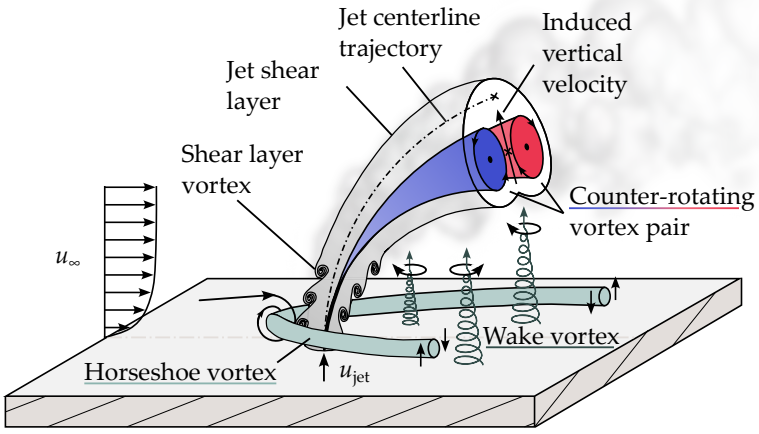

Figure 1.1: Schematic of a transverse jet-in-crossflow, depicting the jet trajectory and the primary swirling vortex patterns.

ous fields, including gas turbine combustors for industrial power plants, jet engine dilution zones to control mixing and reduce NO_x emissions, and to provide film cooling to turbine blades [13, 14]. In order to determine optimal operating conditions and control strategies for JIC, it is crucial to understand their structural, mixing, and, when applicable, reactive characteristics.

1.1.1 Coherent Flow Features of Jets in Crossflow

Typically, the jet emerges perpendicularly from a flush opening embedded in the wall into a crossflow. However, alternative openings, such as elevated ducts or nozzles with different shapes, can also be used. Dimensionless parameters are employed to represent the operating conditions of the JIC. These parameters include the jet-to-crossflow momentum flux ratio J, the velocity ratio R, and the density ratio S. Typically, these parameters scale the characteristic features of the JIC. The jet trajectories, local temperature distributions, local concentration maxima, or the center of mass of characteristic flow structures such as the counter-rotating vortex pair (CVP) have been described using R or J [14–17]. For transverse jets, the dimensionless parameters J and R are determined using

the mean velocities u_{jet} and u_∞, and the densities of the jet (ρ_{jet}) and crossflow (ρ_∞) as follows:

$$J = \frac{\rho_{\text{jet}} u_{\text{jet}}^2}{\rho_\infty u_\infty^2} = \frac{A_\infty \dot{m}_{\text{jet}} u_{\text{jet}}}{A_{\text{jet}} \dot{m}_\infty u_\infty} \tag{1.1}$$

$$R = u_{\text{jet}} / u_\infty \tag{1.2}$$

In RQL combustion chambers, the momentum flux ratio of the transverse jets is usually maintained at approximately $J \approx 20 - 30$ to ensure their adequate penetration into the crossflow [8].

The JIC dynamics are complex and governed by a combination of interdependent vortex systems, some depicted in Fig. 1.1. The counter-rotating vortex pair (CVP) is the most prominent among these. In addition, horseshoe vortices are formed in the upstream region of a jet flush injected from a wall. The upright wake vortices are thought to originate within the wall boundary layer and recur periodically around and beyond the JIC. These vortices entrain fluid from the boundary layer into the jet, with the entrainment being strongest close to $R \approx 4$ [18]. Recent studies on JIC injection from a pipe have suggested that wake vortices dominate the flow dynamics at $R \approx 3.3$, while for lower R values ($R \approx 1.3$), shear-layer vortices (SLV) are the primary dynamical structures within the flow field [19].

In fuel injectors, flow instabilities expedite the transition towards turbulent flow and improve mixing. However, flow instabilities and shear layer dynamics, such as the CVP and the SLV, can trigger combustion instabilities under certain conditions, a phenomenon known as the vorticity-coupled combustion instability mechanism [20]. Despite similarities with the roll-up of axial jets, SLV exhibits distinct characteristics. The asymmetric transport of vortices in the JIC arises from the reverse flow into the jet nozzle due to the strong adverse pressure gradient existing around it [21]. As the SLV convects along its streamwise direction, it gradually grows until vortex pairing and breakdown to turbulence

occur. The Reynolds number of the jet Re_{jet}, J, and the jet exit velocity profile heavily influence the complexity of the SLV's behavior [22]. Such instabilities and disturbances occur in many combustion systems due to shear flows under certain conditions, including swirling jets with high swirl number and axisymmetric jets with low density compared to the surroundings. An initial disturbance is amplified in an unstable flow field, while the same disturbance in a stable flow decays. These disturbances could manifest in many forms, such as turbulent eddies, acoustic waves, or autoignition events. Unstable shear flows are either convectively or globally unstable [23]. Convective instability causes the amplification of any external disturbance inputs and often shows a broadband response, while global instability allows for self-excited oscillations without continuous stimulation resulting in a narrowband response.

Recent studies indicate that the stability of JIC shifts from broadband unstable to narrowband unstable when R is sufficiently low, approximately at 3.2. Hot-wire measurements in the windward shear layer showed a drastic change in flow spectral characteristics for $S \approx 1$ conditions and $J \approx 10.2$ [24]. Davitian et al. [25] found that low J jets resist low-level acoustic forcing, a characteristic of many narrowband unstable flows.

Bagheri et al. [26] conducted a linear stability analysis on JIC with $R = 3$ and identified two linearly unstable narrowband modes in the flow: one high frequency mode associated with SLV and another lower frequency mode in the wake of the jet, which can cause oscillation for mixing enhancement purposes. Getsinger et al. [27] extended experimental work from unity S to variable density ratio jets in crossflow. The single-component hot-wire measurements indicated that broadband instability transitions into narrowband instability when $S \leq 0.45$, but regardless of the magnitude of S, it always becomes narrowband unstable at sufficiently low J levels.

However, the stability of a reacting JIC has not yet been fully examined. Therefore, it is essential to be careful when generalizing non-reacting results due to evidence that chemical heat release can change the stability limits in shear flows [28]. Juniper et al. [29] studied an axial jet with narrowband instability under reactive and non-reactive conditions. Consequently, they concluded that narrowband instability significantly increases when reactions are involved. The combustion process can affect the stability of a system in two ways: actively participating in an instability mechanism or changing the base flow. Mahalingam et al.'s [30] analysis revealed that changes to the base flow had a much more significant impact on stability than active participation, which is not unexpected due to significant modifications caused by heat release during combustion.

1.1.2 Entrainment, Mixing and Flame Stabilization of Jets in Crossflow

Recent findings identified coherent vortical structures as the driving force behind the improved mixing performance of JIC compared to axial jets [15]. These structures alter the jet to crossflow interface, allowing crossflow fluid to enter into the jet at a faster rate. Subsequently, this increases surface area and strong gradients in mixture fraction fields, promoting molecular diffusion for enhanced results. Non-premixed reacting jets in crossflow rely heavily on the fuel/air mixing dynamics to ensure flame stabilization, heat release distribution, and minimal pollutant formation. A high difference is noticed between those jets stabilized in cold air crossflows and those established in hot vitiated crossflows. Alternative flame stabilization mechanisms, including autoignition, are possible in vitiated flows. Reaction zones are sustained in locations with flow velocities that are not achievable when a jet is injected into an air crossflow of low temperature. Schmitt et al. [31] investigated flame stabilization in premixed jets injected into a vitiated crossflow with a temperature of $T_\infty = 1776\,\mathrm{K}$ and equivalence ratios,

ϕ, between $0.05 \leq \phi \leq 0.77$ and J ranging from $4 \leq J \leq 10$. The flames were all attached along the entire circumference of the nozzle at every condition tested, while penetration significantly increased when compared against non-reactive jets. Jets with higher ϕ showed substantially shorter flame lengths compared to those of lower ϕ. The $OH^{\star}$ chemiluminescence imaging revealed that turbulence had a more profound effect on the structure in low ϕ jets. Moreover, flow-flame interaction at elevated T_{∞} and premixed flames verify the turbulent conditions within jet in crossflow near-field region.

Furthermore, researchers have studied the response of jets in vitiated crossflows in RQL literature. These combustors involve "inverse flames" where the jet contains the oxidizer while the crossflow carries fuel. The investigations mainly focus on interactions between multiple JIC, typically under high J conditions with significant confinement. Despite this structural variation between inverse flames and traditional fuel jets, only a few studies have examined what sets them apart; thus, a deeper understanding of their behavior remains largely unknown.

1.1.3 Forced Response of Jets in Crossflow

Several studies have examined forcing the JIC to maximize jet penetration and enhance mixing [32–35]. These investigations have focused exclusively on jet forcing and have not considered crossflow forcing. Notably, a single optimal forcing condition for maximum penetration has not been identified, as various studies have reported significant differences in the conditions required for optimal performance [35]. In forced response studies, a wide range of parameters need to be considered, including the forcing frequency (f_F), amplitude (u'_{jet}), duty cycle (α_F), and pulse shape. Investigations have further shown that jet penetration is substantially enhanced when the forcing frequency f_F is lower than the fundamental mode of shear-layer vortices (SLV) [33,34].

Jets operating in the narrowband unstable regime with low values of J

and S exhibit resistance to low amplitude sinusoidal forcing [24, 25, 27]. On the other hand, broadband unstable jets with their shear layer structures heavily respond to this same kind of perturbation. While it is challenging to excite a narrowband instability with small amplitude forcing, it has been noted that high-amplitude forcing near the fundamental mode can induce lock-in to the forcing frequency.

Recently, Marr et al. [36] conducted a study to investigate the effects of acoustic forcing on jet flames stabilized in crossflow with low temperatures and discovered that it significantly shortened non-premixed flame lengths. Eroglu and Breidenthal [33] observed similar behavior. Their reactive LIF measurements of a forced JIC revealed that flame length decreased by 50% at optimal pulsing conditions. The findings demonstrate that the near-field mixing due to forcing creates remarkably similar emission profiles comparable with those from partially premixed unforced jets.

In neither of the studies significant impacts of jet forcing altering the crossflow has been found or described.

Vice versa, crossflow forcing on jets in crossflow has only been studied a few times in the literature, and even less for reactive jets in crossflow [11, 12, 37–39]. Acoustic driving the jets from jet-flow direction will likely result in axisymmetric excitation and consequential production of ring vortices at the jet nozzle exit plane. In contrast, crossflow forcing exhibits an inherent asymmetry, similar to forcing conditions used to study transverse excitation in swirl flames [40]. Crossflow forcing in the JIC system suppresses the dominant spectral features observed in the unforced JIC. However, applying crossflow forcing at a certain frequency can lead to the initiation of flapping and detaching motions, which increase in dominance as the forcing amplitude increases. POD analysis of the velocity and scalar fields taken from forced LES results shows a longer, thinner jet plume with a lower flame center of gravity for its scalar values. The flapping of the jet helps spread out the fluid

over time but also leads to more noticeable fluctuations within its mixing processes [38].

The studies of Wilde [11] indicated that low-frequency crossflow acoustics provide both asymmetric and axisymmetric excitation of the jets. The fluctuating crossflow velocity, u'_∞, induces a bulk, asymmetric velocity response. On the other hand, the fluctuating crossflow pressure, p'_∞, induces a time-varying pressure drop across the jet nozzle, which leads to a fluctuating jet exit velocity, u'_{jet}, that axisymmetrically excites the jet. This axisymmetric excitation of the jet is called jet-nozzle-coupling to emphasize the similarity with behavior observed in liquid rocket instability research and causes periodic jet flapping, whose magnitude depends heavily on the JIC parameters, such as J, R, and S.

Following the earlier discussion of acoustics and combustion instability in jet engine combustors, e.g., RQL combustors, this section pivots slightly to emphasize the connection to the forced response of JIC. The acoustic environment within gas turbines and jet engines can be thought of as a built-in forcing mechanism. The JIC is considered acoustically compact since its natural frequencies generally lie around several hundreds of Hertz, the preheated speed of sound is high, and jet diameters are typically quite small.

An oscillating acoustic field will induce a varying mass flow rate through the jet nozzle, fluctuating in intensity and phase as determined by the local sound pressure level and nozzle impedance Z_{jet}. This impedance is further reliant on several factors, including the average mass flow rate, the velocity within the jet nozzle, fluid properties at that location, and its overall geometric configuration. The intensity of acoustic waves inside a combustor is strongly determined by its geometry and boundary conditions. Even small oscillations in combustion chamber pressure p' can cause massive time-varying mass flux, because of the low pressure drop of JIC nozzles. The unsteady mass flow rate generated by the JIC nozzle can enhance combustion instability due to

the additional unsteady heat release. In any stability analysis of gas turbine or jet engine combustors using jets in crossflow, it is essential to take into account crossflow oscillations, the resulting jet-nozzle-coupling, and jet oscillations. The coupling between the jet nozzles and acoustically unsteady crossflow can affect JIC performance by altering penetration depth and mixing even if the unsteady mass flow does not amplify thermoacoustic instabilities.

1.2 Research Questions and Thesis Outline

This thesis focuses on elucidating the flame dynamics of the lean burnout zone of a Rich-Quench-Lean (RQL) combustion chamber. With the new experimental approach of spatially separating the rich primary zone from the lean burnout zone, both can be independently investigated to determine the respective contribution to the total system dynamics. The experimental setup offers the possibility to acoustically force the RJIC configuration in the secondary zone from crossflow and jet direction and perform thermoacoustic investigations. The dynamic flame behavior is measured in terms of two individual flame transfer functions representing the response to velocity fluctuations from both directions.

Chapter 2 provides a comprehensive overview of the fundamental concepts of thermoacoustics and presents the equations and assumptions utilized in this investigation. The application of conservation equations to elucidate plain wave propagation and necessary boundary conditions forms the foundation for describing thermoacoustic systems. Fluctuating pressure p' and velocity u' are interdependent to define thermoacoustic systems using basic network components. The chapter concludes by examining the flame dynamics within the framework of thermoacoustic network modeling. Previous studies have emphasized the necessity to consider two excitation positions, namely, forcing the jets themselves and the crossflow, as both significantly impact the dynamic behavior of

reactive jets in crossflow. The first question tackled by this thesis is as follows:

- *How to describe the dynamic response of the lean secondary zone while differentiating between the velocity fluctuations from the crossflow and the jet?*

In Chapter 3, a modeling approach is presented to characterize the dynamic flame response of the lean secondary zone based on the resulting complex acoustic velocity fluctuations produced by forcing the jets or the crossflow. The objective is to develop a network system-based formulation that allows the individual description of the dynamic behavior using FTFs.

Given that the RJIC setup under investigation is categorized as a convectively and broadband unstable jet, it is postulated that induced disturbances propagate within the shear layer of the inverse diffusion flame. In this context, inverse diffusion implies that fuel mass flow is entrained while air constitutes the jet. A first-order physical model describing the convective time delay experienced by a perturbation traveling within the reactive shear layer of the secondary air jets is formulated in Chapter 4. This model is utilized to validate the phase response of the presented FTFs and offers insight into the governing physical mechanisms. Chapters 5 and 6 provide a detailed overview of the experimental facility used in this study, including a thorough description of the test matrix employed. The chapters also include a discussion of the reasoning behind the selection of the specific conditions tested, providing a comprehensive summary of the experimental methodology employed in the study.

The modeling approach is validated by identifying asymptotic cases where the RJIC system responds solely to crossflow or jet velocity fluctuations. These results are presented in Chapter 7 and at the beginning of Chapter 8, thus leading to the second and third research questions discussed in the remaining sections of Chapter 8:

- *How does the inverse diffusion flame in the lean secondary zone react to velocity fluctuations in the crossflow and the jets depending on various operating conditions?*
- *How does the dynamic flame response differ with changing geometrical jet parameters and configurations?*

In Chapter 9, the findings are summarized and highlighted. The chapter provides an overview of the major contributions of this work and outlines the potential routes for future research in this area.

2 Basic Concepts of Thermoacoustics

The following chapter provides the basic equations and assumptions for thermoacoustic investigations. Using conservation equations to explain the plain wave propagation and essential boundary conditions serves as a foundation for describing thermoacoustic systems. The relationship between dynamic pressure and velocity is used to characterize thermoacoustic systems using simple network elements. The chapter closes with the characterization of the flame dynamics in the context of thermoacoustic network modeling.

2.1 Linearized Acoustic Equations

In the realm of jet engines and gas turbine combustors, the flow can often be characterized by examining compressible flow transport properties in both temporal and spatial domains. Such flow phenomena can be generally represented by the conservation equations of mass, momentum, and energy, which are accompanied by the ideal gas law, $p = \rho \mathbb{R} T$:

$$\frac{\partial \rho}{\partial t} + \frac{\partial \rho u_\mathrm{i}}{\partial x_\mathrm{i}} = 0 \tag{2.1}$$

$$\frac{\partial u_\mathrm{i}}{\partial t} + u_\mathrm{j}\frac{\partial u_\mathrm{i}}{\partial x_\mathrm{j}} + \frac{1}{\rho}\frac{\partial p}{\partial x_\mathrm{i}} = \frac{\partial \tau_\mathrm{ij}}{\partial x_\mathrm{j}} \tag{2.2}$$

$$\frac{\partial p}{\partial t} + u_\mathrm{i}\frac{\partial p}{\partial x_\mathrm{i}} + p\gamma\frac{\partial u_\mathrm{i}}{\partial x_\mathrm{i}} = (\gamma - 1)\dot{q}_\mathrm{V} + (\gamma - 1)\tau_\mathrm{ij}\frac{\partial u_\mathrm{i}}{\partial x_\mathrm{j}} \tag{2.3}$$

Density ρ, velocity field u_i with the coordinates x_i, and pressure p represent the spatio-temporal solution variables. The ratio of specific heats is referred to as γ, and $\dot{q}_\mathrm{V}$ captures the volumetric heat source from the combustion process. The stress tensor is denoted by τ. Numerous sim-

plified sets of equations can be derived utilizing the fundamental system of non-linear, coupled partial differential equations [41]. To calculate the spatio-temporal propagation of coherent disturbances, they are separated into a varying mean quantity $\bar{(\,)}$ and a superimposed perturbation part $(\,)'$ [42]. The amplitudes of the flow perturbations observed in jet engines are assumed to be small compared to their corresponding mean flow quantities. In the case of the velocity fluctuations u' this refers to the speed of sound c:

$$\rho' \ll \bar{\rho} \quad p' \ll \bar{p} \quad u' \ll c \tag{2.4}$$

With this assumption, the products of the second and higher order disturbance components are neglected; thus, nonlinear effects can be ignored. The instantaneous values of the flow variables can be expressed as follows:

$$\rho = \bar{\rho} + \rho' \tag{2.5}$$
$$p = \bar{p} + p' \tag{2.6}$$
$$u = \bar{u} + u' \tag{2.7}$$
$$\dot{q}_\mathrm{V} = \bar{\dot{q}}_\mathrm{V} + \dot{q}'_\mathrm{V} \tag{2.8}$$

Inserting Eqs. 2.5-2.8 into Eqs. 2.1-2.3, using the linearity assumptions and neglecting any viscous stresses (thus $\tau = 0$), which is common in thermoacoustics [43], leads to the Linearized-Euler Equations (LEE):

$$\frac{\partial \rho'}{\partial t} + \bar{u}_\mathrm{i}\frac{\partial \rho'}{\partial x_\mathrm{i}} + u'_\mathrm{i}\frac{\partial \bar{\rho}}{\partial x_\mathrm{i}} + \bar{\rho}\frac{\partial u'_\mathrm{i}}{\partial x_\mathrm{i}} + \rho'\frac{\partial \bar{u}_\mathrm{i}}{\partial x_\mathrm{i}} = 0 \tag{2.9}$$

$$\frac{\partial u'_\mathrm{i}}{\partial t} + \bar{u}_\mathrm{j}\frac{\partial u'_\mathrm{i}}{\partial x_\mathrm{i}} + u'_\mathrm{j}\frac{\partial \bar{u}_\mathrm{i}}{\partial x_\mathrm{j}} + \frac{1}{\bar{\rho}}\frac{\partial p'}{\partial x_\mathrm{i}} + \frac{\rho'}{\bar{\rho}}\bar{u}_\mathrm{j}\frac{\partial \bar{u}_\mathrm{i}}{\partial x_\mathrm{i}} = 0 \tag{2.10}$$

$$\frac{\partial p'}{\partial t} + u'_\mathrm{i}\frac{\partial \bar{p}}{\partial x_\mathrm{i}} + \bar{u}_\mathrm{i}\frac{\partial p'}{\partial x_\mathrm{i}} + \gamma\left(\bar{p}\frac{\partial u'_\mathrm{i}}{\partial x_\mathrm{i}} + p'\frac{\partial \bar{u}_\mathrm{i}}{\partial x_\mathrm{i}}\right) = (\gamma - 1)\dot{q}'_\mathrm{V} \tag{2.11}$$

2.2 The Wave Equation

With the application to thermoacoustics and acoustic wave propagation, the velocity gradients ($\partial \bar{u}_i / \partial x_i = 0$) in the LEE are neglected to derive a simplified form. Additionally, isentropicity is assumed, which defines the linear dependency between acoustic pressure and the density by $\rho' = {}^{p'}/_{c^2}$ [44]. The LEE Eqs. 2.9-2.11 are then simplified to:

$$\frac{\partial p'}{\partial t} + \bar{u}_i \frac{\partial p'}{\partial x_i} + \bar{\rho} c^2 \frac{\partial u_i'}{\partial x_i} = (\gamma - 1)\dot{q}_V' \tag{2.12}$$

$$\frac{\partial u_i'}{\partial t} + \bar{u}_i \frac{\partial u_i'}{\partial x_i} + \frac{1}{\bar{\rho}} \frac{\partial p'}{\partial x_i} = 0 \tag{2.13}$$

Subtracting the spatial derivative of Eq. 2.13 from the temporal derivative of Eq. 2.12 leads to the common expression for the convective wave equation in the time domain:

$$\frac{1}{c^2} \left(\frac{\partial}{\partial t} + \bar{u}_i \frac{\partial}{\partial x_i} \right)^2 p' - \frac{\partial^2 p'}{\partial x_i^2} = \frac{\gamma - 1}{c^2} \frac{\partial \dot{q}_V'}{\partial t} \tag{2.14}$$

Similarly, it is possible to derive a convective momentum equation relating the acoustic velocity to the acoustic pressure:

$$\bar{\rho} \left(\frac{\partial}{\partial t} + \bar{u}_i \frac{\partial}{\partial x_i} \right) u' + \frac{\partial p'}{\partial x_i} = 0 \tag{2.15}$$

This equation is based on the proposal that in the linear, first-order theory, the flow field can be decoupled into acoustics, vorticity, and entropy parts [45].

2.3 Propagation of One-Dimensional Plane Waves

The acoustic wave propagation in ducts can be considered approximately one-dimensional if the wavelength $\lambda = c/f$ is significantly larger than the duct diameter d_{duct}. A more precise criterion is defined by the cut-off frequency [46]. Below this cut-off frequency, the wavenumber of

multidimensional acoustic modes has a negative imaginary part, e.g., the modes do not spatially propagate in the considered duct. The convective wave equation Eq. 2.14 can be solved analytically assuming a uniform temperature distribution and ignoring the heat release source term on the right-hand side of the equation ($\dot{q}'_{\mathrm{V}} = 0$). In a moving medium, the transport equation can be obtained by considering wave propagation along the x direction as follows:

$$\left(\frac{1}{c^2}\left(\frac{\partial}{\partial t} + \bar{u}\frac{\partial}{\partial x}\right)^2 - \frac{\partial^2}{\partial x^2}\right) p' = 0 \tag{2.16}$$

In the context of linear-acoustic systems, assuming a harmonic wave character is common. This assumption allows the representation of time-dependent fluctuating quantities as harmonic functions in the frequency domain:

$$\rho'\left(x_{\mathrm{i}}, t\right) = \widehat{\rho}_{\mathrm{i}}\left(x_{\mathrm{i}}\right) e^{(i\omega t)} \tag{2.17}$$

$$p'\left(x_{\mathrm{i}}, t\right) = \widehat{p}_{\mathrm{i}}\left(x_{\mathrm{i}}\right) e^{(i\omega t)} \tag{2.18}$$

$$u'_{\mathrm{i}}\left(x_{\mathrm{i}}, t\right) = \widehat{u}_{\mathrm{i}}\left(x_{\mathrm{i}}\right) e^{(i\omega t)} \tag{2.19}$$

$$\dot{q}'_{\mathrm{V}}\left(x_{\mathrm{i}}, t\right) = \widehat{\dot{q}}_{\mathrm{V}}\left(x_{\mathrm{i}}\right) e^{(i\omega t)} \tag{2.20}$$

The $\widehat{(\,)}$ denotes the complex Fourier transformed of the harmonically oscillating quantities with the angular frequency $\omega = 2\pi f$. The harmonic ansatz for the pressure p' is now used to solve the partial differential Eq. 2.16. Therefore, the convective wave number $k = \omega/c$ is introduced, and the fluctuating pressure is written as:

$$p' = \widehat{p} e^{\left(i\omega\left(t - \frac{x}{c}\right)\right)} \tag{2.21}$$

Inserting Eq. 2.21 into Eq. 2.16 leads to the following equation:

$$((i\omega + \bar{u}k)^2 - c^2k^2)p' = 0 \tag{2.22}$$

The two solutions are found with:

$$k^{\pm} = \frac{\omega}{c \pm \bar{u}} \tag{2.23}$$

The wavenumber Eq. 2.23 is inserted into Eq. 2.22, and a linear combination of both gives the solution of the quadratic equation:

$$p'(x,t) = C_1^+ \, e^{(-i\omega t + k^+ x)} + C_2^- \, e^{(i\omega t + k^- x)} \tag{2.24}$$

The acoustic velocity u' is calculated assuming a similar form as for the acoustic pressure p':

$$u'(x,t) = C_1^+ \frac{1}{\bar{\rho}c} \, e^{(-i\omega t + k^+ x)} - C_2^- \frac{1}{\bar{\rho}c} \, e^{(i\omega t + k^- x)} \tag{2.25}$$

The product $\bar{\rho}c$ of the mean density and the speed of sound is called the characteristic field impedance. It can be interpreted as fluid element's resistance (inertia) to a deflection due to a pressure fluctuation. The integration constants C_1^+ and C_2^- are determined by the boundary conditions to close the differential equation and represent the complex amplitudes traveling in co-flow, and counter-flow direction [47]. These traveling waves are often referred to as the Riemann invariants and are denoted by the variables $\widehat{f}$ for co-flow and $\widehat{g}$ for counter-flow direction. The acoustic pressure and velocity can be expressed as follows:

$$p'(x,t) = \bar{\rho}c \left(f e^{(i\omega t + k^+ x)} + g e^{(i\omega t + k^- x)} \right) \tag{2.26}$$

$$u'(x,t) = \left(\underbrace{f e^{(i\omega t + k^+ x)}}_{\widehat{f}} - \underbrace{g e^{(i\omega t + k^- x)}}_{\widehat{g}} \right) \tag{2.27}$$

Starting from Eq. 2.26 and 2.27, it can be shown that $\widehat{f}$ and $\widehat{g}$ are related to the acoustic variables p' and u' as follows:

$$\widehat{f} = \frac{1}{2}\left(\frac{p'}{\bar{\rho}c} + u'\right) \tag{2.28}$$

$$\widehat{g} = \frac{1}{2}\left(\frac{p'}{\bar{\rho}c} - u'\right) \tag{2.29}$$

2.4 Boundary Conditions

Acoustic boundary conditions are often described by a reflection coefficient R or an acoustic impedance Z. The reflection coefficient is determined for one-dimensional wave propagation downstream from the ratio of the complex amplitudes of the reflected wave with respect to the incoming wave propagating. A distinction is made whether the boundary condition is a flow inlet or an outlet:

$$R_{\text{in}} = \frac{\widehat{f}_{\text{in}}}{\widehat{g}_{\text{in}}}, \qquad R_{\text{out}} = \frac{\widehat{g}_{\text{out}}}{\widehat{f}_{\text{out}}} \tag{2.30}$$

As an alternative to the reflection coefficient, the impedance Z can be used to describe acoustic boundary conditions:

$$Z = \frac{\widehat{p}}{\bar{\rho}c\widehat{u}} \tag{2.31}$$

Impedance and reflection coefficient are linked as follows:

$$Z = \frac{1+R}{1-R} \tag{2.32}$$

Three idealized acoustic boundary conditions are common. First, the acoustic soft end where the fluctuating pressure p' reaches values close to zero at the boundary, thus $R = -1$, $Z = 0$. For example, this results in an opening of a duct to an infinite volume. An incident wave is completely reflected with a phase shift of π. Second, the acoustic stiff

end where velocity fluctuations u' become zero e.g., for rigid walls. Here $R = 1$ and the impedance becomes $Z = \infty$. Third, the ideally absorbing end is determined by $R = 0$ and $Z = \bar{\rho}c$ becoming the characteristic impedance. An incident wave is completely absorbed or transmitted.

2.5 Linear Acoustic Network Modeling

The network modeling method used in acoustics originates from electrical network analysis. In this method, a port connects the poles of a black box and describes the relationship between in-going and out-going waves represented by the state variables. The most commonly chosen state variables are the electric current and voltage in electrical multi-ports and the acoustic pressure p' and velocity u' or the Riemann invariants $\widehat{f}$ and $\widehat{g}$ in acoustic applications. In the analysis of electrical circuits, the number of poles corresponds to the number of degrees generated by flowing electric currents. Each requires a separate wire, considered a port in the topological representation. Similar to the number of ports that occur in an acoustic system, assuming that only plane wave propagation is considered. In analyzing the acoustic field, the number of ports is essential, as it represents the geometry and topology of the system under consideration. For this reason, the concept of an acoustic N-port defined by the N-number of ducts coupled to the element under investigation has been introduced. As a result, a selected acoustic subsystem connected to some others by N-ducts is referred to as an acoustic N-port.

Linear thermoacoustic systems can be described by a superposition or network of subsystems (N-ports) according to systems theory [48–50]. Each element of the modular network thus characterizes a component of the overall system, e.g., the burners or dampers and even flames of a combustion chamber. More complex subsystems can be replaced by a network of simple acoustic N-port elements. Frequently used representatives for simple N-port elements are ducts (2-ports), area

jumps (2-ports), or junctions (mostly 3-ports). The transfer behavior of these elements characterizes the linear relationship between the acoustic variables at their inputs and outputs. A low-order model can represent the system's acoustic properties by connecting multiple elements or subsystems. This modularity allows the inclusion of an experimentally determined flame transfer function in such models.

Based on the most common and documented applications of an element with one in- and output ($N = 2$), the linear acoustic network modeling approach is explained next, and a general representation of N-port elements is derived. These elements are described via a linear time-invariant transfer or scattering matrix. Detailed expressions for ducts and area jumps are provided. Afterward, the representation of a 3-port junction is presented.

2.5.1 General Representation of N-port Elements

The transfer matrices **TM** describe the linear relationship between the acoustic state upstream (subscript $(\,)_\mathrm{u}$) and downstream (subscript $(\,)_\mathrm{d}$) of acoustic elements which is given as follows [50]:

$$\begin{bmatrix} \widehat{f} \\ \widehat{g} \end{bmatrix}_\mathrm{d} = \underbrace{\begin{bmatrix} \mathrm{TM}_{11} & \mathrm{TM}_{12} \\ \mathrm{TM}_{21} & \mathrm{TM}_{22} \end{bmatrix}}_{\mathbf{TM}^{\mathrm{fg}}} \begin{bmatrix} \widehat{f} \\ \widehat{g} \end{bmatrix}_\mathrm{u} \tag{2.33}$$

In order to couple acoustic pressure and velocity between two reference planes, the transfer matrix can be rearranged rather than linking the Riemann variants:

$$\begin{bmatrix} \frac{p'}{\bar{\rho}c} \\ u' \end{bmatrix}_\mathrm{d} = \underbrace{\begin{bmatrix} \mathrm{TM}_{11} & \mathrm{TM}_{12} \\ \mathrm{TM}_{21} & \mathrm{TM}_{22} \end{bmatrix}}_{\mathbf{TM}^{\mathrm{pu}}} \begin{bmatrix} \frac{p'}{\bar{\rho}c} \\ u' \end{bmatrix}_\mathrm{u} \tag{2.34}$$

The transformation between both representations can be performed utilizing the transformation matrix Ω [51,52]:

$$\Omega = \begin{bmatrix} 1 & 1 \\ 1 & -1 \end{bmatrix} \tag{2.35}$$

$$\Omega^{-1} = \frac{1}{2} \begin{bmatrix} 1 & 1 \\ 1 & -1 \end{bmatrix} \tag{2.36}$$

$$\mathbf{TM}^{\mathrm{pu}} = \Omega \cdot \mathbf{TM}^{\mathrm{fg}} \cdot \Omega^{-1} \tag{2.37}$$

$$\mathbf{TM}^{\mathrm{fg}} = \Omega^{-1} \cdot \mathbf{TM}^{\mathrm{pu}} \cdot \Omega \tag{2.38}$$

Multiplication of the transfer matrices of all subsystems yields the transfer behavior of the overall system of i network elements such as $\mathbf{TM}_{\mathrm{sys}} = \mathbf{TM}_{\mathrm{i}} \cdot \mathbf{TM}_{\mathrm{i}-1} \cdot \mathbf{TM}_{\mathrm{i}-2} \cdot ... \cdot \mathbf{TM}_{1}$.

Besides the transfer matrix, the network element can also be characterized by a scattering matrix **SM**. Therein, the individual matrix elements referred to as complex reflection (R^+, R^-) and transmission coefficients (T^+, T^-) couple the Riemann invariants to the wave propagation through the element. As waves leave and enter the acoustic element separately, scattering matrices maintain causality over transfer matrices:

$$\begin{bmatrix} \widehat{g}_{\mathrm{u}} \\ \widehat{f}_{\mathrm{d}} \end{bmatrix} = \underbrace{\begin{bmatrix} R^+ & T^- \\ T^+ & R^- \end{bmatrix}}_{\mathbf{SM}^{\mathrm{fg}}_{2\times2}} \begin{bmatrix} \widehat{f}_{\mathrm{u}} \\ \widehat{g}_{\mathrm{d}} \end{bmatrix} \tag{2.39}$$

Similar to the transformation between transfer matrices, the scattering matrix can be transformed into a transfer matrix representation:

$$\mathbf{SM}_{\mathrm{fg}} = \frac{1}{\mathrm{TM}^{\mathrm{fg}}_{22}} \begin{bmatrix} \mathrm{TM}^{\mathrm{fg}}_{11}\mathrm{TM}^{\mathrm{fg}}_{22} - \mathrm{TM}^{\mathrm{fg}}_{12}\mathrm{TM}^{\mathrm{fg}}_{21} & \mathrm{TM}^{\mathrm{fg}}_{12} \\ -\mathrm{TM}^{\mathrm{fg}}_{21} & 1 \end{bmatrix} \tag{2.40}$$

In the following, the transfer and scattering matrices of different com-

ponents are presented, which are used in Chapter 3 to describe the secondary zone in terms of a network system.

2.5.2 Ducts with Constant Cross-Section (2-port)

Considering a duct without losses of length l at a constant cross-section, with flow at the mean velocity $\bar{u}$, then the acoustic waves $\widehat{f}$ and $\widehat{g}$ traveling at the speed of sound undergo a phase change between the two nodes upstream $(\,)_\mathrm{u}$ and downstream $(\,)_\mathrm{d}$ according to:

$$\widehat{f}_\mathrm{d}(x=l) = \widehat{f}_\mathrm{u} e^{(-ik^+l)} \tag{2.41}$$

$$\widehat{g}_\mathrm{d}(x=l) = \widehat{g}_\mathrm{u} e^{(ik^-l)} \tag{2.42}$$

The transfer matrix now connects the two states upstream and downstream over the length of the duct:

$$\begin{bmatrix} \widehat{f} \\ \widehat{g} \end{bmatrix}_\mathrm{d} = \begin{bmatrix} e^{(-ik^+l)} & 0 \\ 0 & e^{(ik^-l)} \end{bmatrix} \begin{bmatrix} \widehat{f} \\ \widehat{g} \end{bmatrix}_\mathrm{u} \tag{2.43}$$

Transformed with Eq. 2.35 and 2.36, using the normalized acoustic pressure and the velocity at the specific states, it follows:

$$\begin{bmatrix} \frac{p'}{\bar{\rho}c} \\ u' \end{bmatrix}_\mathrm{d} = \begin{bmatrix} e^{(-ik^+l)} + e^{(ik^-l)} & e^{(-ik^+l)} - e^{(ik^-l)} \\ e^{(-ik^+l)} - e^{(ik^-l)} & e^{(-ik^+l)} + e^{(ik^-l)} \end{bmatrix} \begin{bmatrix} \frac{p'}{\bar{\rho}c} \\ u' \end{bmatrix}_\mathrm{u} \tag{2.44}$$

2.5.3 Area Jumps (2-port)

Area jumps in a duct are usually modeled as acoustically compact. The axial extent l of the change in cross-section is much smaller than the wavelengths considered. This assumptions hold if $He = {}^{\omega l}/_{c} = kl \ll 1$. The transfer matrix can be determined based on the conservation equations for mass and momentum. After linearization, neglecting terms of higher order and any losses, for an iso-thermal area jump, the transfer

matrix for low Mach numbers is given as follows:

$$\begin{bmatrix} \frac{p'}{\bar{\rho}c} \\ u' \end{bmatrix}_{\mathrm{d}} = \begin{bmatrix} 1 & 0 \\ 0 & \frac{A_{\mathrm{u}}}{A_{\mathrm{d}}} \end{bmatrix} \begin{bmatrix} \frac{p'}{\bar{\rho}c} \\ u' \end{bmatrix}_{\mathrm{u}} \tag{2.45}$$

If losses and length correction (reduced l_{red}, and effective l_{eff}) are considered, then the resulting transfer matrix can be found in the literature [52–55].

2.5.4 Junctions (3-port)

A 3-port junction describes an element in which, e.g., two incoming flows are combined to one outgoing flow. Based on the conservation of mass and momentum, the following equations can be formulated for an isothermal flow through the junction [53]. For a basic simplified application, an ideal case without losses is considered:

$$\left[\left(\frac{p'}{\bar{\rho}c}M + u'\right)A\right]_{\mathrm{u},1} + \left[\left(\frac{p'}{\bar{\rho}c}M + u'\right)A\right]_{\mathrm{u},2} = \left[\left(\frac{p'}{\bar{\rho}c}M + u'\right)A\right]_{\mathrm{d}} \tag{2.46}$$

$$\left[\left(\frac{p'}{\bar{\rho}c} + u'M\right)\right]_{\mathrm{u},1} = \left[\left(\frac{p'}{\bar{\rho}c} + u'M\right)\right]_{\mathrm{d}} \tag{2.47}$$

$$\left[\left(\frac{p'}{\bar{\rho}c} + u'M\right)\right]_{\mathrm{u},2} = \left[\left(\frac{p'}{\bar{\rho}c} + u'M\right)\right]_{\mathrm{d}} \tag{2.48}$$

The subscripts $(\,)_{\mathrm{u},1,2}$ represent the two incoming ducts. Combining the Eqs. 2.46, 2.47 and 2.48, assuming low Mach-numbers ($M \approx 0$) leads to the following equation system:

$$\begin{bmatrix} 0 & A_{\mathrm{u},1} \\ 1 & 0 \\ 0 & 0 \end{bmatrix} \begin{bmatrix} \frac{p'}{\bar{\rho}c} \\ u' \end{bmatrix}_{\mathrm{u},1} + \begin{bmatrix} 0 & A_{\mathrm{u},2} \\ 0 & 0 \\ 1 & 0 \end{bmatrix} \begin{bmatrix} \frac{p'}{\bar{\rho}c} \\ u' \end{bmatrix}_{\mathrm{u},2} = \begin{bmatrix} 0 & A_{\mathrm{d}} \\ 1 & 0 \\ 1 & 0 \end{bmatrix} \begin{bmatrix} \frac{p'}{\bar{\rho}c} \\ u' \end{bmatrix}_{\mathrm{d}} \tag{2.49}$$

Conversion to the Riemann invariants leads to:

$$\begin{bmatrix} A_{\mathrm{u},1} & -A_{\mathrm{u},1} \\ 1 & 1 \\ 0 & 0 \end{bmatrix} \begin{bmatrix} \widehat{f} \\ \widehat{g} \end{bmatrix}_{\mathrm{u},1} + \begin{bmatrix} A_{\mathrm{u},2} & -A_{\mathrm{u},2} \\ 0 & 0 \\ 1 & 1 \end{bmatrix} \begin{bmatrix} \widehat{f} \\ \widehat{g} \end{bmatrix}_{\mathrm{u},2} = \begin{bmatrix} -A_{\mathrm{d}} & A_{\mathrm{d}} \\ -1 & -1 \\ -1 & -1 \end{bmatrix} \begin{bmatrix} \widehat{f} \\ \widehat{g} \end{bmatrix}_{\mathrm{d}} \tag{2.50}$$

Rearranged in the scattering matrix sense preserving flow directions, leads to:

$$\begin{bmatrix} \widehat{g}_{\mathrm{u},1} \\ \widehat{g}_{\mathrm{u},2} \\ \widehat{f}_{\mathrm{d}} \end{bmatrix} = \underbrace{\begin{bmatrix} \frac{-A_{\mathrm{u},2}+A_{\mathrm{u},1}-A_{\mathrm{d}}}{A_{\mathrm{u},1}+A_{\mathrm{u},2}+A_{\mathrm{d}}} & \frac{2A_{\mathrm{u},2}}{A_{\mathrm{u},1}+A_{\mathrm{u},2}+A_{\mathrm{d}}} & \frac{2A_{\mathrm{d}}}{A_{\mathrm{u},1}+A_{\mathrm{u},2}+A_{\mathrm{d}}} \\ \frac{2A_{\mathrm{u},1}}{A_{\mathrm{u},1}+A_{\mathrm{u},2}+A_{\mathrm{d}}} & \frac{-A_{\mathrm{u},1}+A_{\mathrm{u},2}-A_{\mathrm{d}}}{A_{\mathrm{u},1}+A_{\mathrm{u},2}+A_{\mathrm{d}}} & \frac{2A_{\mathrm{d}}}{A_{\mathrm{u},1}+A_{\mathrm{u},2}+A_{\mathrm{d}}} \\ \frac{2A_{\mathrm{u},1}}{A_{\mathrm{u},1}+A_{\mathrm{u},2}+A_{\mathrm{d}}} & \frac{2A_{\mathrm{u},2}}{A_{\mathrm{u},1}+A_{\mathrm{u},2}+A_{\mathrm{d}}} & \frac{-A_{\mathrm{u},1}-A_{\mathrm{u},2}+A_{\mathrm{d}}}{A_{\mathrm{u},1}+A_{\mathrm{u},2}+A_{\mathrm{d}}} \end{bmatrix}}_{\text{Scattering Matrix } \mathbf{SM}} \begin{bmatrix} \widehat{f}_{\mathrm{u},1} \\ \widehat{f}_{\mathrm{u},2} \\ \widehat{g}_{\mathrm{d}} \end{bmatrix} \tag{2.51}$$

The individual **SM** elements represent the reflection and transmission coefficients R and T of the ports. In Chapter 3, a similar form of the 3-port junction is described to determine the lean secondary zone as a network element.

2.6 Flame Dynamics

In order to predict thermoacoustic oscillations in gas turbine combustors or jet engines, the precise characterization of the frequency-dependent heat-release source term of the flame is essential. Flame transfer functions (FTFs) are employed as part of this endeavor to quantify the dynamic flame response to acoustic perturbations. The following will describe the FTF, including its fundamental underlying assumptions.

2.6.1 Flame Transfer Function

The FTF characterizes the frequency-dependent response of a flame to a disturbance or excitation upstream of the flame location. In the context of perfectly premixed flames, the FTF is characterized as the quotient of relative heat release rate oscillations to relative velocity or mass flow perturbations at a designated reference location $(\,)_{\mathrm{ref}}$, which is typically located at the inlet of the combustion chamber. The heat release rate and velocity/mass flow perturbations are normalized with their respective mean values, resulting in a dimensionless quantity:

$$FTF(\omega) = \frac{\dot{Q}'(\omega)/\overline{\dot{Q}}}{u'_{\mathrm{ref}}(\omega)/\bar{u}_{\mathrm{ref}}} \tag{2.52}$$

Assuming that the flame is, on average, a linear, time-invariant system, these fluctuations can be represented as harmonic oscillations at a certain angular frequency ω. They can be expressed using the complex-valued Fourier transformed:

$$\dot{Q}'(\omega) = \widehat{\dot{Q}}(\omega)e^{\left(i\omega t+\varphi_{\dot{\mathrm{Q}}}\right)} \tag{2.53}$$

$$u'_{\mathrm{ref}}(\omega) = \widehat{u}_{\mathrm{ref}}(\omega)e^{\left(i\omega t+\varphi_{\mathrm{u_{ref}}}\right)} \tag{2.54}$$

The FTF can thus be decomposed into a frequency-dependent amplitude $\widehat{FTF}$ and phase $\angle\widehat{FTF}$.

$$\widehat{FTF}(\omega) = \frac{\widehat{\dot{Q}}/\overline{\dot{Q}}}{\widehat{u}_{\mathrm{ref}}/\overline{u}_{\mathrm{ref}}} \tag{2.55}$$

$$\angle\widehat{\mathrm{FTF}}(\omega) = \varphi_{\dot{\mathrm{Q}}} - \varphi_{\mathrm{u_{ref}}} \tag{2.56}$$

From a systems theory perspective, the FTF represents the transfer function of a Single-Input-Single-Output (SISO) system. Regarding the formation of thermoacoustic instabilities, the FTF contains precisely the information, which decisively influences the stability of a combustion system. The amplitude of the FTF describes, concerning the loss or damping effects of the combustion system, whether the acoustic field quantities

experience an energy source or sink due to the flame dynamics. Together with the acoustics of the combustion system, the phase of the FTF determines the frequency ranges in which constructive or destructive superposition of the pressure and heat release fluctuations occurs and whether thermoacoustic combustion instabilities can form in principle. Convective transport processes largely determine the dynamic flame behavior in thermoacoustic combustion systems. An oscillation of the mass flow (premixed fuel-air or reactive hot gases) at the reference combustion chamber inlet causes an oscillation of the heat release in the combustion chamber. However, these two oscillations exhibit a characteristic time delay resulting from the convective transport of the oscillation from the reference plane to the main reaction zone of the flame. This time delay is essentially a function of the distance between the main reaction zone and the reference plane, as well as the mean transport velocity along this distance. The phase of the FTF can consequently be approximated as a function of this time delay τ [56,57].

$$\angle\widehat{\mathrm{FTF}}(\omega) \approx -\omega\tau \tag{2.57}$$

This description of the phase of the FTF represents a very good approximation from a global point of view. This allows the derivation of limit values of the FTF for particularly small and high frequencies. Low frequency limits $\omega \to 0$ for perfectly premixed combustion are listed below:

$$\lim_{\omega\to 0} \; |\widehat{\mathrm{FTF}}| \; = 1 \tag{2.58}$$

$$\lim_{\omega\to 0} \; \angle\widehat{\mathrm{FTF}} \; = 0 \tag{2.59}$$

For small frequencies, the flame reacts quasi-stationary to fluctuations in the reference plane. The velocity fluctuation at the reference plane causes a fluctuation in the heat release rate of the same magnitude in proportion [58]. Consequently, a negligible phase difference results for periods significantly larger than the convective delay time τ. Partially premixed flames are very common in technical applications. Here

fluctuations of the equivalence ratio can also cause heat release rate oscillations. These are superimposed on velocity fluctuations caused by an oscillating fuel mass flow, mostly at the injector, and have different low frequency limits [54,56,59,60].

For high frequencies, especially the spatial distribution of heat release causes an increasing dispersion of the flame response, resulting in a decreasing and eventually vanishing amplitude of the FTF. From a mathematical point of view, the phase of the FTF would continue to decrease with increasing frequency and tend towards minus infinity. However, meaningful phase values can only be determined up to a frequency where the flame response still has sufficient amplitude. These limit values can be used as an evaluation criterion for verifying the dynamic flame behavior. In addition, fulfilling these limit values is a prerequisite for the validity of model approaches.

2.6.2 Rankine-Hugoniot Jump Condition for Acoustic Perturbations

The Rankine-Hugoniot conditions are one-dimensional integral conditions describing mass, momentum, and energy conservation across a discontinuity - in the present case, a flame. This discontinuity can be modeled to be at rest or in motion. For the derivation, it is assumed that the heat source is a flame in a quasi-1D flow configuration and is positioned between the cold reactants upstream (subscript $(\,)_\mathrm{c}$) and the hot combustion products downstream (subscript $(\,)_\mathrm{h}$) [61]. Considering a wavelength much larger than the axial flame expansion, the flame can be treated as an acoustically compact network element with $N = 2$ ports. The Rankine Hugoniot relations have been used many times and were derived in different ways [61–65]. Tho following derivation is strongly based on the given literature. The relevant governing equations for mass,

momentum, and energy across the flame are given as follows :

$$\rho_h u_h - \rho_c u_c = 0 \tag{2.60}$$

$$p_h + \rho_h u_h^2 - p_c - \rho_c u_c^2 = 0 \tag{2.61}$$

$$\rho_h u_h^2 \left(h_h + \frac{u_h^2}{2} \right) - \rho_c u_c^2 \left(h_c + \frac{u_c^2}{2} \right) - \dot{Q} = 0 \tag{2.62}$$

Here $\dot{Q}$ is the heat release rate of the flame over the flame surface and h is the specific enthalpy. Assuming a stationary, isentropic, one-dimensional flow field upstream and downstream of the flame the specific enthalpy is expressed by the ideal gas law ($p = \rho \mathbb{R} T$) with the specific gas constant $\mathbb{R}$:

$$h = c_p T = \frac{\gamma}{\gamma - 1} \frac{p}{\rho} \tag{2.63}$$

In addition, the state equation can be formulated:

$$\frac{\rho_h \mathbb{R} T_h}{p_h} - \frac{\rho_c \mathbb{R} T_c}{p_c} = 0 \tag{2.64}$$

Introducing the Mach-number $M = {}^{u}/_{c}$ and rearranging the Eqs. 2.60 - 2.64 leads to the Rankine-Hugoniot equations across a flame [61, 64, 66]:

$$\frac{u_h}{u_c} = 1 + \frac{\gamma - 1}{\gamma} \frac{\dot{Q}}{p_c u_c} \tag{2.65}$$

$$\frac{p_h}{p_c} = 1 - (\gamma - 1) \frac{\dot{Q}}{p_c u_c} M_c^2 \tag{2.66}$$

$$\frac{T_h}{T_c} = \left(\frac{c_h}{c_c} \right)^2 = 1 + \frac{\gamma - 1}{\gamma} \frac{\dot{Q}}{p_c u_c} \tag{2.67}$$

Note that low Mach-numbers have been assumed; only terms up to 1^{st} order are retained, and higher order terms are neglected. These relations are now linearized for small acoustics fluctuations. Splitting the variables p, ρ, u and the heat release rate $\dot{Q}$ into mean and fluctuating quantities leads to two equations for the acoustic pressure and velocity

downstream of the flame:

$$p'_{\mathrm{h}} = p'_{\mathrm{c}} - \overline{\rho}_{\mathrm{c}} c_{\mathrm{c}} \left(\frac{T_{\mathrm{h}}}{T_{\mathrm{c}}} - 1 \right) M_{\mathrm{c}} \overline{u}_{\mathrm{c}} \left(\frac{\dot{Q}'}{\overline{\dot{Q}}} + \frac{u'_{\mathrm{c}}}{\overline{u}_{\mathrm{c}}} \right) \tag{2.68}$$

$$u'_{\mathrm{h}} = u'_{\mathrm{c}} + \left(\frac{T_{\mathrm{h}}}{T_{\mathrm{c}}} - 1 \right) \overline{u}_{\mathrm{c}} \left(\frac{\dot{Q}'}{\overline{\dot{Q}}} - \frac{p'_{\mathrm{c}}}{\overline{p}_{\mathrm{c}}} \right). \tag{2.69}$$

A more convenient expression is found by introducing the following ratios for the temperatures and specific impedance:

$$\mathbb{A} = \left(\frac{T_{\mathrm{h}}}{T_{\mathrm{c}}} - 1 \right) \quad \mathbb{B} = \frac{(\overline{\rho} c)_{\mathrm{h}}}{(\overline{\rho} c)_{\mathrm{c}}} \tag{2.70}$$

The Eqs. 2.68 and 2.69 can then be written as:

$$\frac{p'_{\mathrm{h}}}{\overline{\rho}_{\mathrm{h}} c_{\mathrm{h}}} = \mathbb{B} \frac{p'_{\mathrm{c}}}{\overline{\rho}_{\mathrm{c}} c_{\mathrm{c}}} - \mathbb{B}\mathbb{A} M_{\mathrm{c}} u'_{\mathrm{c}} \left(1 + \frac{\dot{Q}' / \overline{\dot{Q}}}{u'_{\mathrm{c}} / \overline{u}_{\mathrm{c}}} \right) \tag{2.71}$$

$$u'_{\mathrm{h}} = -\mathbb{A}\gamma M_{\mathrm{c}} \frac{p'_{\mathrm{h}}}{\overline{\rho}_{\mathrm{c}} c_{\mathrm{c}}} + \left(1 + \mathbb{A} \frac{\dot{Q}' / \overline{\dot{Q}}}{u'_{\mathrm{c}} / \overline{u}_{\mathrm{c}}} \right) u'_{\mathrm{c}} \tag{2.72}$$

With the FTF definition according to Eq. 2.52 and using the transfer matrix notation for 2-port elements with the acoustic pressure and velocity yields the following equation for the so-called flame transfer matrix (**FTM**):

$$\begin{bmatrix} \frac{p'}{\overline{\rho} c} \\ u' \end{bmatrix}_{\mathrm{h}} = \underbrace{\begin{bmatrix} \mathbb{B} & -\mathbb{B}\mathbb{A} M_{\mathrm{c}} (1 + FTF) \\ -\mathbb{A}\gamma M_{\mathrm{c}} & 1 + \mathbb{A} FTF \end{bmatrix}}_{\mathbf{FTM}} \begin{bmatrix} \frac{p'}{\overline{\rho} c} \\ u' \end{bmatrix}_{\mathrm{c}} \tag{2.73}$$

The flame transfer matrix can be used to implement the dynamic response of a flame into an acoustic network system. It can be coupled to other elements via its upstream or downstream port as used in Chapter 3.

3 MISO Network Approach for the Lean Secondary Zone

The network element technique is a well-known tool for identifying and describing the thermoacoustic properties of combustion systems, e.g. [49,62]. In such a network, the thermoacoustic element describes the functional relations between the acoustic variables, e.g., acoustic pressure p' and acoustic velocity u', at its ports based on the conservation equations and element specific transfer functions. The latter represents, for example, acoustic losses of ducts, junctions, and injectors or the dynamic flame response. In many simple cases, these elements consist of two in- and outputs and can be referred to as 2-port systems. Nevertheless, the approach is not restricted in the number of inputs, and for elements with more than two ports ($N > 2$), so-called N-ports are possible as derived by Lavrentjev and Åbom [67]. Any linear time-invariant N-port can be described by relating the input state variables to the corresponding output variables.

By selecting the reference location of the ports as shown in Fig. 3.1 on the upper left, the compact RQL combustor can be considered as a 2-port system (Ⓐ-Ⓐ). In this arrangement, the flame dynamics of the primary and secondary zones are inseparable. To identify the individual parts of flame dynamics, the zones of the RQL combustor are separated, as seen in Fig. 3.1 on the upper right. The secondary zone of the separated RQL forms an N-port system with $N = 3$ connecting the flow from the primary zone and the secondary mixing air flow to the combustor outlet (Ⓒ-Ⓒ). This system can be modeled as a network consisting of a 3-port with an adjoining 2-port flame, as shown in the lower part of Fig. 3.1, where the 3-port represents the acoustic system behavior, and the flame element describes the heat release. State ① represents the upstream $(\,)_{\mathrm{u}}$

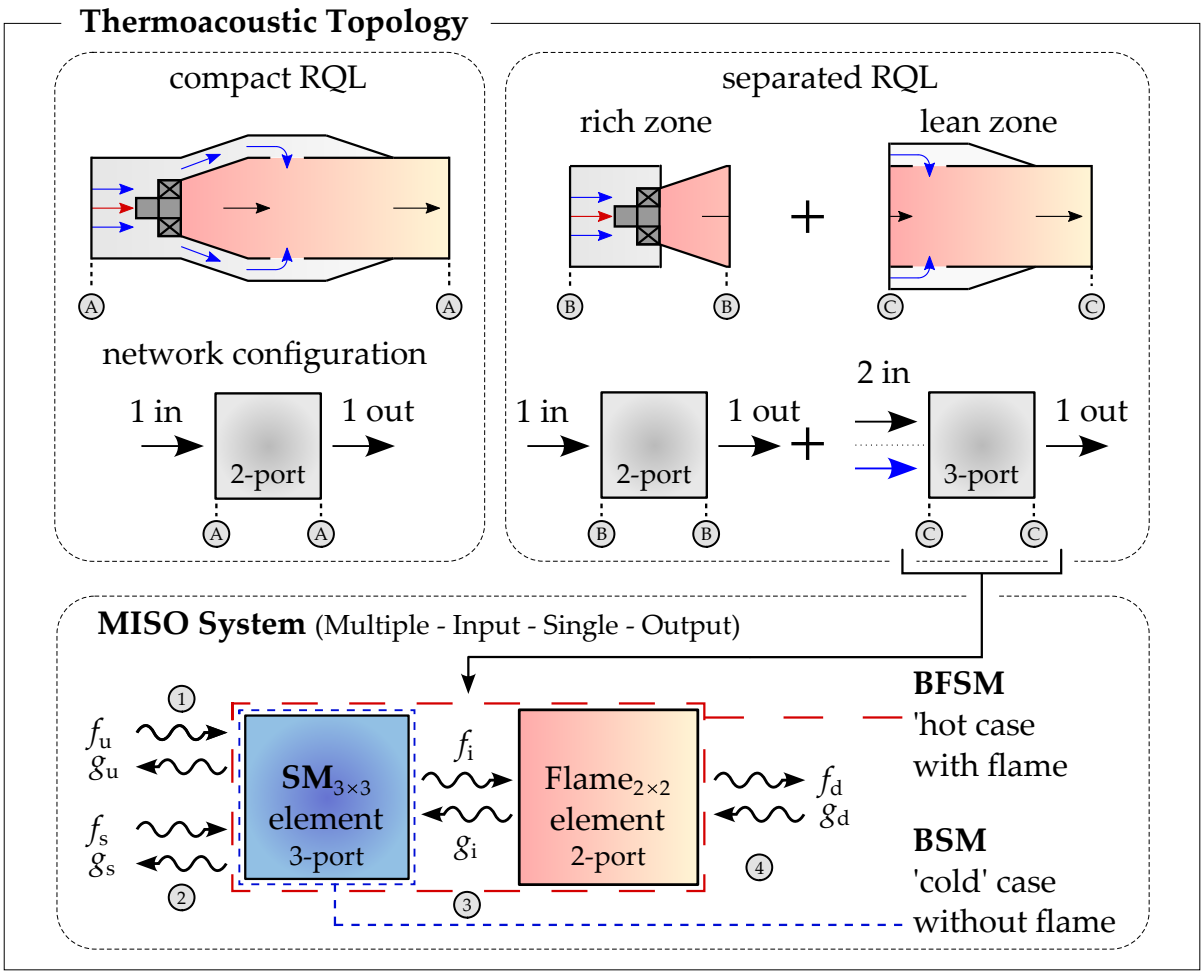

Figure 3.1: Top: Comparison of combustion chamber topology between compact and separated arrangement in terms of a network element approach; bottom: MISO (Multiple-Input-Single-Output) approach for the secondary zone as a network system of a 3×3 scattering matrix (**SM**) and a 2×2 flame element.

state at the end of the primary zone, ② represents the state of the mixing air added through the side mixing air jets $(\,)_s$, ③ is the virtual intermediate $(\,)_i$ coupling state and ④ represents the state downstream $(\,)_d$ of the lean secondary zone.
Karlsson and Åbom [68] and Holmberg et al. [69] introduced a technique where a 3-port can be evaluated with a 3×3 scattering matrix represent-

ing the reflection R and transmission T coefficients of the system for the selected state variables. With the application to thermoacoustics in RQL combustors in mind, it is convenient to introduce the acoustic Riemann invariants $\widehat{f}$ and $\widehat{g}$ as state variables to describe the network elements in terms of harmonic acoustic disturbances that propagate in co-flow and counter-flow direction. This leads to the following representation of a 3-port where subscripts $(\,)_{u,s,i}$ refer to the corresponding ports of the disturbances at the system boundary, see the lower part of Fig. 3.1:

$$\begin{bmatrix} \widehat{g}_u \\ \widehat{g}_s \\ \widehat{f}_i \end{bmatrix} = \underbrace{\begin{bmatrix} R_u & T_{s,u} & T_{i,u} \\ T_{u,s} & R_s & T_{i,s} \\ T_{u,i} & T_{s,i} & R_i \end{bmatrix}}_{\mathbf{SM}_{fg,3\times3}} \begin{bmatrix} \widehat{f}_u \\ \widehat{f}_s \\ \widehat{g}_i \end{bmatrix} \tag{3.1}$$

Adding the Rankine-Hugoniot 2-port type element to the network system results in a compact arrangement for the $\mathbf{SM}_{fg,3\times3}$ and the 2×2 flame element with coupling intermediate state variables $\widehat{f}_i$ and $\widehat{g}_i$. The Rankine-Hugoniot jump conditions are one-dimensional integral conditions describing mass, momentum and energy conservation across a discontinuity - here a flame [61]. Applying the jump condition to the presented case, using the speed of sound c, the Mach number M, leads to:

$$\begin{aligned} \begin{bmatrix} \widehat{f}_d \\ \widehat{g}_d \end{bmatrix} = \frac{1}{2} \begin{bmatrix} \mathbb{B} - \mathbb{A}\gamma M_i + 1 \\ \mathbb{B} + \mathbb{A}\gamma M_i - 1 \end{bmatrix} & \\ \begin{bmatrix} \mathbb{B} - \mathbb{A}\gamma M_i - 1 & \mathbb{A}\overline{u}_i \\ \mathbb{B} + \mathbb{A}\gamma M_i + 1 & -\mathbb{A}\overline{u}_i \end{bmatrix} & \begin{bmatrix} \widehat{f}_i \\ \widehat{g}_i \\ \dot{Q}'/\overline{\dot{Q}} \end{bmatrix} \\ \mathbb{A} = \left(\frac{T_d}{T_i} - 1 \right) \quad \mathbb{B} = \frac{(\overline{\rho}c)_i}{(\overline{\rho}c)_d} & \end{aligned} \tag{3.2}$$

The subscript $(\,)_i$ denotes variables upstream, and $(\,)_d$ denotes quantities downstream of the flame. The downstream acoustic quantities are related to the upstream fluctuations through mean flow quanti-

ties ($T_\mathrm{i}, T_\mathrm{d}, \bar{u}_\mathrm{i}$) and heat release fluctuations $\dot{Q}'$. Following the well-established method for 2-port elements (e.g. [70–73]), the dynamic flame response is often quantified with an FTF. In the case of velocity coupled flame response, the definition of the FTF is given as the normalized heat release fluctuation $\dot{Q}'/\overline{\dot{Q}}$ divided by a normalized reference velocity fluctuation $u'_\mathrm{ref}/\overline{u}_\mathrm{ref}$. As two flows enter the lean secondary zone, both are considered to contribute to the heat release fluctuations. The secondary zone can be seen as a Multiple-Input-Single-Output (MISO) network system. It is assumed that the individual contributions of the two velocity fluctuations from upstream u'_u and the side mixing air jets u'_s, on the unsteady heat release rate can be linearly superposed and quantified by individual FTFs [65, 74]. For the linear case, the heat release rate fluctuations can be expressed as two SISO FTFs:

$$\frac{\dot{Q}'}{\overline{\dot{Q}}} = FTF_\mathrm{u,M}\frac{u'_\mathrm{u}}{\overline{u}_\mathrm{u}} + FTF_\mathrm{s,M}\frac{u'_\mathrm{s}}{\overline{u}_\mathrm{s}} \tag{3.3}$$

$$= FTF_\mathrm{u,M}\frac{\widehat{f}_\mathrm{u} - \widehat{g}_\mathrm{u}}{\overline{u}_\mathrm{u}} + FTF_\mathrm{s,M}\frac{\widehat{f}_\mathrm{s} - \widehat{g}_\mathrm{s}}{\overline{u}_\mathrm{s}} \tag{3.4}$$

Thereby, $FTF_\mathrm{u,M}$ and $FTF_\mathrm{s,M}$ are the complex-valued flame transfer functions of each input. This MISO approach is particularly useful for separating the physical mechanisms adding to the system's behavior.

For validation purposes, the starting point of the modeling must be understood. It is important to examine the impact of the linearity assumption and how it affects the FTFs. Equation 3.4 is interpreted as a vector space with base vectors $(FTF_\mathrm{u,M}{}^{u'_\mathrm{u}}/\overline{u}_\mathrm{u})$ and $(FTF_\mathrm{s,M}{}^{u'_\mathrm{s}}/\overline{u}_\mathrm{s})$. By definition of the linearized momentum flux ratio

$$\frac{J'}{\overline{J}} = 2\left(\frac{u'_\mathrm{u}}{\overline{u}_\mathrm{u}} - \frac{u'_\mathrm{s}}{\overline{u}_\mathrm{s}}\right) \quad , \tag{3.5}$$

the relationship between the velocity fluctuations is known. Considering the limit case of small infinitesimal changes in the absolute phase difference between both harmonic fluctuations $(J'/\overline{J} \to 0)$, the phase difference

of the velocity fluctuations has to become $d\varphi_{u-s} = \pi$ for Eq. 3.5 to be valid. Since the phase vectors of the velocity fluctuations point in opposite directions, the vector space used to represent the heat release rate fluctuations is defined by the complex valued FTFs. In the case of stable operation and no heat release rate fluctuations $\dot{Q}'/\overline{\dot{Q}} = 0$, the right-hand side of Eq. 3.4 must turn zero. This is only the case if the scalar product of both vectors becomes zero and the vectors are orthogonal:

$$FTF_{\mathrm{u,M}} \cdot FTF_{\mathrm{u,M}} \stackrel{!}{=} 0 \tag{3.6}$$

This implies that both complex valued FTFs must have an absolute phase difference of 90° or $\pi/2$ to satisfy Eq. 3.6:

$$|\angle FTF_{\mathrm{u,M}} - \angle FTF_{\mathrm{s,M}}| \stackrel{!}{=} 90° = \pi/2 \tag{3.7}$$

Inserting Eq. 3.4 into 3.2 and eliminating $\widehat{f}_{\mathrm{i}}$ and $\widehat{g}_{\mathrm{i}}$ and by substituting the resulting formulation into Eq. 3.1 leads to a 3×3 matrix (called $\mathbf{BFSM}^{MISO}$) including the reflection and transmission coefficients, temperatures before and after the flame, and the desired FTFs:

$$\begin{bmatrix} \widehat{g}_{\mathrm{u}} \\ \widehat{g}_{\mathrm{s}} \\ \widehat{f}_{\mathrm{d}} \end{bmatrix} = \mathbf{BFSM}^{MISO} \begin{bmatrix} \widehat{f}_{\mathrm{u}} \\ \widehat{f}_{\mathrm{s}} \\ \widehat{g}_{\mathrm{d}} \end{bmatrix} \tag{3.8}$$

The $\mathbf{BFSM}^{MISO}$ is evaluated in Chapter 8, and the condition given by Eq. 3.7 is carefully examined. A detailed description of the complete matrix and all matrix elements is supplied in the Appendix. The detailed procedure for obtaining the coefficients and measurements performed is given in Section 6.6. To determine the desired complex valued $FTF_{\mathrm{u,M}}$ and $FTF_{\mathrm{s,M}}$ from acoustic measurements, a regression algorithm is applied. Genetic algorithms (GA) in particular, have proven robust in finding the optimum solutions for various engineering optimization problems [75]. GA do not rely on gradients and has superior parameter search patterns. The GA is applied to the resulting MISO optimization problem $\mathbf{BFSM}^{MISO}$.

4 Model of Convective Time Delay

For the presented JIC, it is assumed that induced disturbances propagate within the shear layer of the inverse diffusion flame. Inverse means that the fuel mass flow is entrained while the air forms the jet. A first-order physical model of the convective time delay of a perturbation traveling in the reactive shear layer of the secondary air jets is developed. The model is used to verify the presented FTF phase response and provides the interpretation of the variation of the phase time delay τ with the operating conditions as seen in the flame response measurements. Thereby, the phase time delay is defined as follows:

$$\tau = \frac{\varphi}{2\pi \cdot f} \tag{4.1}$$

Even with forcing from two different locations, upstream and the mixing jets, both fluctuations cause a convectively transported disturbance growing from the edge of the mixing air jets along the shear-layer into the flame. In this case, it can be expected that the time delay of both FTFs is identical $\tau_u = \tau_s$ and represents the gradient of the phase response of the FTFs.

It is assumed that the time delay scales with the length of the flame L_F and the convective velocity of perturbations in the reactive shear layer u_{con}:

$$\tau = \frac{L_F}{u_{con}} \tag{4.2}$$

Combustion in the secondary zone takes the form of a turbulent inverse jet diffusion flame. For these characteristics, expressions for the flame length L_F and the convection velocity u_{con} will be derived next. The fuel is given by the non-oxidized components of the hot gas mass flow from the rich primary zone $\dot{m}_{pr} = \dot{m}_f + \dot{m}_{air,pz}$ where $\dot{m}_f$ is the fuel mass flow

rate and $\dot{m}_{\text{air,pz}}$ the air mass flow rate of the primary zone of the RQL combustor. As seen from the experiment, the reaction of the primary flow starts quasi-instantaneously when in contact with the secondary air. Thus, it is reasonable to assume that the reaction in the secondary zone will occur in a region close to the stoichiometric mixture fraction of the primary flow with secondary air. For simplicity the stoichiometric air ratio of the primary flow $l_{\text{min,p}} = \frac{\dot{m}_{\text{air,pz,st}}}{\dot{m}_{\text{pr}}}$ is expressed in terms of the primary zone equivalence ratio ϕ_{pz} and the stoichiometric air ratio $l_{\text{min}} = \frac{\dot{m}_{\text{a,st}}}{\dot{m}_{\text{f}}}$:

$$\begin{aligned} l_{\text{min,p}} &= \frac{\dot{m}_{\text{air,st}} - \dot{m}_{\text{air,pz}}}{\dot{m}_{\text{pr}}} \\ &= \frac{l_{\text{min}} - l_{\text{min}}/\phi_{\text{pz}}}{1 + l_{\text{min}}/\phi_{\text{pz}}} \\ &= l_{\text{min}} \frac{1 - 1/\phi_{\text{pz}}}{1 + l_{\text{min}}/\phi_{\text{pz}}} \end{aligned} \tag{4.3}$$

The stoichiometric mixture fraction of the secondary combustion zone is defined as follows:

$$\begin{aligned} f_{\text{pr,st}} &= \frac{\dot{m}_{\text{pr}}}{\dot{m}_{\text{pr}} + \dot{m}_{\text{air,pz,st}}} \\ &= \frac{1}{1 + l_{\text{min,p}}} \\ &= \frac{1 + l_{\text{min}}/\phi_{\text{pz}}}{1 + l_{\text{min}}} \end{aligned} \tag{4.4}$$

The model for L_{F} is obtained by considering the entrainment of turbulent jets according to Hasselbrink and Mungal [76]:

$$\frac{\dot{m}(x)}{\dot{m}_0} = C_{\text{ent}} \cdot \frac{x}{d_{\text{eff}}} \left(\frac{\rho_\infty}{\rho_{\text{jet}}} \right)^{1/2} \tag{4.5}$$

For the turbulent inverse diffusion flame, the radially inward entrain-

ment of ambient fluid is connected with the equivalent radially outward transport of jet fluid in the shear layer by the shear layer turbulence. When the stoichiometric amount of air for the primary mass flow rate $l_{\mathrm{min,p}}\dot{m}_{\mathrm{pr}}$ has been entrained, the flame length is reached. Thus it can be written as:

$$\frac{l_{\mathrm{min}}\dot{m}_{\mathrm{f}} - \dot{m}_{\mathrm{air,pz}}}{\dot{m}_{\mathrm{air,sz}}} = C_{\mathrm{ent}} \cdot \frac{L_{\mathrm{F}}}{d_{\mathrm{jet,eff}}} \left(\frac{\rho_{\infty}}{\rho_{\mathrm{jet}}}\right)^{1/2} \tag{4.6}$$

The jet entrainment coefficient C_{ent} can be obtained according to Lawn [77]:

$$C_{\mathrm{ent}} = \frac{2 \cdot \alpha_{\mathrm{c}}}{\beta_{\mathrm{c}}} \tag{4.7}$$

The axial scalar decay α_{c} and the radial scalar spread β_{c} are empirical constants determined in the literature from measurement results. In the review of Lawn [77], the values of various authors are presented as $\alpha_{\mathrm{c}} = 8.9 - 10.1$ and $\beta_{\mathrm{c}} = 56 - 67$. While the entrainment coefficient Eq. 4.7 applies strictly only to the jet's similarity region, it also allows approximation of the entrainment in the core region. The flame length L_{F} can be estimated from the primary hot gas mass flow rate $\dot{m}_{\mathrm{pr}} = \dot{m}_{\mathrm{f}} + \dot{m}_{\mathrm{air,pz}}$, the secondary air mass flow rate $\dot{m}_{\mathrm{air,sz}}$, and the momentum flux ratio J, resulting in:

$$\begin{aligned} L_{\mathrm{F}} &= \frac{d_{\mathrm{jet,eff}}}{C_{\mathrm{ent}}} \left(\frac{\rho_{\infty}}{\rho_{\mathrm{jet}}}\right)^{-1/2} \frac{l_{\mathrm{min,p}}\dot{m}_{\mathrm{pr}}}{\dot{m}_{\mathrm{air,sz}}} \\ &= \frac{d_{\mathrm{jet,eff}}}{C_{\mathrm{ent}}} \left(\frac{\rho_{\infty}}{\rho_{\mathrm{jet}}}\right)^{-1/2} \frac{l_{\mathrm{min}}\dot{m}_{\mathrm{f}} - \dot{m}_{\mathrm{air,pz}}}{\dot{m}_{\mathrm{air,sz}}} \end{aligned} \tag{4.8}$$

In the core region of the jet, the transport velocity u_{con} can be estimated from the stoichiometric mass fraction $f_{\mathrm{pr,st}}$. For the considered inverse diffusion flame, the equivalent jet mass fraction $f_{\mathrm{jet,st}} = 1 - f_{\mathrm{pr,st}}$ is introduced to linearly interpolate between the core velocity $u_{\mathrm{jet}} = \frac{\dot{m}_{\mathrm{air,sz}}}{\rho_{\mathrm{jet}} A_{\mathrm{jet}}}$ and the part of crossflow velocity parallel to the jet. As the primary zone

crossflow u_∞ and u_{jet} are at 90° this velocity is neglected:

$$u_{\text{con}} \approx f_{\text{jet,st}} \cdot u_{\text{jet}} \tag{4.9}$$

In a turbulent jet's fully developed shear layers, scalar spreading is significantly faster than the distribution of specific momentum. This is considered by the turbulent Schmidt number Sc_t. Moving into the shear layer for more significant entrainment for the weighting of u_{jet} with $f_{\text{jet,st}}$, a correction factor should be applied to ensure accuracy. For JIC with momentum flux ratio $J = 8 - 72$, He et al. [79] found Schmidt numbers of $Sc_t = 0.2 - 0.5$ to fit well with experimental data. For simplicity in this work, an exponential function of $f_{\text{jet,st}}$ is used to determine the Schmidt number for each OP:

$$Sc_{\text{t}} = \max\left[C_{\text{u}} f_{\text{jet,st}} \exp(-a_{\text{Sc}} f_{\text{jet,st}}), 0.728\right] \tag{4.10}$$

Here $C_{\text{u}} = 1.3$ and $a_{\text{Sc}} = 1.15$ were derived from measurements at each operating point, to arrive at Schmidt numbers of $Sc_{\text{t}} = 0.136 - 0.402$. For the convective velocity, it follows:

$$u_{\text{con}} = \frac{f_{\text{jet,st}}}{Sc_t} \cdot u_{\text{jet}} \tag{4.11}$$

With the flame length L_{F} from Eq. 4.8 and the convective velocity u_{con} from Eq. 4.11, the time delay τ is calculated using Eq. 4.2. Table 4.1 summarizes the resulting parameters for the operating range, which is discussed in Chapter 6.

Table 4.1: Time delay model parameters for the different mixing air jet configurations and operating points.

OP	L_F [m]	u_{con} [m/s]	τ [ms]
OP1	0.0327	8.28	3.953
OP2	0.0249	6.69	3.728
OP3	0.0178	5.05	3.540
OP4	0.0114	3.37	3.387
OP5	0.0328	8.83	3.719
OP6	0.0179	4.75	3.768
OP7	0.0111	3.00	3.708
OP8	0.0278	5.46	5.094
OP9	0.0250	6.69	3.744
OP10	0.0145	19.33	0.750

5 RQL Combustor Facility

The experiments were performed on the RQL test rig depicted in Fig. 5.1. The test rig operates at atmospheric pressure in a thermal power range of 45 – 80kW and offers full optical access and application of

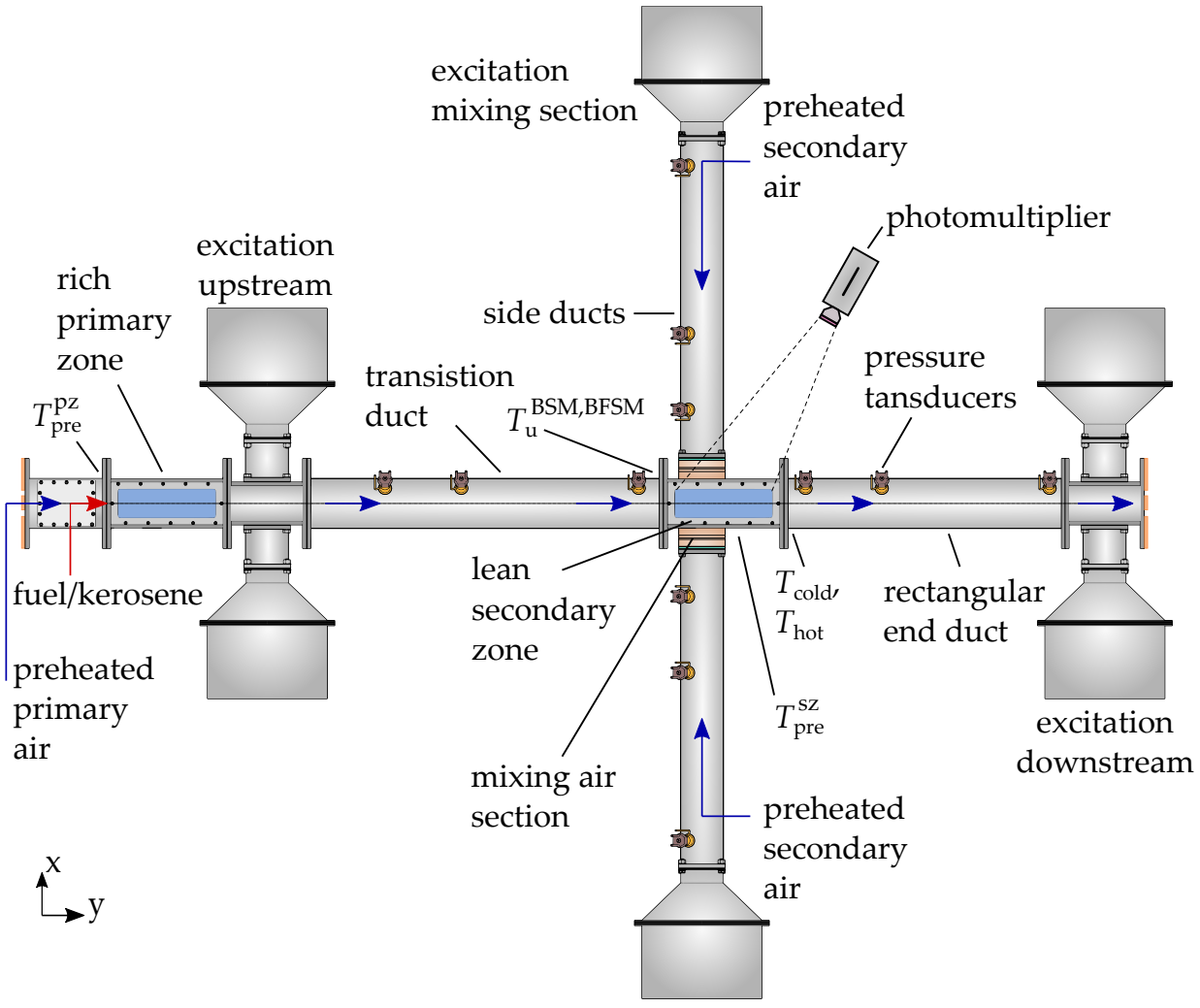

Figure 5.1: Atmospheric RQL test rig; top view of the setup for the investigation of the secondary zone.

intrusive measurement methods to the combustion zones. The design of the test rig is modular, which permits the investigation of the test stand acoustics using various setups. The topology of the test rig is explained in detail in the following paragraphs, with specific focus on key components and parts of the design strategy, such as the acoustic and thermal design of the central ducts, the mixing air section's variability, the jet nozzle parameters, and ensuring ignition in the lean secondary zone.

The primary and secondary air mass flows are separately measured and controlled. In order to approximate the conditions encountered in full-scale engines, it is possible to employ two electric preheaters to elevate the air temperature at the burner inlet in the primary zone and at the inlet of the mixing air segment. These preheaters can deliver operating air temperatures of $423 - 523\,\mathrm{K}$ and are fitted with thermocouples to ensure temperatures do not exceed safe limits. The primary air flow enters the test rig on the left with a constant inlet temperature of T_{pre}^{pz}, measured with a Type-K thermocouple as indicated in Fig. 5.1. The primary combustion chamber has a 90x90 mm^2 square cross-section and a total length of $l_{\mathrm{cc}} = 0.28\,\mathrm{m}$. It is equipped with a generic fuel injector and can operate using both kerosene or gaseous fuel. The upstream excitation element with two loudspeakers (Type: Eminence Kappa 12in) follows the primary combustion chamber. The transition duct with a length of $l_{\mathrm{td}} = 0.96\,\mathrm{m}$ and a diameter $d_{\mathrm{td}} = 0.117\,\mathrm{m}$ is used to reconstruct the 1D acoustic field and connects the excitation element to the lean secondary combustion chamber. Three dynamic pressure transducers are mounted at a non-equidistant spacing to ensure high-quality wavefield reconstruction with the MMM in the transition duct [50, 51, 80, 81].

The lean secondary combustion chamber has a geometry similar to the primary zone with 90x90 mm^2, $l_{\mathrm{cc}} = 0.28\,\mathrm{m}$ and is optically accessible. The preheated secondary air T_{pre}^{sz} is measured with a Type-K thermocouple and enters the test rig through the two side ducts mounted to the secondary zone. The side ducts with a length of $l_{\mathrm{side}} = 0.85\,\mathrm{m}$ and a diameter of $d_{\mathrm{side}} = 0.112\,\mathrm{m}$ are used for the MMM technique

and are connected to the lean combustion chamber via the mixing air section shown in Fig. 5.2. The jet geometry, the number of rows, and the pattern within the mixing air section can be varied using inserts. Compared to the investigated low-frequency range wavelength, the inserts are expected to be compact. Acoustic excitation of the mixing jets and application of the MMM is possible on both sides of the chamber with loudspeakers at the end of the side ducts. The secondary zone is followed by a rectangular end duct with the same side length as the combustion chamber and a total length of $l_{\mathrm{ed}} = 0.92\,\mathrm{m}$. Non-equidistant spaced pressure transducers are mounted, and a downstream excitation element is used to perform acoustic forcing.

The test rig outlet can be equipped with various end terminations, such as perforated plates with orifices that reduce the reflection of low-frequency acoustic waves [82]. The reflection coefficient of an open end can be significantly reduced by installing an orifice or perforated plate whose area contraction ratio is equal to the Mach number of the flow in the orifice or plate. The acoustic energy is converted into vortices shedding from the edges of the orifice [82].

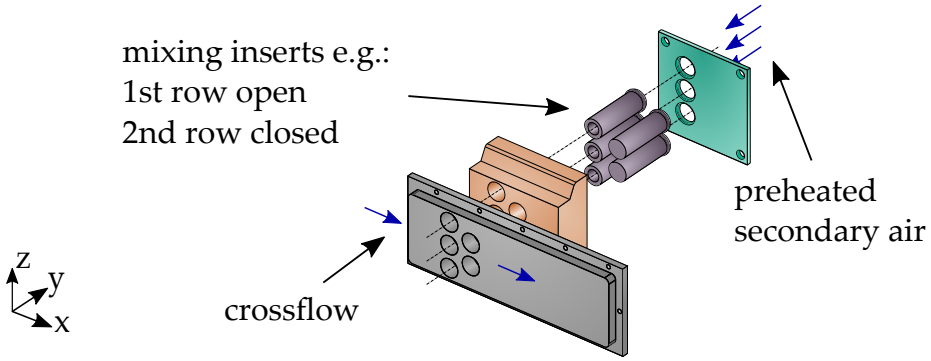

Figure 5.2: Mixing air section setup and view of variable mixing inserts.

5.1 Mixing Air Section and Jet Geometries

The mixing air sections, which house the mixing inserts, are located on the left and right-hand sides of the secondary combustion chamber. The mounting and positioning of the mixing sections and inserts are illustrated in Fig. 5.2 and Fig. 5.3, respectively. Each section can hold up to five mixing inserts, with a maximum diameter of $d_{\text{jet,max}} = 27$ mm. Various arrangements can be achieved with these inserts, such as opposing single row (first or second row only) or opposing two rows staggered. Figure 5.2 shows a one-row setup with six inserts. Unused ports can be closed with plugs. Orifice plates can also be used to control the acoustic boundary conditions before the mixing inserts, as shown in Fig. 5.2. The plates hold the inserts in place and prevent them from vibrating. The inserts are assumed to be compact, with a length of $l_{\text{insert}} = 0.077$ m, compared to the investigated frequency range.

Four configurations have been designed to test different jet nozzle diameters and patterns. Table 5.1 lists the investigated configurations.

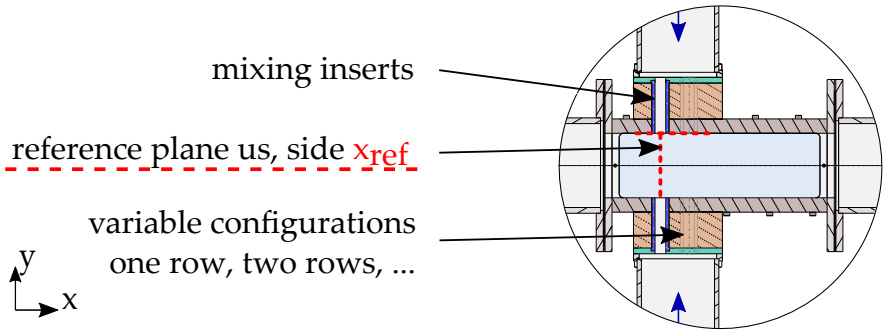

Figure 5.3: Detailed view of mixing air section and position of reference planes x_u and x_s.

Table 5.1: Characteristic parameters of the designed mixing air configurations.

Jet Parameter	Unit	Config. Ⓐ 1 row	Config. Ⓑ 1 row	Config. Ⓒ 2 rows	Config. Ⓓ 1row
$d_{\text{jet,eff,I}}$	mm	14.89	16.64	12.45	8.74
$d_{\text{jet,eff,I}}$	mm	–		10.00	–
$n_{\text{jet,I}}$	–	6			4
$n_{\text{jet,II}}$	–	–		4	–
J_{I}	–	23.97	17.94	26.46	194.94
J_{II}	–	–		10.89	–
s_{x}	mm	–		30	–

5.2 Acoustic and Thermal Design

The experimental setup comprises a series of ducts with varying inner diameters. In order to obtain a one-dimensional acoustic field along the axis of the ducts, it is necessary to suppress transverse modes. To achieve this, the diameter of the ducts must be smaller than the investigated wavelength. Higher order modes occur beyond specific cut-off frequencies f_{cut}, which depend on the acoustic mode and the duct geometry [83]. For cylindrical ducts, modes that are not entirely axial start propagating at frequencies above

$$f_{\text{cut,cyl,(1,0)}} = \frac{1.84}{\pi d} c \tag{5.1}$$

as a function of the duct diameter d and the speed of sound c. For rectangular ducts, f_{cut} is expressed as

$$f_{\text{cut,rec,(1,0)}} = \frac{c}{2} \sqrt{\left(\frac{m}{b}\right)^2 + \left(\frac{n}{h}\right)^2}, \tag{5.2}$$

Table 5.2: Cut-off frequencies for main ducts in RQL test rig.

	Transition duct (cyl)	Side duct (cyl)	End duct (rec)
$f_{\text{cut},(1,0)}$	3347 Hz	2156 Hz	3716 Hz

where $m = 1$, $n = 0$, $b = h = 0.09\,\text{m}$ represent the inner dimensions of the rectangular duct [49]. The critical cut-off frequencies for the various duct geometries of the test rig are summarized in Table 5.2, which were obtained at different temperatures in the corresponding duct. All frequencies exceed the operating range of excitation by a factor greater than 5. Therefore, radial and circumferential modes can be considered negligible, which is essential for interpreting the acoustic measurements and applying the multi-microphone method (MMM).

The length of the ducts used for wavefield reconstruction in the test rig is determined by the lowest frequency of the acoustic field. Based on previous experimental studies [54, 71, 83], assuming a similar speed of sound and scaling with the Helmholtz-number for the frequency range starting at $f = 60$ Hz, the optimal duct length for high-quality reconstruction is approximate $l_{\text{duct}} \approx 1.07\,\text{m}$. All major ducts in the RQL facility comply with this criterion.

The thermal design of the test rig played a crucial role in ensuring the re-ignition of the reactive hot gas in the secondary zone. The secondary zone inlet temperature of the reactive flow were determined based on a one-dimensional enthalpy balance for the primary zone and the transition duct. Impingement cooling was employed for the primary zone in the experimental setup to prevent overheating of the steel and quartz glass windows. In contrast, the transition duct utilized natural convection and radiation for cooling. In order to guarantee re-ignition in the secondary zone, the effects of chemical kinetics needed to be considered. A homogeneous constant pressure reactor (CPR) was integrated into the CANTERA software platform to calculate the re-ignition time

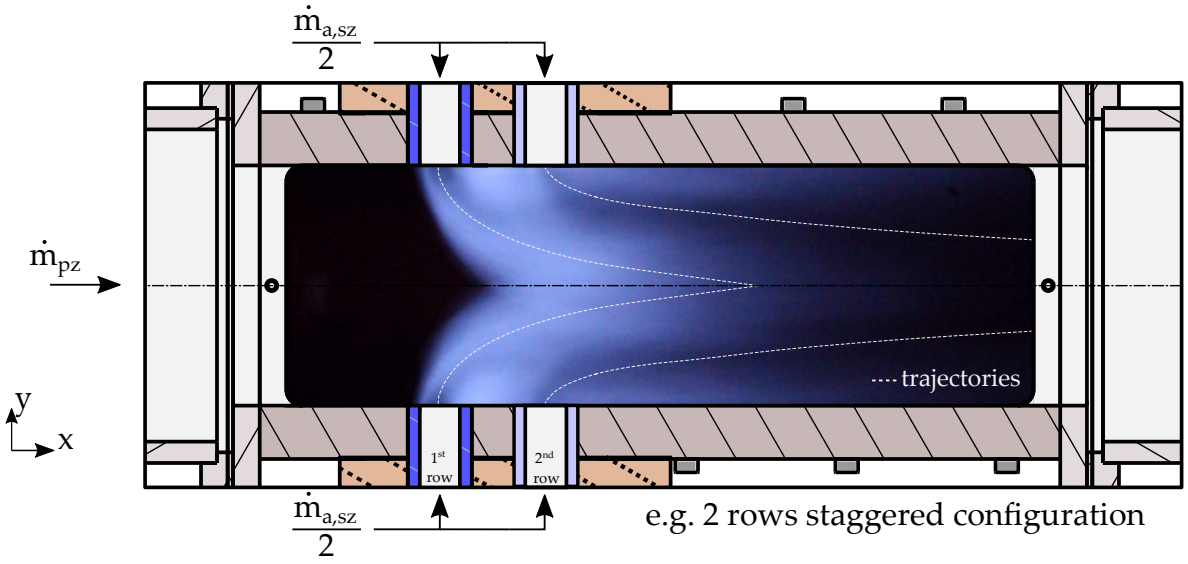

Figure 5.4: Image of the inverse diffusion flame in the lean secondary zone; dashed lines represent the calculated trajectories for rows one and two.

delay. This involved combining the exhaust gas constituents of the rich primary zone, at the transition duct's exit temperature, with the pre-heated air of the lean secondary zone. The reactor was propagated in time until a temperature rise to 50% of the maximum temperature in the secondary combustor was reached, leading to an ignition time delay of $t_{\text{ign}} \approx 0.145$ ms. Ignition in the experiment takes place in the mixing jet shear layer close to the stoichiometric mixture fraction. However, for the CPR approach, ignition is observed at leaner and colder mixtures as for the experiments. Thus, the CPR gives a more conservative result. This seemed to justify the assumption of immediate re-ignition in the lean burn-out zone despite the considerable heat loss upstream. Figure 5.4 shows an image of the secondary zone flame structure. In side view, the chemiluminescence of the first-row flames partly hides the second-row jets. The flames anchor immediately at the mixing jet nozzle, and combustion mainly occurs in the shear layers following the jet trajectory, resulting in overall lean inverse diffusion flames in the secondary zone.

6 Measurement Techniques and Data Processing

This chapter describes measurement techniques and methodologies used to investigate the lean secondary zone thermoacoustics in detail. A comprehensive investigation of the thermoacoustic cycle necessitates high spatio-temporal resolution of the acoustic quantities and the heat release. The acoustic pressure oscillations and the flame chemiluminescence, a measure of the flame heat release, are synchronously sampled. The main diagnostic equipment employed in this study includes dynamic pressure transducers, a photomultiplier tube (PMT), and an intensified high-speed CMOS camera. The plane wave decomposition technique is utilized to analyze the dynamic pressure and provides a basis for the multi-microphone method (MMM), which is used to determine acoustic scattering matrices (SM) and flame transfer functions (FTF) in the low-frequency domain. Optical measurement techniques are also introduced to capture the heat release distribution of the flame using time-resolved $OH^{\star}$-chemiluminescence (CL) with the PMT. In addition, an intensified high-speed CMOS camera is employed to acquire the flame shape, position, and intensity distribution based on $OH^{\star}$-CL images.

6.1 Pressure Transducers

Multiple piezoelectric pressure transducers (Type: PCB 106B) are used in the test rig transition and end duct, up and downstream of the secondary zone, and in the side ducts to fully identify the plane wave acoustic pressure field. Each duct has three piezoelectric pressure transducers, which are mounted in a water-cooled holder (Type: PCB 064B06) with a cavity working as a heat shield; both are shown on the right

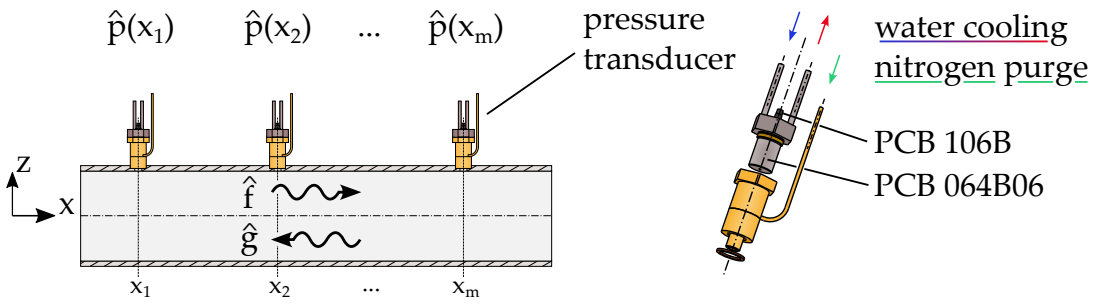

Figure 6.1: Left: Illustration of the plane wave decomposition; right: Sketch of the pressure transducer with water-cooled holder and the purging adapter made of brass.

in Fig. 6.1. The electronics integrated in the piezoelectric transducers has a great advantage over other standard systems. Signal strength is converted within the sensor housing, making further amplification units needless and improving signal robustness. Each water-cooled adapter is purged with nitrogen to prevent condensation on the sensor membrane. A total nitrogen mass flow of $\dot{m}_{N_2} = 0.2\,g/s$ is used for all pressure transducers. Sensor sensitivity ranges from $35 - 45$ mV/kPa. All dynamics pressure transducers are sampled synchronously with two National Instruments PCIe-4472 cards.

6.2 Plane Wave Decomposition

The spectral analysis returns a complex pressure amplitude for each frequency and dynamic pressure transducer. Assuming plane waves, the sound pressure measured by a pressure transducer is a superposition of two waves traveling in opposite directions with a certain frequency $f_n = \omega_n/2\pi$. This is expressed by Eq. 6.1 in terms of complex amplitudes of the Riemann invariants $\widehat{f}$ and $\widehat{g}$ represent the waves flowing in co-flow and counter-flow direction:

$$\widehat{p}(x,\omega) = \widehat{f}(\omega)e^{-ik^+x} + \widehat{g}(\omega)e^{ik^-x} \tag{6.1}$$

The acoustic pressure has been scaled by the characteristic impedance, $\bar{\rho}\bar{c}$ for ease of notation. The plane wave decomposition determines the complex amplitudes $\widehat{f}$ and $\widehat{g}$ from the knowledge of $\widehat{p}(x)$ at multiple axial positions, as illustrated on the left in Fig. 6.1. This yields the following linear system of equations:

$$\begin{aligned} \widehat{p}(x_1,\omega) &= \widehat{f}(\omega)e^{-ik^+x_1} + \widehat{g}(\omega)e^{ik^-x_1} \\ \widehat{p}(x_2,\omega) &= \widehat{f}(\omega)e^{-ik^+x_2} + \widehat{g}(\omega)e^{ik^-x_2} \\ &\vdots \\ \widehat{p}(x_\mathrm{m},\omega) &= \widehat{f}(\omega)e^{-ik^+x_\mathrm{m}} + \widehat{g}(\omega)e^{ik^-x_\mathrm{m}} \end{aligned} \tag{6.2}$$

Equation system 6.3 can be written in matrix form:

$$\underbrace{\begin{bmatrix} e^{-ik^+x_1} & e^{ik^-x_1} \\ e^{-ik^+x_2} & e^{ik^-x_2} \\ \vdots & \vdots \\ e^{-ik^+x_\mathrm{m}} & e^{ik^-x_\mathrm{m}} \end{bmatrix}}_{\mathbf{H}} \times \underbrace{\begin{bmatrix} \widehat{f}(\omega) \\ \widehat{g}(\omega) \end{bmatrix}}_{\mathbf{x}} = \underbrace{\begin{bmatrix} \widehat{p}\,(x_1,\omega) \\ \widehat{p}\,(x_2,\omega) \\ \vdots \\ \widehat{p}\,(x_\mathrm{m},\omega) \end{bmatrix}}_{\mathbf{b}} \tag{6.3}$$

Here $\mathbf{b}$ is represented by the Fourier transform $\widehat{p}(x,\omega)$ of the acoustic pressure signal $p^{'}(x,t)$ acquired at a specific location x_m and evaluated at the discrete forcing frequency $f_\mathrm{n} = \omega_\mathrm{n}/2\pi$. The size of the system matrices is given by the number of unknowns in vector $\mathbf{x}$ and the number of available observation data 'm'. The two $(n = 2)$ unknowns are $\widehat{f}$ and $\widehat{g}$, and 'm' represents the number of pressure transducers in each duct at distinct axial positions.

With at least two linearly independent equations, Eq. 6.3 can be solved. If the number of equations and unknowns are equal, then the method is commonly referred to as the two-microphone method [84, 85]. With the number of equations greater than unknowns, the method is commonly referred to as the multi-microphone method (MMM) [51, 62, 80]. Using more than the desired minimum of two equations yields an over-

determined system of equations and results in an optimization problem. Equation 6.3 is reformulated in a least-square sense, giving the best fit to the solution [86, 87]:

$$\mathbf{x} = \mathbf{H}^{\dagger}\mathbf{b} \tag{6.4}$$

The matrix $\mathbf{H}^{\dagger}$ is the Moore-Penrose pseudoinverse of matrix $\mathbf{H}$ which is defined by

$$\mathbf{H}^{\dagger} = (\mathbf{H}^{\top}\mathbf{H})^{-1}\mathbf{H}^{\top} \quad . \tag{6.5}$$

The superscripts '-1' and 'T' denote the inverse and the conjugate transpose of matrix $\mathbf{H}$, respectively. An estimated error of the fitted solution values of the Riemann invariants in matrix $\mathbf{x}$ can be calculated from

$$\delta = \frac{\left\| \left(\mathbf{I}^{n} - \mathbf{H}\mathbf{H}^{\dagger}\right) \mathbf{b} \right\|_2}{\|\mathbf{b}\|_2} \quad , \tag{6.6}$$

where $\mathbf{I}^{n}$ denotes the identity matrix of size $n \times n$ with n as the number of pressure transducers, the vector $\mathbf{b}$ contains the complex amplitudes and $||\dots||_2$ is the l^2-norm. The smaller the calculated error δ, the better the agreement between the measured pressures and the calculated Riemann invariants. Values around 1% to 4% are typical for a good measurement.

Prior to conducting experiments, microphones are calibrated using a reference pressure transducer sensor to reduce measurement errors. This approach minimizes the relative amplitude and phase discrepancies among the pressure transducers. Further information regarding the calibration procedure can be found in [52] and [88].

Besides noise contributions, another possible source of error could be the speed of sound $c = \sqrt{\gamma R T}$, e.g., the temperature T, which is taken to calculate the wave number k. Errors might be introduced here if the constant axial temperature profile assumption is invalid. For those cases, solutions for linear, exponential, or polynomial mean temperature

profiles could be applied [89–91]. No further correction was made in this thesis, and a constant profile was assumed.

6.3 Determination of the Scattering Matrices

Acoustical characterization of a burner, duct, or junction requires knowledge of the outgoing response to given ingoing acoustic perturbations and vice versa. These elements can be considered as linear time-invariant multi- or N-port elements, where N denotes the total number of ports of the element [67, 92]. In linear acoustics, transmission and reflection of plane harmonic waves in such N-port elements at frequencies below the first cut-off frequency are described by a matrix. The properties of the N-port are independent of the rest of the system elements, and networks of multiple N-port elements can be set up for robust calculations [93].

A model for N-port elements without sources can be expressed as $\mathbf{y} = \mathbf{A}\mathbf{x}$, where $\mathbf{y}$ $(N \times 1)$ is the output state vector, $\mathbf{x}$ $(N \times 1)$ is the input state vector, and $\mathbf{A}$ $(N \times N)$ is the matrix containing the element properties. The multi-port can be modified to include source terms by adding a source vector $\mathbf{y}^s$, representing active parts of the multi-port [94]. This approach is often used in aero-acoustics, where amplification and attenuation between the acoustics and the hydrodynamic field are considered.

Experimental determination of multi-ports can be based on two methods, the N-load method and the N-source method. The N-load method is only applicable when an acoustic source exists and the generated pressure amplitudes are very high ($>$ 130 dB in air) [94]. The latter, the N-source method, is applied in this work and has been used extensively in thermoacoustic research. The determination of scattering matrices is based, like the MMM, on wave field decomposition.

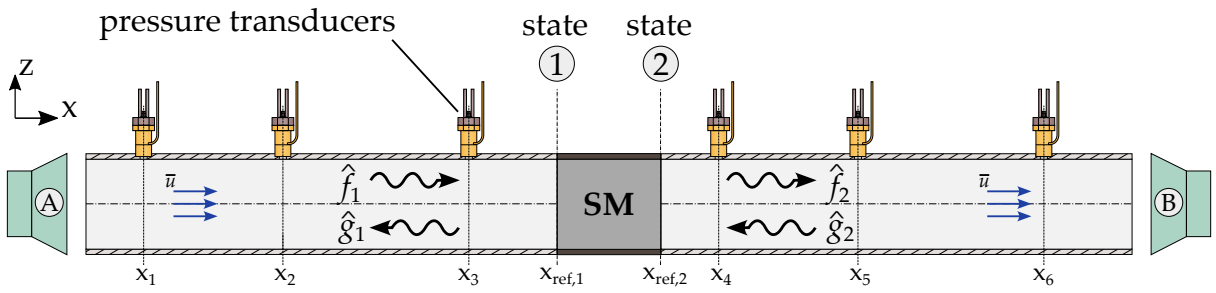

Figure 6.2: Schematic of the 2-port setup to determine scattering matrices based on the MMM and wave decomposition.

6.3.1 Scattering Matrices of 2-port Elements

Acoustically coupled elements with one input and output can be best described using a 2-port model, where $N = 2$. Various formulations of the 2-port model exist, and each can be derived from a linear combination. In thermoacoustics, it is convenient to choose the Riemann invariant variables $\widehat{f}$ and $\widehat{g}$ as state variables, where the matrix $\mathbf{A}$ is referred to as the scattering matrix **SM**. A schematic of a generic setup to determine acoustic scattering matrices is presented in Fig. 6.2. The frequency domain formulation of the 2-port model can be expressed as follows:

$$\underbrace{\begin{bmatrix} \widehat{g}_1(\omega) \\ \widehat{f}_2(\omega) \end{bmatrix}}_{\mathbf{y}} = \underbrace{\begin{bmatrix} R_1 & T_{21} \\ T_{12} & R_2 \end{bmatrix}}_{\mathbf{SM}^{fg}_{2x2}} \underbrace{\begin{bmatrix} \widehat{f}_1(\omega) \\ \widehat{g}_2(\omega) \end{bmatrix}}_{\mathbf{x}} \tag{6.7}$$

The matrix connects the Riemann invariants at the two sides of the 2-port denoted by ① and ②, respectively. The unknown reflection R and transmission T coefficients of the incoming waves can be determined using four equations, provided that the vectors $\mathbf{y}$ and $\mathbf{x}$ are known. Two of these equations can be obtained from an acoustic field measurement on either side of the 2-port using the wave-decomposition method discussed earlier. The other two equations can be obtained by modifying the acoustic field and performing a second measurement, which can be

achieved by altering the system's acoustic load or by changing the excitation location [50]. In this study, the latter approach is used, as shown in Fig. 6.2 with the two loudspeakers Ⓐ and Ⓑ, creating independent load cases for the 2-port. The solution is obtained by solving the following linear equation system:

$$\underbrace{\begin{bmatrix} R_1 & T_{21} \\ T_{12} & R_2 \end{bmatrix}}_{\mathbf{SM}_{2x2}^{fg}} = \underbrace{\begin{bmatrix} \widehat{g}_1^A(\omega) & \widehat{g}_1^B(\omega) \\ \widehat{f}_2^A(\omega) & \widehat{f}_2^B(\omega) \end{bmatrix}}_{\mathbf{y}} \underbrace{\begin{bmatrix} \widehat{f}_1^A(\omega) & \widehat{f}_1^B(\omega) \\ \widehat{g}_2^A(\omega) & \widehat{g}_2^B(\omega) \end{bmatrix}^{-1}}_{\mathbf{x}^{-1}} \tag{6.8}$$

The subscripts for the Riemann invariants $(\,)_{1,2}$ refer to the axial reference plane of the corresponding states ① and ② and were determined using the pressure transducers upstream and downstream of the reference planes. The superscripts $(\,)^{A,B}$ represent the two excitation positions for the two-source method. The presented 2-port technique is applied to determine the lean secondary zone characteristics in the stiff mixing air jets configuration, which is presented in Chapter 7.

6.3.2 Scattering Matrices of 3-port Elements

This section discusses the determination of scattering matrices for elements with $N = 3$ ports, as presented by Karlsson and Åbom [68] and Holmberg et al. [69]. A 3×3 scattering matrix (**SM**) is used to represent the reflection and transmission coefficients R and T of the system for the selected state variables. Figure 6.3 shows a schematic of a generic setup to determine the scattering matrix for a 3-port system by adding a third branch ③. Similar to the 2-port element, the 3-port can be written in the

frequency domain as:

$$\begin{bmatrix} \widehat{g}_1(\omega) \\ \widehat{g}_2(\omega) \\ \widehat{f}_3(\omega) \end{bmatrix} = \underbrace{\begin{bmatrix} R_1 & T_{21} & T_{31} \\ T_{12} & R_2 & T_{32} \\ T_{13} & T_{23} & R_3 \end{bmatrix}}_{\mathbf{SM}^{\mathrm{fg}}_{3\mathrm{x}3}} \begin{bmatrix} \widehat{f}_1(\omega) \\ \widehat{f}_2(\omega) \\ \widehat{g}_3(\omega) \end{bmatrix} \tag{6.9}$$

With the addition of one port, the matrix now contains nine unknown reflection and transmission coefficients, which describe the system behavior. To solve for these coefficients, three excitation cases can be realized by adding a third loudspeaker C. This results in a system of nine

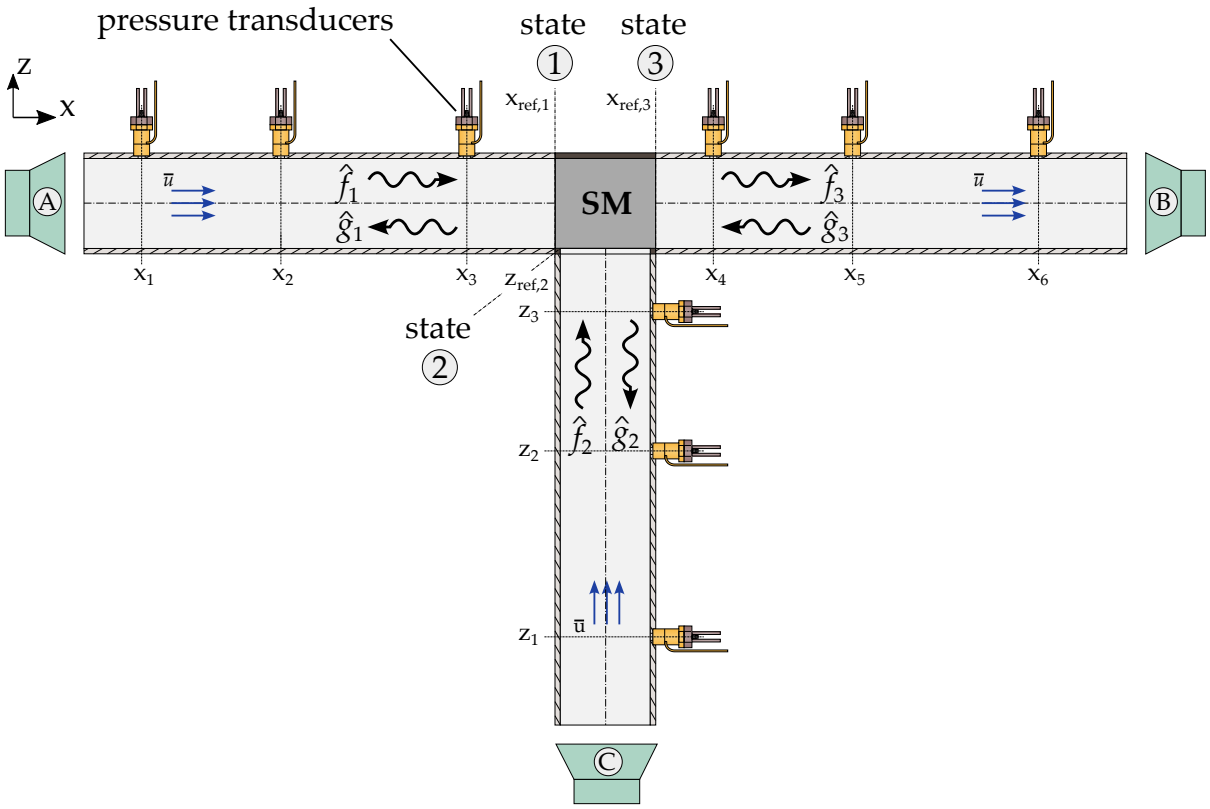

Figure 6.3: Schematic of the 3-port setup to determine scattering matrices based on the MMM and wave decomposition.

linear independent equations. The solution is given by the same matrix multiplication as in Eq. 6.8:

$$\begin{bmatrix} R_1 & T_{21} & T_{31} \\ T_{12} & R_2 & T_{32} \\ T_{13} & T_{23} & R_3 \end{bmatrix} = \begin{bmatrix} \widehat{g}_1^A(\omega) & \widehat{g}_1^B(\omega) \\ \widehat{g}_2^A(\omega) & \widehat{g}_2^B(\omega) \\ \widehat{f}_3^A(\omega) & \widehat{f}_3^B(\omega) \end{bmatrix} \begin{bmatrix} \widehat{g}_1^C(\omega) \\ \widehat{g}_2^C(\omega) \\ \widehat{f}_3^C(\omega) \end{bmatrix} \begin{bmatrix} \widehat{f}_1^A(\omega) & \widehat{f}_1^B(\omega) & \widehat{f}_1^C(\omega) \\ \widehat{f}_2^A(\omega) & \widehat{f}_2^B(\omega) & \widehat{f}_2^C(\omega) \\ \widehat{g}_3^A(\omega) & \widehat{g}_3^B(\omega) & \widehat{g}_3^C(\omega) \end{bmatrix}^{-1} \tag{6.10}$$

The presented states ①, ② and ③ in Fig. 6.3 represent the states upstream coming from the primary zone, the side mixing air jets and the downstream state, denoted by the subscripts $(\,)_{u,s,d}$.

6.4 Measurement of 2-port Flame Transfer Functions Based on the Rankine-Hugoniot Relations

Utilizing the relationship between flame transfer matrix (**FTM**) and flame transfer function FTF given by Eq. 2.73, it is possible to obtain the FTF from pure acoustic measurements based on the MMM. It is experimentally impossible to determine the flame transfer matrix separately from the burner transfer matrix since measurements involving flames always include the burner transfer matrix. However, this contribution can be eliminated in the evaluation process. The measurement procedure involves acquiring two transfer matrices for burners with and without flames, with the procedure presented in Section 6.3.

The scattering matrices in fg-notation are converted to transfer matrices in pu-notation using Eqs. 2.38 and 2.38. Despite the presence of the flame, the burner transfer matrix is assumed to remain unchanged in

the reacting case with flame downstream of the burner. The **FTM** can be determined using the matrix operation

$$\mathbf{FTM} = \mathbf{BFTM} \cdot \mathbf{BTM}^{-1}, \tag{6.11}$$

where **BFTM** and **BTM** represent the matrices from measurements with combustion (burner+flame) and without combustion (burner only). Several previous works have utilized and justified this assumption [52, 54, 66, 95]. With the following relationship the FTF is determined:

$$FTF(\omega) = \frac{\mathbf{FTM}_{22}(\omega) - 1}{\frac{T_{\text{hot}}}{T_{\text{cold}}} - 1} \tag{6.12}$$

Here, $\mathbf{FTM}_{22}$ represents the lower right 22-Element of the flame transfer matrix, T_{hot} is the flame temperature and T_{cold} is the reactant and starting temperature of combustion. The temperature description and the measurement locations are presented in Section 6.6.

6.5 Measurement of Flame Transfer Functions Based on OH* Chemiluminescence

The measurement of spontaneous emission of electromagnetic radiation from excited species generated during chemical reactions - so-called chemiluminescence (CL) - is a common measurement technique widely used to evaluate flame properties. The main light emitters in hydrocarbon flames suitable for monitoring the flame are $OH^\star$, $CH^\star$, $C_2^\star$ and $CO_2^\star$ ($(\ )^\star$ denoting the excited state) with peaks at 309, 431, 516 and 300-600 nm, respectively. The relationship between light emission and flame properties has been studied multiple times [96–100]. $OH^\star$ CL has become widely used for heat release in premixed flames and has been extended to non-premixed combustors by Morrell et al. [101]. Most approaches relying on CL are prone to regions of high strain and strong equivalence ratio fluctuations. The latter provides an additional influence to the heat release, and thus the FTF often cannot be calcu-

lated correctly from the OH*-radical CL [102]. On the other hand, Lauer and Sattelmayer [96] proved that CL can capture the heat release of turbulent flames with a classic burner−flame setup. Considering the highly reactive nature of the hot gases from the primary zone, it can be expected that the secondary flame will react in the flamelet regime with a narrow stoichiometry band around the most reactive mixture fraction. Thus, the CL of the flame would, similar to premixed combustion, be a function of the flamelet density and could serve as a measure of the heat release.

The OH* CL is monitored with a photomultiplier tube (PMT). As described in the experimental setup in Chapter 5, the OH* CL PMT is mounted above the test rig. It simultaneously captures the flame CL during the forcing cycle with the pressure transducers. A narrow bandpass filter with a wavelength of 308nm full width at half maximum of 10nm is used to detect emissions in the OH* band.

Flame transfer functions are a common way to describe the dynamic response of the flame to acoustic perturbations. FTFs are determined experimentally using OH*-CL and the PMT to represent the flame dynamics in the lean secondary zone. The signal from the PMT $I(t)$ can be related to the heat release $\dot{Q}$ as $I \propto \dot{Q}$. For well-known 2-port setups the FTF is often referred to only one reference velocity fluctuation leading to the following representation of the FTF:

$$\frac{\dot{Q}'(\omega)}{\bar{\dot{Q}}(\omega)} = \frac{I'_{\mathrm{OH}^*}(\omega)}{\bar{I}_{\mathrm{OH}^*}(\omega)} = FTF_{\mathrm{u,PMT}}(\omega)\frac{u'_{\mathrm{u}}(\omega)}{\bar{u}_{\mathrm{u}}} \tag{6.13}$$

This formulation has widely been used in experimental investigations, and the gained OH* CL FTF is often compared to the pure acoustic Rankine-Hugoniot FTF as derived in the previous Section 6.4 [54, 66].

This approach is now applied to the lean secondary zone with two velocity fluctuations. As for the pure acoustic approach (see Chapter 3), it is assumed that the total intensity fluctuation recorded with the PMT

is a superposition of two independent contributions. Each of them is a function of the corresponding velocity fluctuations upstream and in the mixing ports and can be evaluated as follows:

$$\frac{\dot{Q}'(\omega)}{\bar{\dot{Q}}(\omega)} = \frac{I'_{\mathrm{OH}^\star}(\omega)}{\bar{I}_{\mathrm{OH}^\star}(\omega)} = FTF_{\mathrm{u,PMT}}(\omega)\frac{u'_{\mathrm{u}}(\omega)}{\bar{u}_{\mathrm{u}}} + FTF_{\mathrm{s,PMT}}(\omega)\frac{u'_{\mathrm{s}}(\omega)}{\bar{u}_{s}} \quad (6.14)$$

Here $I'_{\mathrm{OH}^\star}/\bar{I}_{\mathrm{OH}^\star}$ represents the ratio between the measured fluctuations of the $\mathrm{OH}^\star$ CL intensity, normalized by the mean value. The desired velocity fluctuations at the reference position upstream u'_{u} and in the mixing air jets u'_{s} can be obtained from dynamic pressure measurements applying the MMM. The mean value of the velocities $\bar{u}_{\mathrm{u}}$ and $\bar{u}_{\mathrm{s}}$ are calculated from the mass flow through the combustor area and the mixing air jets.

Both FTFs found with the $\mathrm{OH}^\star$ CL method are compared with the ones measured with the pure acoustic MISO approach (subscript $(\,)_{\ldots,\mathrm{M}}$) in the results chapter.

6.6 Operating Modes and Flame Temperatures

Determination of the flame dynamics with the MISO approach and the classical 2-port MMM technique requires first characterizing the 'cold' non-reacting flow and then the 'hot' reacting flow case.

Typically, 'cold' measurements (**BTM** / **BSM**) are performed with preheated air flowing through the burner. In the presented case, the inlet temperatures at the secondary zone from upstream are too high for using an air preheater. As a result, the 'cold' case is measured with the same secondary air settings as the 'hot' case but with the primary zone operating at lean conditions ($\phi_{\mathrm{pz}} < 1$) and the same hot gas temperature T_{u}^{BSM} as the reacting case. The air mass flow rates are kept the same so that only pure mixing occurs in the lean secondary zone.

For the 'hot' case (**BFSM** / **BFTM**), with flame in the secondary zone, the rich mixture ($\phi_{pz} > 1$) from the primary zone forms an inverse diffusion flame in the shear layers of the secondary jets. Matching inlet conditions for both measurements are ensured by adjusting the fuel mass flow rate in the 'cold' case so that $T_u^{BSM} = T_u^{BFSM}$ (measured at the inlet of the secondary zone).

For the determination of the **BSM**'s nine matrix coefficients (R_n, T_{nm}) the N-source technique is employed, which involves forcing from upstream, side and downstream direction. The **BSM** is illustrated by the left acoustic 3-port element in the lower part of Fig. 3.1 (dashed blue line). The same technique is applied to determine the 'hot' **BFSM**. The **BFSM** includes the flame behavior and represents the total MISO network system, and is also illustrated in the lower part of Fig. 3.1 (dashed red line).

The flame is considered acoustically compact such that the Rankine-Hugoniot (RH) relations between the two temperatures T_{cold} and T_{hot} can be invoked [95]. Both temperatures are measured using Type-N thermocouples downstream of the secondary zone and the measurement position is depicted in Fig. 5.1. The fuel and oxidizer enter the secondary zone separately. Mixing then takes place by convection and diffusion. Combustion occurs in a thin layer in the vicinity of the mixture surface. Here, the local mixture fraction gradient is sufficiently high; thus, this surface is defined by a most reactive mixture fraction Z_{mr} and a corresponding mixture temperature $T_{mr,mix}$. Measured in the 'cold' (**BSM**) case, T_{cold} represents the virtual mixture temperature of the primary and secondary flows before the heat addition from the inverse diffusion flame. T_{hot} is measured in the **BFSM** case with flame and is the flame temperature. Both temperatures T_{cold}, T_{hot} are used for the classical 2-port RH approach. With the additional predetermined 'cold' matrix coefficients and the second 'hot' measurement the MISO network system can be solved for the two FTFs.

Table 6.1: Operating range for the lean secondary zone; OP2* is considered as baseline operating point; the configuration parameters are listed in Table 5.1.

Flow Para.	Unit	Operating Point (OP)											
		1	2*	3	4	5	2*	6	7	2*	8	9	10
T_{pre}	K	473											
$\dot{m}_{\text{fuel}}$	g/s	1.07				1.14	1.07	1.01	0.95	1.07			
$\dot{m}_{\text{air,pz}}$	g/s	13.45	14.35	15.25	16.15	14.35							
$\dot{m}_{\text{air,sz}}$	g/s	15.18	16.19	17.20	18.22	16.19							
$\dot{m}_{\text{air,tot}}$	g/s	28.63	30.54	32.45	34.37	30.54							
ϕ_{pz}	–	1.33	1.25	1.18	1.11	1.33	1.25	1.18	1.11	1.25			
ϕ_{tot}	–	0.63	0.59	0.55	0.52	0.63	0.59	0.55	0.52	0.59			
Configuration		Ⓐ				Ⓐ				Ⓐ	Ⓑ	Ⓒ	Ⓓ

In the experimental investigation of the combustion process, several operating points (OPs) were considered, summarized in Table 6.1. OP2* is considered the baseline design operating point and is part of all three major operating ranges.

The fuel flow rate was fixed for operating points OP1 to OP4, ensuring constant thermal power in the first stage. The primary and secondary air flow rates are increased to reduce the primary zone ϕ_{pz} and total equivalence ratio ϕ_{tot}. This leads to a change in momentum flux ratio J among these four OPs. Concerning the heat release in the secondary zone, OP1 is the most and OP4 the least reactive OP.

For OP5 to OP7, both air mass flow rates were fixed at the values of OP2*, while the fuel mass flow rate was varied to create an operating range with constant exit velocities in the burner and the secondary mixing air jets. This ensured a constant momentum flux ratio J and

velocity ratio R in the secondary zone and preserved the JIC mixing field characteristics, with OP5 being the most and OP7 the least reactive OP in this group.

Finally, OP8 to OP10 involved changes in the mixing air jet configuration to investigate different total cross-sectional areas and patterns of the mixing air jets. This permitted a more detailed analysis of the mixing and coupling processes in the secondary zone.

7 Flame Response to Primary Zone Velocity Fluctuations

In Chapter 3, the MISO approach was introduced to describe the dynamic behavior of the lean secondary zone treated as a 3-port network system. At this point, asymptotic cases can be identified in which the 3-port system degenerates into a 2-port system and can readily be analyzed using the established MMM 2-port technique presented in Section 6.4. One of these asymptotic cases is generated by acoustically stiff secondary mixing air jets. The large distance between both combustion zones ensures a homogeneous temperature and velocity profile at the entrance of the secondary zone. Thereby, no other than velocity fluctuations are taken into account in describing the flame dynamic heat release. The flame in the lean secondary zone is expected only to react to the velocity fluctuations coming from the end of the primary zone. The established technique will also verify the generalized acoustic 3-port MISO approach, and the procedure is applied in Chapter 8 for multiple operating points. Operating points OP1 - 4 were evaluated to verify the asymptotic case findings. The setup and the procedure is explained in the following, and the resulting FTFs are discussed.

7.1 Acoustically Stiff Mixing Air Jets

In order to reduce the acoustic 3-port system to an acoustic 2-port system, the acoustic fluctuations of the mixing air jets must be suppressed. This was achieved using choked orifices in place of open insert holders at the entrance of the inserts as illustrated in Fig. 7.1 and tested in the simplified setup shown in Fig. 7.2. Figure 7.3 shows the

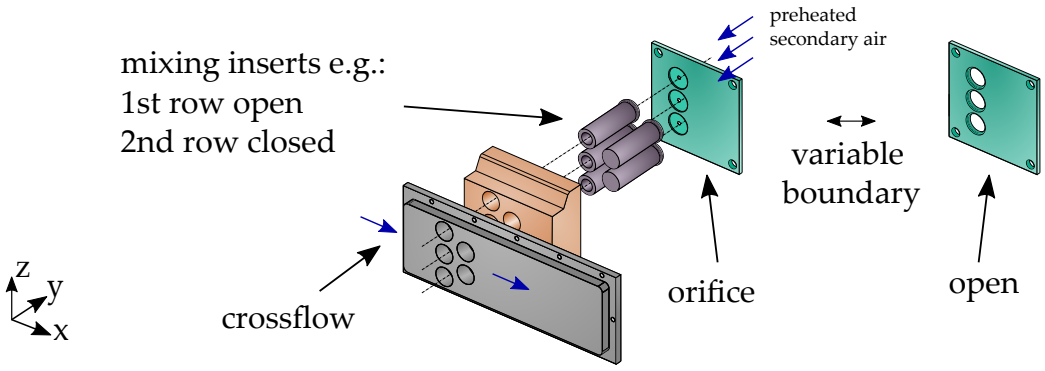

Figure 7.1: Mixing air section setup with view of mixing inserts and variable boundary - open and orifice.

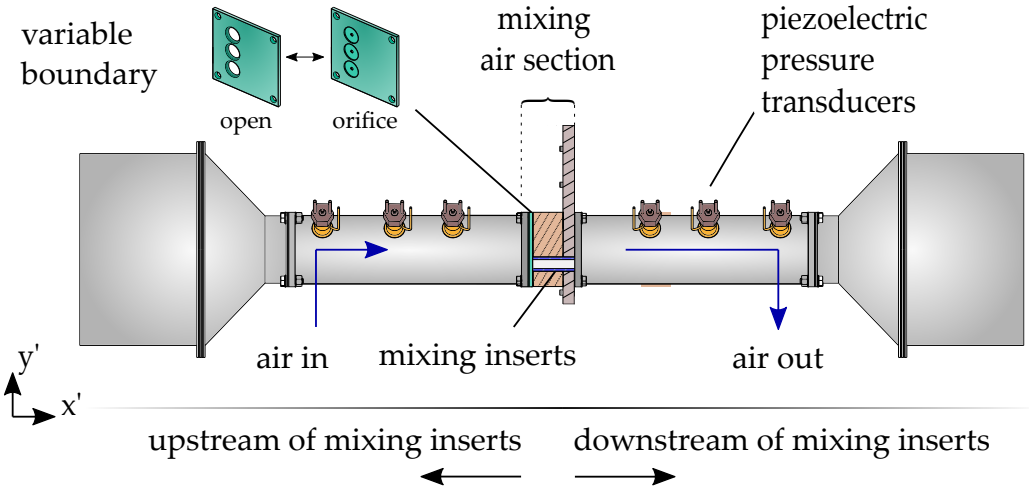

Figure 7.2: Simplified test section for characterization of mixing air section with different boundaries.

reflection coefficient of the downstream side of the inserts measured for the open and choked orifice configurations. It should be noted that no notable flame surface modification occurred despite changing the acoustic boundary condition. The open insert configuration, marked with circle symbols, results in the reflection coefficient R with a local

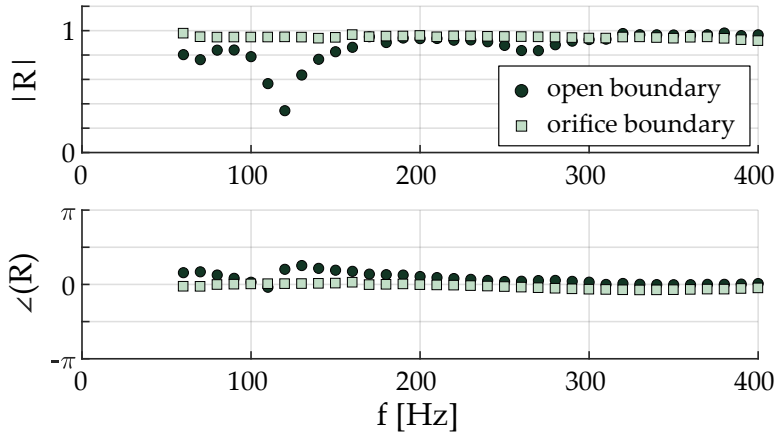

Figure 7.3: Reflection coefficient for different boundary conditions determined at the simplified test section; reference position inside the mixing jet nozzles.

minimum at $f = 120\,\mathrm{Hz}$ with $|R| = 0.34$. Subsequently, the reflection coefficient increases towards higher frequencies and approaches one. In contrast, using choked orifices as the boundary results in a reflection coefficient of approximately one for the entire frequency range, which is indicated by square symbols. Based on these findings, the velocity fluctuations in the mixing air jets of the test rig can be assumed to be nearly zero $u'_\mathrm{s} = 0$. Consequently, the acoustic topology of the test rig can be simplified from a 3-port to a 2-port system.

7.2 Transfer Behavior with Stiff Mixing Air Jets

In the following, the location of the two ports of the transfer matrices also referred to as reference planes, are defined at the same position $x_\mathrm{u} = x_\mathrm{d}$. The reference plane is the axial location of the cross-section through the secondary air jets and is marked in Fig. 5.3. Based on the operating point OP2* the transfer behavior will be evaluated. An illustrative example of a measured **BTM** is shown in Fig. 7.4 on the left.

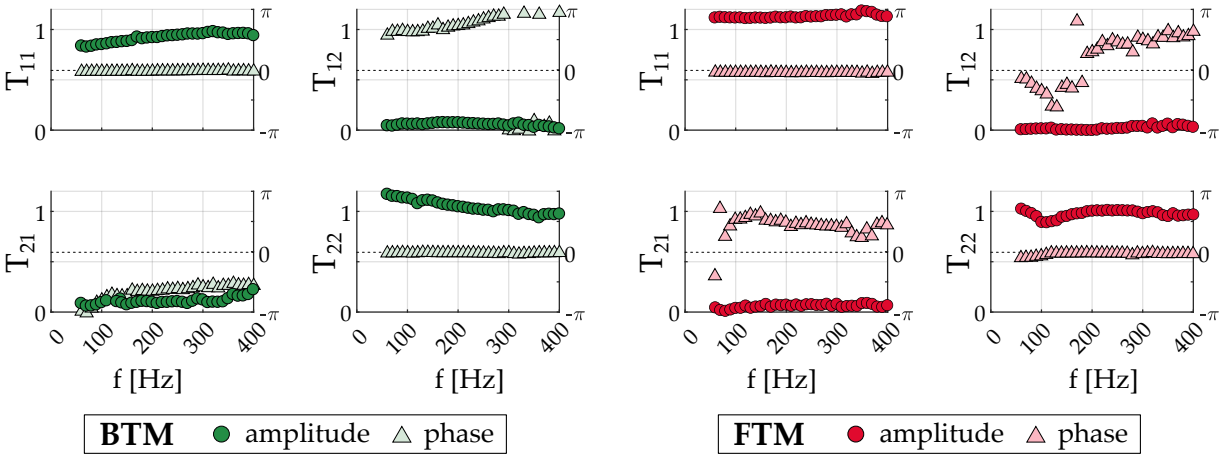

Figure 7.4: Left: burner transfer matrix of OP2*; right: flame transfer matrix of OP2*, calculated from **BTM** and **BFTM** measurements with normalized pressure $p'/\rho c$ and velocity u'.

The secondary zone is approximated by a straight duct with a small infinitesimal length, implying that an analytical transfer matrix in the form of Eq. 7.1 is expected:

$$\mathbf{BTM} = \lim_{L\to 0} \frac{1}{2} \begin{pmatrix} e^{-ik^+L} + e^{-ik^-L} & e^{-ik^+L} - e^{-ik^-L} \\ e^{-ik^+L} - e^{-ik^-L} & e^{-ik^+L} + e^{-ik^-L} \end{pmatrix} = \begin{pmatrix} 1 & 0 \\ 0 & 1 \end{pmatrix} \tag{7.1}$$

The element T_{11} relates the pressure upstream and downstream of the reference position, and its absolute value is close to unity. The phase matches the expected value of zero. The element T_{12} represents the influence of the upstream velocity on the downstream pressure and can be interpreted as a pressure loss term. The element T_{21} relates the upstream pressure to the downstream velocity and is expected to be small. The phase deviations have a negligible impact on the response, given the small magnitude of the transfer coefficient. The element T_{22} connects the acoustic velocity upstream and downstream and has a value of approximately one due to the continuity equation for compact elements. The **BTM** results agree well with the analytical model, and changes in operating conditions do not affect any elements, resulting in similar **BTM**s. The burner-flame transfer matrix is measured subsequently, and the

flame transfer matrix (**FTM**) is calculated using Eq. 6.11. The resulting **FTM** is shown on the right in Fig. 7.4. The element T_{11} has an almost constant absolute value close to the ratio of the characteristic impedance upstream $(\bar{\rho}c)_\mathrm{u}$ and downstream $(\bar{\rho}c)_\mathrm{d}$ of the flame, with a zero phase lag. The elements T_{12} and T_{21} have small amplitudes compared to the other elements, making their phases unimportant. The element T_{22} correlates with the fluid expansion due to the unsteady heat release rate and is highly dependent on the flame. Similar **FTM** results are obtained for all other operating conditions.

7.3 Flame Response with Varying Momentum Flux Ratio and Stiff Mixing Air Jets

With the application of the Rankine-Hugoniot relations from Eq. 6.12, the FTF_RH were calculated from the pure acoustic measurements. The hybrid FTF_PMT gained from optical OH* PMT measurements will be compared with the FTF_RH. For the hybrid FTF_PMT, the flame was acoustically excited from upstream. The velocity fluctuations u'_u were calculated using the MMM in the transition duct. To ensure that the flame response is in the linear regime, the forcing amplitude for all measurements was set to a maximum of $10 - 15\%$ in terms of the normalized

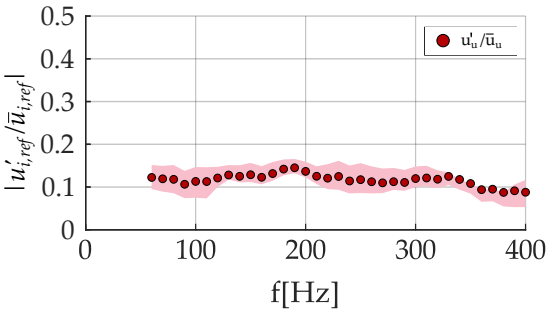

Figure 7.5: Velocity fluctuations in red markers at the reference position upstream with the standard deviation as shaded light red surface for the operating range OP1 - 4.

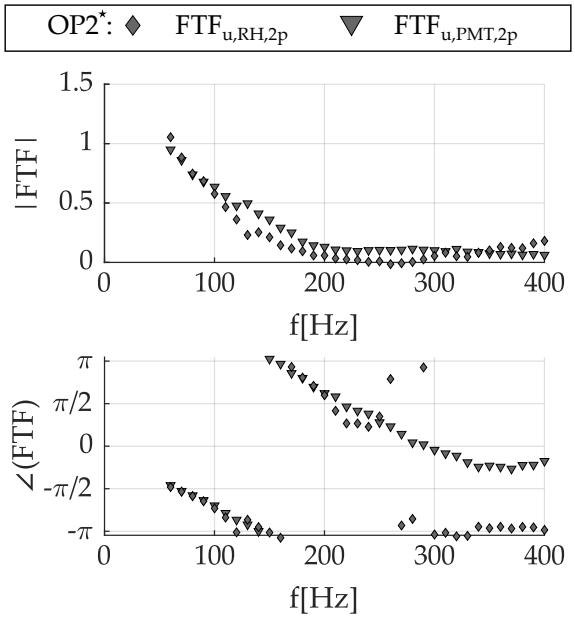

Figure 7.6: Flame transfer function of OP2*, pure acoustic FTF_{RH} in dark gray dots, compared with the hybrid FTF_{PMT} in dark gray triangles; top: amplitude of the FTFs; bottom: phase angle of the FTFs.

velocity fluctuations as shown in Fig. 7.5. The shaded zone in light red shows the standard deviation for all operation points.

The FTF results of OP2* are presented in Fig. 7.6. The absolute value of $FTF_{\mathrm{RH,OP2}^\star}$ shows a decreasing trend from $|FTF_{\mathrm{RH,OP2}^\star}| \approx 1$ at $f = 60\,\mathrm{Hz}$ to very low values of $|FTF_{\mathrm{RH,OP2}^\star}| \approx 0.14$ for frequencies greater than $f = 200\,\mathrm{Hz}$. The phase starts at $\angle FTF_{\mathrm{RH,OP2}^\star} \approx -\pi/2$ and exhibits a constant falling trend towards $f = 250\,\mathrm{Hz}$. The phase scattering of $\angle FTF_{\mathrm{RH,OP2}^\star}$ at higher frequencies can be attributed to the similarity of the underlying **BFTM** and **BTM** data and the low deviation of the corresponding T_{22}-elements. These low values result from small changes between the measurements with and without flame at higher frequencies. The linearly falling phase indicates a constant convective time delay between the velocity fluctuations in the reference plane and the heat release in the inverse diffusion flame. At low frequencies ($f \to 0$),

the phase becomes $\angle FTF_{\mathrm{RH,OP2^\star}} \approx 0$ similar to technically premixed flames with choked fuel feed [54,73]. The amplitude can be extrapolated to $|FTF_{\mathrm{RH,OP2^\star}}| \approx 1.35$ at $f = 0\,\mathrm{Hz}$, whereas a more quasi-stationary thermal power modulation at low frequencies would be expected.

In addition, $FTF_{\mathrm{RH,OP2^\star}}$ is compared to results of $FTF_{\mathrm{PMT,OP2^\star}}$ measured with the PMT. The amplitude and phase response of the PMT measurements show a great agreement with the RH FTFs. The PMT phase $\angle FTF_{\mathrm{PMT,OP2^\star}}$ seems more robust for higher frequencies. Since the $FTF_{\mathrm{PMT,OP2^\star}}$ relies only on the hot measurement data, it exhibits a continuous falling phase up to $f = 400\,\mathrm{Hz}$.

Figure 7.7 shows FTFs measured with the pure acoustic RH and the hybrid PMT method for the most reactive point OP1 to the least reactive point OP4. For the latter, the highest deviation in amplitude is observed between $|FTF_{\mathrm{RH,OP4}}|$ and $|FTF_{\mathrm{PMT,OP4}}|$ in the frequency range of $f = 60 - 200\,\mathrm{Hz}$. For the phase, $\angle FTF_{\mathrm{RH,OP4}}$ starts with high scattering from $f = 150\,\mathrm{Hz}$ on where $\angle FTF_{\mathrm{PMT,OP4}}$ still shows a linear trend. With reference to OP4, only a small amount of heat is released in the secondary zone resulting in a very small temperature increase due to combustion. These conditions are unfavorable for the **BFTM** and **BTM** measurements, leading to high scattering and uncertainty in the $FTF_{\mathrm{RH,OP4}}$ calculation. Conversely, for the most reactive point OP1, both FTFs fall on top of each other till the phase of $\angle FTF_{\mathrm{RH,OP1}}$ starts to deviate as does $\angle FTF_{\mathrm{RH,OP2^\star}}$ for frequencies higher $f = 200\,\mathrm{Hz}$, again due to vanishing amplitude.

In comparing the phases of OP1 and OP4, a steeper decline is observed for the more reactive OP1, whereas a flatter decline is seen for OP4. Specifically, the radially inward entrainment of ambient fluid is linked to the radially outward transport of jet fluid in the shear layer by shear layer turbulence. Once the stoichiometric amount of air for the primary mass flow rate $l_{\mathrm{min,p}}\dot{m}_{\mathrm{pr}}$ is entrained, the flame length L_{F} is reached. Consequently, the flame length varies with a larger

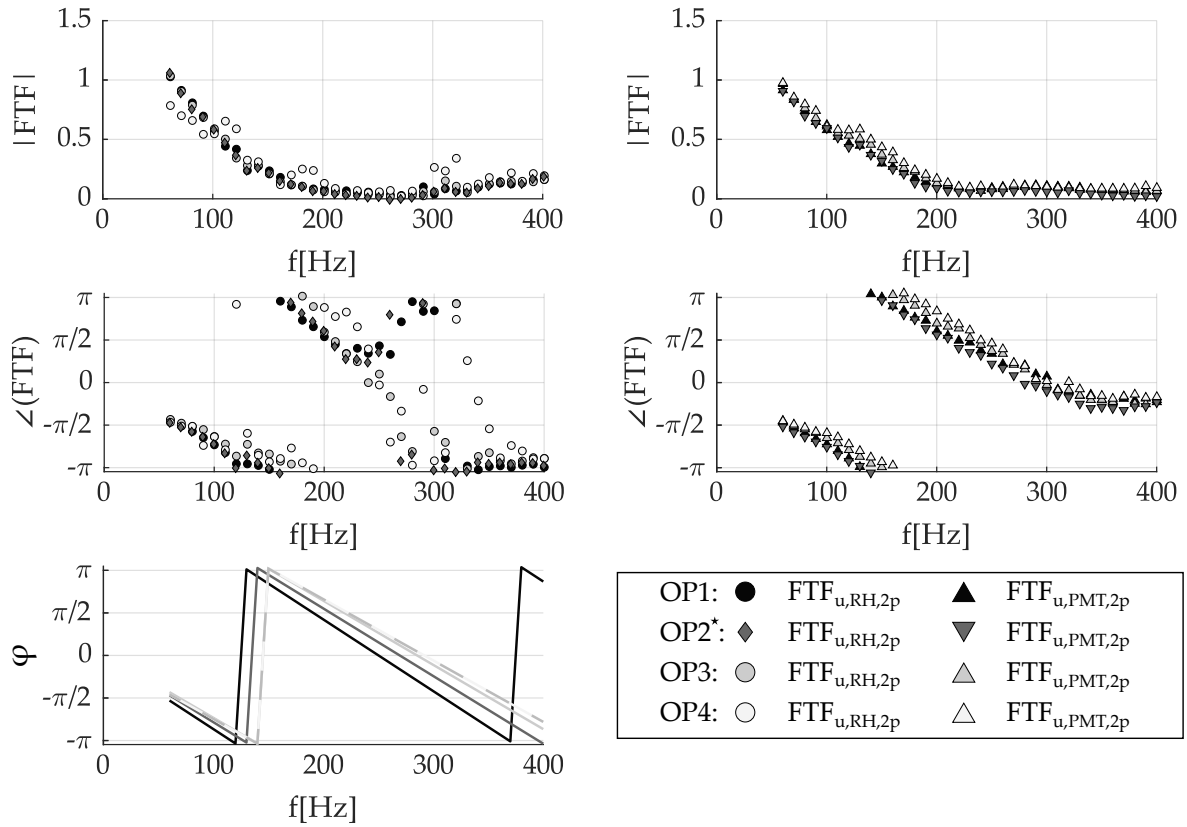

Figure 7.7: Flame transfer functions for operating points OP1-4; ordered by reactivity, with the most reactive OP1 in dark gray and the least reactive OP4 in light gray; left: pure acoustic FTF_{RH} in dot markers; right: hybrid FTF_{PMT} in triangle markers; bottom left: phase angle φ given by the time delay model (dashed gray line for OP4).

flame length for richer OPs and a shorter flame length for leaner ones ($L_{\mathrm{F,OP1}} > L_{\mathrm{F,OP4}}$). The change in flame length is depicted in Fig. 7.8 as the flame center of gravity x_{COG}, a well-known measure for the flame length.

Figure 7.8 depicts the normalized time-averaged $\mathrm{OH}^{\star}$-intensity distribution images for OP1 and OP4, along with relevant flame parameters. The normalization was performed with individual maximum intensity values of each image, as normalization with the overall maximum value

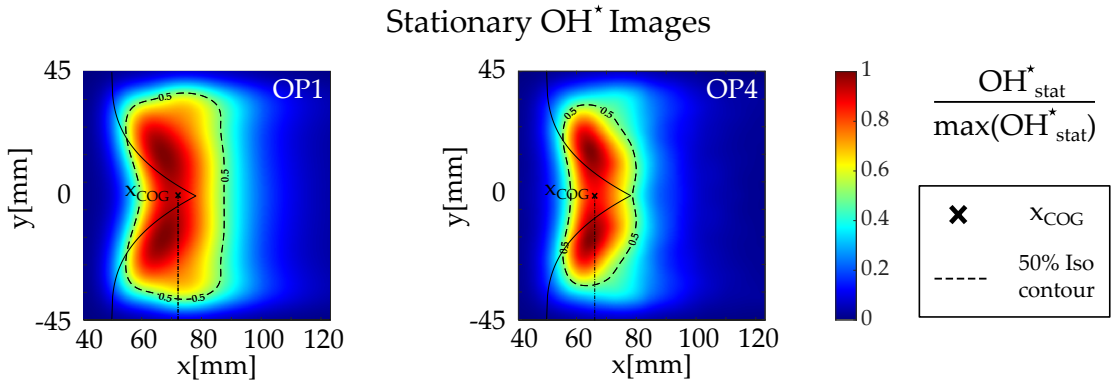

Figure 7.8: Stationary images of the $OH^{\star}$ intensity depicting the changes in flame length with the flame center of gravity x_{COG} for the operation points OP1 and OP4.

was not feasible, owing to the several orders of magnitude difference between $OH^{\star}_{max,OP1}$ and the least reactive point $OH^{\star}_{max,OP4}$. The flame length was determined using the flame center of gravity x_{COG}, and the 50% $OH^{\star}$-intensity isocontour was included in each image. Additionally, the plot depicts the analytically estimated jet center-line trajectory for the upper and lower mixing air jets entering the combustion chamber until the maximum penetration depth at the combustor center-line is reached.

The stationary images demonstrate that the flame shape in both cases is similar, and that the $OH^{\star}$ distribution is explainable with the JIC theory. The jets that enter the combustion chamber bend immediately due to the moderate momentum flux ratio J and are then distorted from the initial circular shape to a rising kidney shape. This distortion leads to the characteristic counter-rotating vortex pair (CVP) on the leeward side of the jet, which has been extensively studied [103–105]. Heat release starts on the windward side of the jet root, where scalar dissipation and moderate shear stress are low, while regions of high strain and quenching exhibit almost no $OH^{\star}$ radicals. The combustion expands around the jet, merges on the leeward side, and then travels along the jet direction into the CVP [106]. The opposing jet configuration and

the CVP favor entrainment and heat release on the leeward side. In the inner region of the CVP, low scalar dissipation rates, moderate shear, and low flow velocity result in a longer residence time, and high heat release, which is where the $OH^{\star}$ intensity peak is located for all operating points [96]. The different levels of equivalence ratio between the operating points change the flame length and position of x_{COG}, with less reactive OPs leading to shorter and more reactive OPs producing longer flames.

The phase response of the FTFs can be compared with the phase response φ derived via the time delay model presented in Chapter 4. The convective transport velocity u_{con} is a function of the jet mass fraction and velocity and decreases for less reactive operational points ($u_{con,OP1} > u_{con,OP4}$). A larger change in relative flame length than convective transport velocity ($d(L_F/L_{F,max}) > d(u_{con}/u_{con,max})$) is observed. As a result, the time delay τ decreases towards less reactive operational points ($\tau_{OP1} > \tau_{OP4}$). The phase response results in $\varphi = -\tau/2\pi f \rightarrow \varphi_{OP1} < \varphi_{OP4}$, which is evident in the measurement data and phase response φ shown in the bottom left of Fig. 7.7. The resulting values for the time delays are summarized in Table 4.1 in Chapter 4. Comparing the phase response obtained from the FTF measurements and the time delay model reveals good agreement. The latter predicts a change in flame length and time delay concerning the change in flow conditions and momentum flux ratio J.

In addition to the measured FTFs for OP1 - 4, further operating points were assessed to explore the impact of varying parameters such as air mass flow rates and momentum flux ratio J. The subsequent paragraphs present and discuss the results obtained for these operating points.

7.4 Flame Response with Constant Momentum Flux Ratio and Stiff Mixing Air Jets

In the following section, the operation point of the test rig is varied by altering the fuel flow rate while keeping the air mass flow ratios constant. This results in a constant pressure drop across the mixing ports and, consequently, a fixed jet velocity and momentum flux ratio J. These operating conditions, designated as OP5 - 7, were examined and compared to the OP1 - 4 range. Both ranges overlap at the baseline OP2*.

The FTFs of OP5 - 7 obtained from the RH and PMT measurements are displayed in Fig. 7.9. The time delay model is also evaluated, and the resulting phase graphs φ for the OP5 - 7 range are presented in the bottom left corner. The results for OP2* are depicted using gray markers as reference, while the remaining FTFs are shown as pinkish markers. For all FTFs of OP5 - 7 a similar behavior to those for OP1 - 4 in Fig. 7.7 is observed.

The FTFs based on RH on the left show a maximum value at $f = 60\,\mathrm{Hz}$ and drop to very low values from $f = 200\,\mathrm{Hz}$ on. The slightly spread amplitudes indicate the sensitivity to the measured temperatures before and after the flame (T_{cold} and T_{hot}) used for calculation. Also, the phase of all RH FTFs starts to scatter for frequencies $f > 200\,\mathrm{Hz}$ due to the very low amplitude values. The largest scattering is observed for OP7, again being the least reactive OP with only a minimal temperature increase between the cold and hot measurements. Contrary to OP1 - 4, all phases now fall on each other. This can be seen very well in regions of significant amplitudes from $f = 60 - 200\,\mathrm{Hz}$.

All OPs indicate the same time delay over the operating range. With constant air mass flow rates in both zones, the operating point is changed by changing the fuel rate in the first stage. Keeping the momentum flux ratio J and the jet velocity u_{jet} constant at its design value conditions is ideal for mixing and entrainment. Comparing the

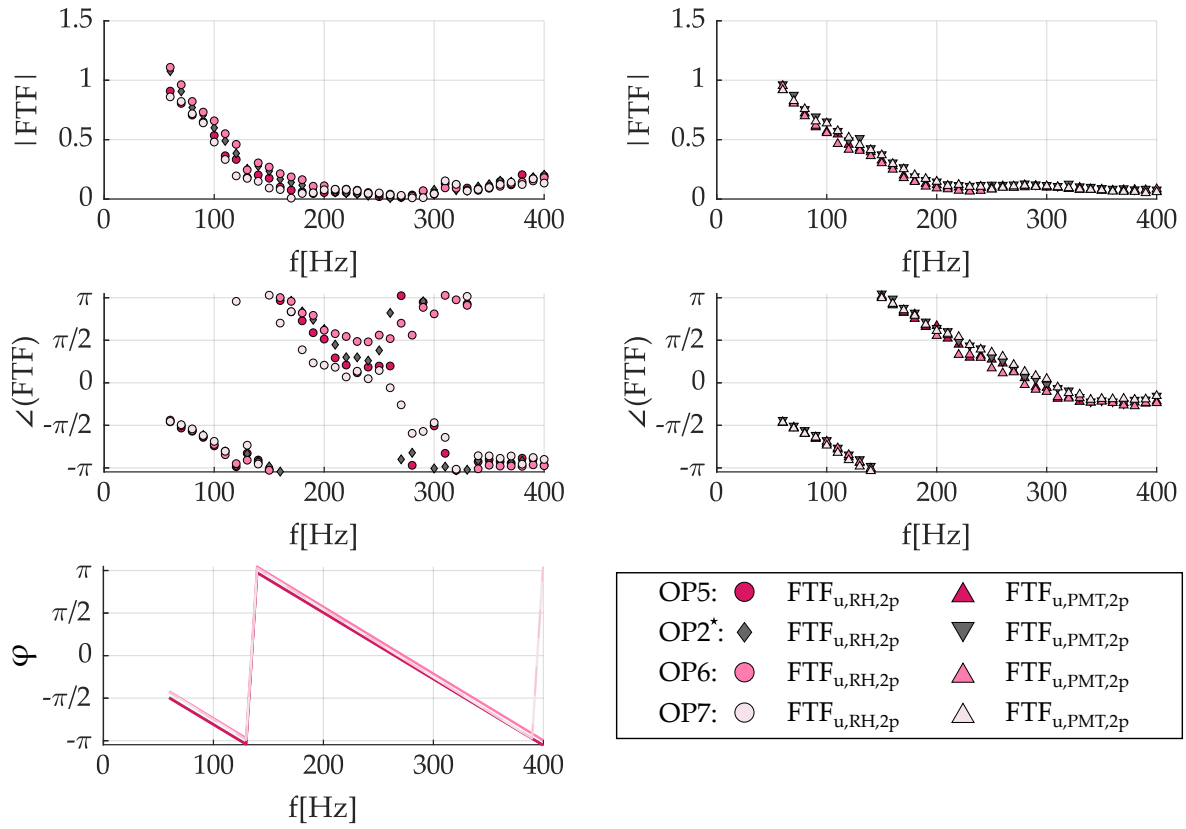

Figure 7.9: Flame transfer functions for OP2* in gray and OP5 - 7; ordered by reactivity, with the most reactive OP5 in dark pink and the least reactive OP7 in light pink; left: pure acoustic FTF_{RH} in dot markers; right: hybrid FTF_{PMT} in triangle markers; bottom left: phase angle φ given by the time delay model (dashed pink line for OP7).

individual OP with the same equivalence ratio, e.g., $\phi_{\mathrm{tot}} = 0.63$, reveals the overall mixing quality as the dominant physical process changing the phase response. The higher air mass flow rates of OP5 compared to OP1 increases the convective velocity thus $u_{\mathrm{con,OP5}} > u_{\mathrm{con,OP1}}$. The lower air mass flow rates of OP6 and OP7 decrease the convective velocity thus $u_{\mathrm{con,OP6}} < u_{\mathrm{con,OP3}}$ and $u_{\mathrm{con,OP7}} < u_{\mathrm{con,OP4}}$. This change in convective velocity in the jet shear layer compensates the change in flame length, resulting in identical time delays across the range of equivalence ratios.

The PMT FTFs on the right side show very good agreement compared to the amplitudes and phase values of the RH FTFs. With all OPs (OP2*, OP5 - 7) operating under design conditions with constant momentum flux ratio J, the entrainment rate can be assumed constant, and mixing behavior and quality for each OP remains the same. For all OPs, the same low-pass behavior with almost identical amplitude and phase values is observed.

For OP2* and the range of OP5 - 7, the phase response is almost constant given the unchanging design conditions, air mass flow ratios, and momentum flux ratio J. The resulting phases are consistent with the predictions of the time delay model φ based on entrainment theory. The corresponding phases for φ from theory are presented in the bottom left of Fig. 7.9.

8 Flame Response to Primary Zone and Mixing Jet Velocity Fluctuations

In this chapter, the secondary zone is evaluated regarding velocity fluctuations from the end of the primary zone and the mixing jets using the MISO method proposed in Chapter 3. Therefore, an open boundary plate is placed upstream of the mixing jet nozzles. Before investigating the influence of individual operating points on the dynamic flame behavior, the applicability of the MISO method is verified by comparing its results with two asymptotic cases where the individual flame responses could be isolated. This verification is carried out based on OP1.

After confirming the suitability of the MISO method, the operating range OP1 - 4 is investigated with changing air mass flow ratios and momentum flux ratio J. The influence of constant air mass flow ratios and momentum flux ratio J is discussed based on OP5 - 7. Furthermore, the section also includes the evaluation of various mixing air jet diameters and configurations within OP8 - 10. This analysis specifically examines the impact of changing mixing air jet diameter d_{jet} and row pattern on the FTFs of the lean secondary zone.

For all operating points, the FTFs obtained with a PMT are compared with those obtained with the pure acoustic MISO method. For each OP, the phase response of both FTFs is compared with the time delay model presented in Chapter 4.

8.1 MISO Network Approach Verification

Figure 8.1 shows the resulting FTFs for the most reactive operation point OP1. In the top graph, the amplitude of the MISO method $FTF_{\mathrm{u,M}}$ is compared with the verification FTF data obtained in Chapter 7. In the

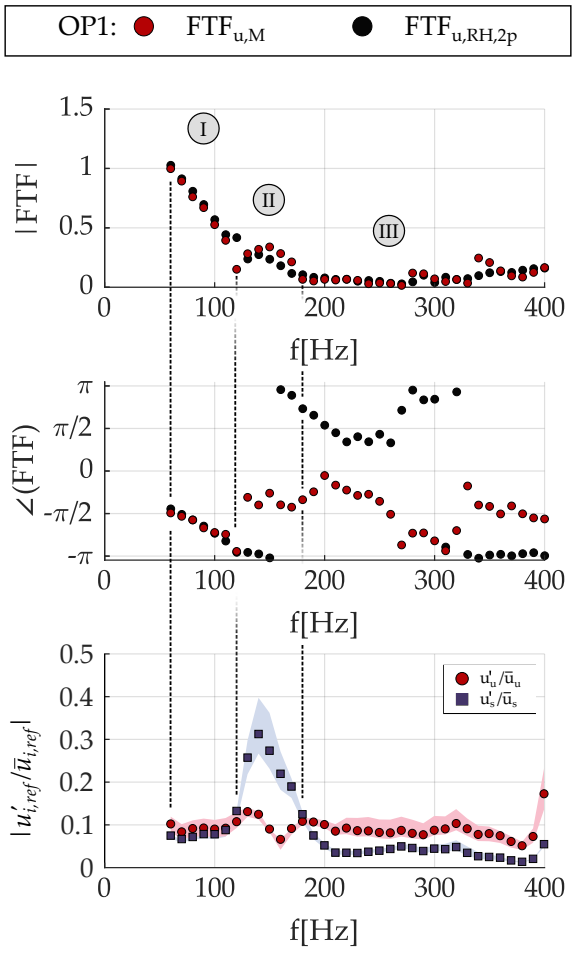

Figure 8.1: Flame transfer function of OP1; top: amplitude $|(\,)|$ of $FTF_{\mathrm{u,M}}$ in red dots obtained via the MISO method, compared to $FTF_{\mathrm{u,RH,2p}}$ in black dots; middle: corresponding phase $\angle(\,)$ of the two FTFs; bottom: normalized velocity fluctuations upstream $u'_{\mathrm{u}}/\bar{u}_{\mathrm{u}}$ in red dots and side $u'_{\mathrm{s}}/\bar{u}_{\mathrm{s}}$ in blue squares during an upstream forcing with the standard deviation (shaded surface) for the operating range.

latter, choked orifices were utilized upstream of the mixing jet nozzles to suppress the acoustic response of the mixing air jets ($u'_{\mathrm{s}} = 0 \rightarrow R_{\mathrm{s}} \approx 1$), which allowed the isolation of the response to primary zone velocity fluctuations u'_{u}. The resulting verification data and FTFs are marked with the subscript $(\,)_{\mathrm{u,2p}}$. The middle graph shows the comparison of the FTF phase response, and in the bottom graph, the relative velocity fluctuations upstream and in the mixing jets obtained in the measurements for upstream forcing are shown.

The frequency response characteristics of the system and the discussion is divided into three frequency ranges denoted by Ⓘ, Ⓘⓘ, and Ⓘⓘⓘ. The first range spans from 60 Hz to 120 Hz, and within this range $FTF_{\mathrm{u,2p}}$ and $FTF_{\mathrm{u,M}}$ exhibit good agreement. In the second range, although the amplitudes still compare well, the phase of $\angle FTF_{\mathrm{u,M}}$ jumps to just below $-\pi/4$, while $\angle FTF_{\mathrm{u,2p}}$ drops further. In Fig. 8.1, the relative velocity fluctuation amplitudes for the upstream $u'_{\mathrm{u}}/\bar{u}_{\mathrm{u}}$ and side mixing air jets $u'_{\mathrm{s}}/\bar{u}_{\mathrm{s}}$ indicates that the side branch experiences a damped resonance frequency and reaches rather high amplitudes up to 40%. This behavior results from two effects. During an eigenfrequency and forced response analysis using a 1D network system, a longitudinal mode was identified that couples with the perpendicular side ducts, leading to strong fluctuations in the side ducts in this frequency range. Additionally, the downstream perforated plate has a high reflection coefficient in this frequency range, and an almost standing wave pattern can evolve. The wave field reconstruction with the MMM reveals pressure anti-nodes at the position of the mixing air jets. The strong crossflow pressure fluctuations p'_{u} due to the eigenfrequency, result in high acoustic velocity fluctuations in the mixing air ports, as shown in the bottom part of Fig. 8.1. The latter leads to a strong crossflow to jet nozzle coupling, and the high induced velocity fluctuations.

The crossflow to jet nozzle coupling and the high induced velocity fluctuations in the jets strongly affect the mixing and combustion process of the inverse diffusion flame. With the remaining low fuel level to be

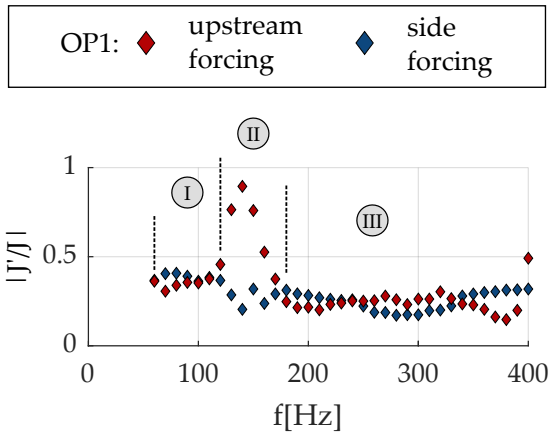

Figure 8.2: Normalized momentum flux ratio fluctuations J'/J of OP1 for upstream forcing in red and side forcing in blue.

burned in the secondary zone, the flame is sensitive to changes in the momentum flux- and velocity ratio J and R. Both are key parameters for the evolution of hydrodynamic structures in JIC and enhance mixing and entrainment. In Fig. 8.2, the linearized and normalized momentum flux ratio $J'/\bar{J}$ for upstream and side forcing is shown. The strong jet nozzle coupling during upstream forcing causes a strong fluctuation of momentum flux ratio J'/J indicated with the red diamonds. The strong fluctuations of the jets create toroidal ring vortices that penetrate further into the crossflow. The resulting steepening and over-penetration of the jets changed the mixing characteristics for the worse. Consequently, the flame length shortens, shifting its center of gravity x_{COG} upstream towards the reference plane x_{u}. Similar behavior was also discovered by Marr et al. [36], and Erogul and Breidenthal [33]. Analogous to the change in flame length caused by a variation of the operational point, the time delay τ decreases, thus shifting the phase to smaller values. At any rate, the substantial variation in oscillation amplitude through this region makes evaluating the FTF difficult.

The last region Ⓘ shows amplitudes of almost zero for both FTFs. The velocity fluctuations are back in the linear regime, but the flame seems

unaffected. Due to the very low amplitudes, the associated phase values are arbitrary in this frequency range, making the data questionable in this region.

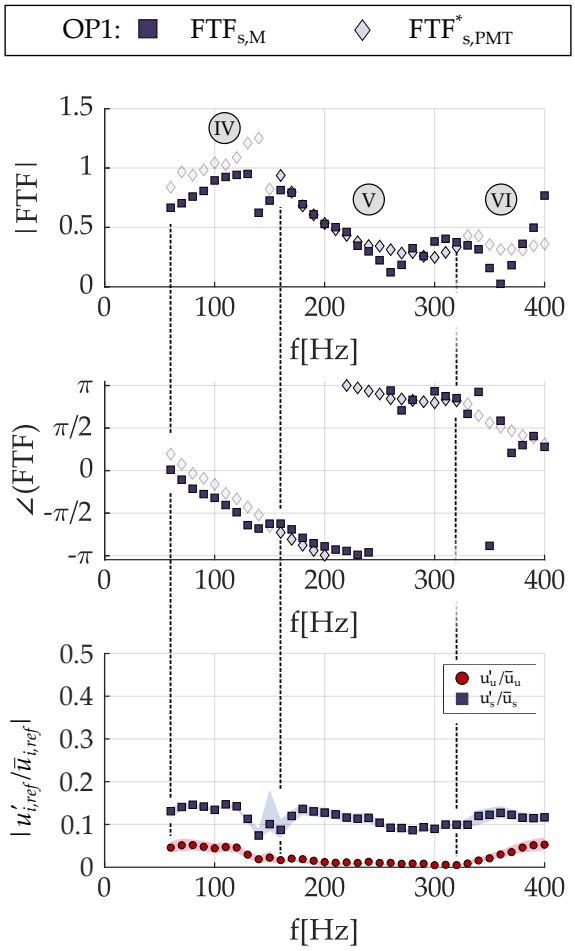

Figure 8.3: Flame transfer function of OP1; top: amplitude $|(\,)|$ of $FTF_{\mathrm{s,M}}$ in blue squares obtained via the MISO method, compared to $FTF^{*}_{\mathrm{s,PMT}}$ in gray diamonds extracted from PMT OH* CL measurement with forcing from the side; middle: corresponding phase $\angle(\,)$ of the two FTFs; bottom: normalized velocity fluctuations upstream $u'_{\mathrm{u}}/\bar{u}_{\mathrm{u}}$ in red dots and side $u'_{\mathrm{s}}/\bar{u}_{\mathrm{s}}$ in blue squares during a side forcing with the standard deviation (shaded surface) for the operating range.

The side FTFs for the operation point OP1 with the highest reactivity are displayed in Fig. 8.3. The top and middle graph of Fig. 8.3 depict the amplitude and phase of $FTF_{\mathrm{s,M}}$, respectively, using dark blue square markers. The amplitude rises from 60 Hz to a global maximum plateau at $110 - 130$ Hz with $|FTF_{\mathrm{s,M}}| = 0.95$. Subsequently, the FTF linearly decreases to a local minimum at 260 Hz, after which it increases again to a local maximum of $|FTF_{\mathrm{s,M}}| = 0.40$ at 310 Hz. The phase of $\angle FTF_{\mathrm{s,M}}$, displayed in the middle graph of Fig. 8.3, starts at a value of zero at 60 Hz and shows a constant decreasing linear trend, with a small change in sign close to $130 - 150$ Hz. The phase starts to scatter from 310 Hz and exhibits the same random behavior as the amplitude.

A secondary evaluation was conducted to verify the $FTF_{\mathrm{s,M}}$ obtained through the acoustic MISO method for the side velocity fluctuations. As stiff boundaries failed to suppress the upstream velocity fluctuations $u'_{\mathrm{u}}/\bar{u}_{\mathrm{u}}$, an alternative approach was employed. The OH* CL that yielded favorable outcomes previously was utilized again. Regions with minimal upstream velocity fluctuations $u'_{\mathrm{u}}/\bar{u}_{\mathrm{u}}$ were identified during side forcing. Under these conditions, Eq. 6.14 was reduced to a formulation where the global intensity fluctuation is solely dependent on $u'_{\mathrm{s}}/\bar{u}_{\mathrm{s}}$:

$$\frac{I'_{\mathrm{OH}^\star}(\omega)}{\bar{I}_{\mathrm{OH}^\star}(\omega)} = FTF_{\mathrm{u,PMT}}(\omega)\underbrace{\frac{u'_{\mathrm{u}}(\omega)}{\bar{u}_{\mathrm{u}}}}_{=0} + FTF_{\mathrm{s,PMT}}(\omega)\frac{u'_{\mathrm{s}}(\omega)}{\bar{u}_{\mathrm{s}}} \tag{8.1}$$

$$\frac{I'_{\mathrm{OH}^\star}(\omega)}{\bar{I}_{\mathrm{OH}^\star}(\omega)} = FTF^{*}_{\mathrm{s,PMT}}(\omega)\frac{u'_{\mathrm{s}}(\omega)}{\bar{u}_{\mathrm{s}}} \tag{8.2}$$

The FTF coupling the heat release rate and the velocity fluctuations was then denoted by $FTF^{*}_{\mathrm{s,PMT}}$ and represented with gray diamonds. The $FTF^{*}_{\mathrm{s,PMT}}$ was obtained through side forcing and is compared to $FTF_{\mathrm{s,M}}$ in Fig. 8.3. The analysis of the FTFs revealed three ranges, �IV, ⑤, and ⑥. In ranges �IV and ⑥, $u'_{\mathrm{u}}/\bar{u}_{\mathrm{u}}$ exhibited a significant amplification of around 4 - 5%, as illustrated in the bottom graph of Fig. 8.3. In these regions, the amplitude and phase of both FTFs differed greatly as the

flame reacted to both fluctuations, and $FTF^{*}_{s,PMT}$ was only referred to the side. Conversely, the flame only responded to the velocity fluctuations from the side in the range Ⓥ, where extremely low upstream velocity fluctuations were observed. In this range, the amplitude and phase of both FTFs were in good agreement with minor deviations at $f = 260\,\text{Hz}$ and 300 Hz. These results corroborated the findings of the pure acoustic MISO method.

The side flame transfer function FTF_s is also affected by high forcing amplitudes and jet nozzle coupling during upstream forcing, similar to the upstream flame transfer function FTF_u. However, this time it is the amplitude that changes. The effect of increasing forcing amplitudes on flame dynamics has been investigated by several studies, which have used flame describing functions (FDFs) to capture the results [107–110]. The response of a system to inlet velocity fluctuations can become non-linear when the forcing amplitude is increased while keeping the equivalence ratio constant. This transition between linear and non-linear behavior is frequency-dependent.

In the experiments of Balachandran et al. [107], and Schimek et al. [110], the magnitude of the FTF decreased as the forcing amplitude increased, with this effect being stronger for higher frequencies than lower ones. It should be noted that up to a certain level of forcing amplitude, no substantial flame surface modification occurred despite amplitudes changes. However, when the forcing frequency exceeded a certain range, roll-up on the flame surfaces could be observed, which depended heavily on the respective magnitudes of the forcing amplitude. This roll-up coincided with the shedding of vortices from the lip of a bluff body, such as an injector or the jet nozzle exit, and the resultant distortion of the flame sheets and shear layer. The shift to a lower FTF magnitude with higher forcing amplitude could explain the shift seen in the frequency range Ⓘⓥ, as shown in Fig. 8.4. The presented FDFs on the right are purely heuristic and have not been measured. A shift to a lower FDF could be possible with the strong increase in amplitude.

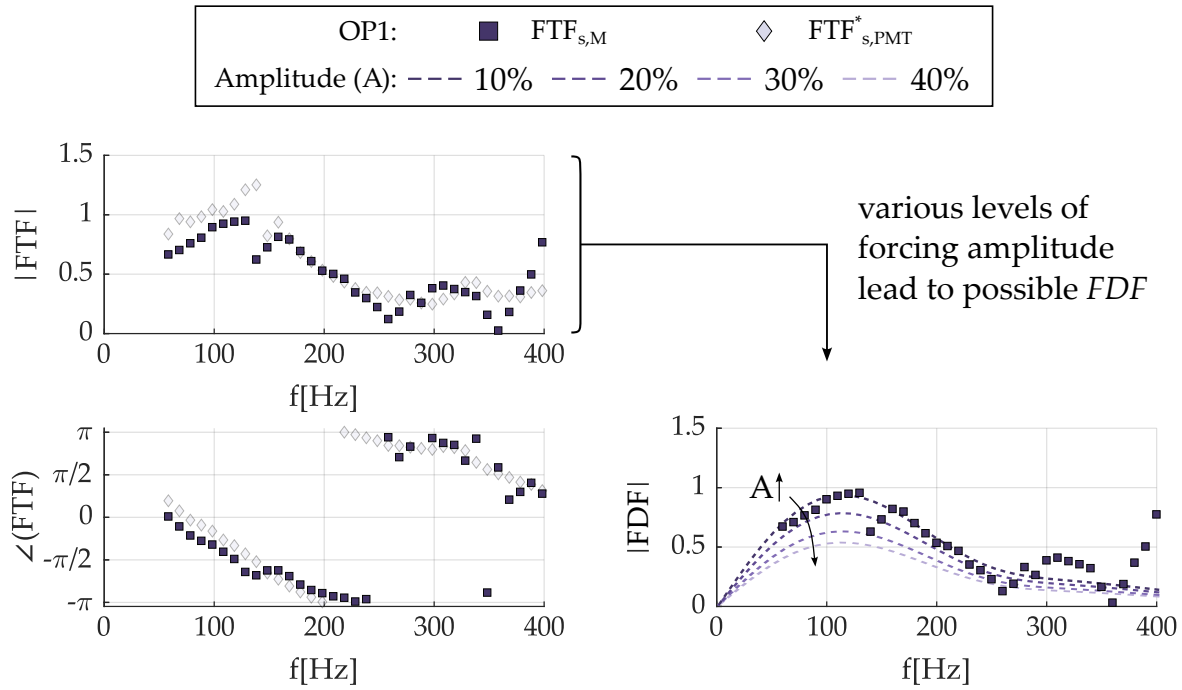

Figure 8.4: Flame transfer function of OP1; left: $FTF_{s,M}$ in blue squares obtained via the MISO method, compared to $FTF^{*}_{s,PMT}$ in gray diamonds extracted from PMT OH^{*} CL measurement during a side forcing; right: multiple analytical flame describing functions FDF_s depending on various amplification amplitudes (A); heuristic graphs are shown based on literature.

Palies et al. [109] and Schimek et al. [110] also found the strongest nonlinear behavior in regions where the heat release and $OH^{\star}$ CL fluctuation reaches its maximum, which is also confirmed in this study.

Comparison of MISO method to $OH^{\star}$ CL measurements

The FTFs measured with the PMT, $FTF_{u,PMT}$ and $FTF_{s,PMT}$, were computed using a regression approach based on the "hot" measurements and Eq. 6.14. The resulting FTFs are compared to those obtained from the MISO method, $FTF_{u,M}$ and $FTF_{s,M}$, and the comparison results are presented in Fig. 8.5.

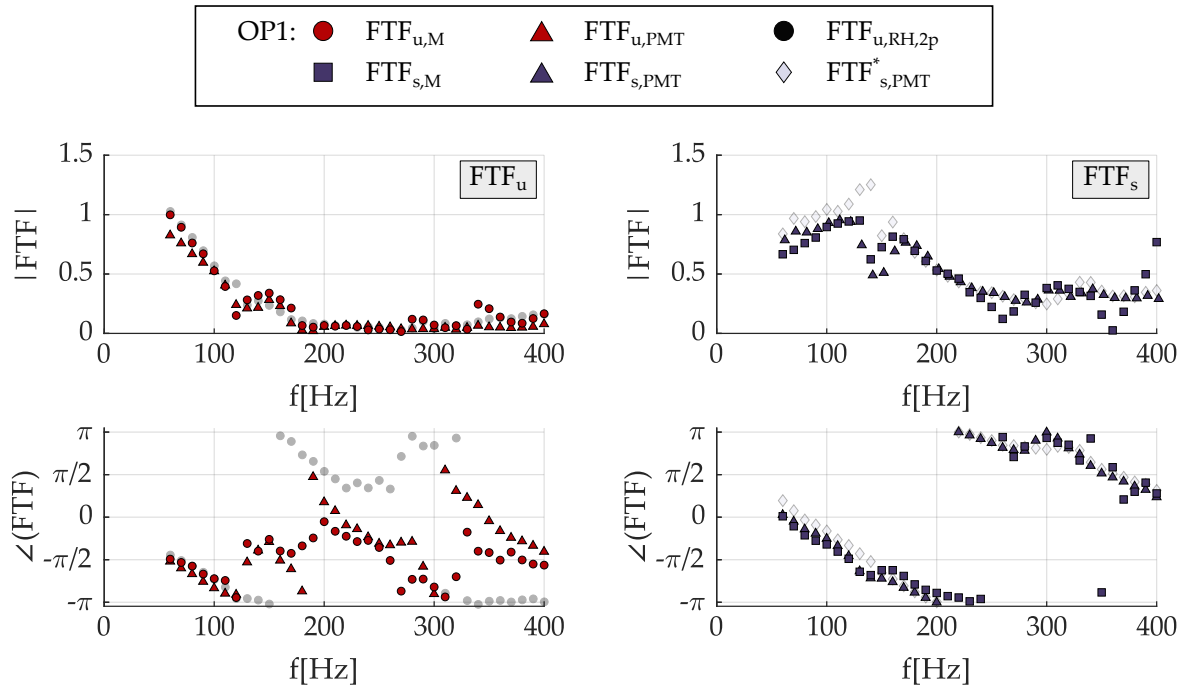

Figure 8.5: Flame transfer function of OP1; left: $FTF_{\mathrm{u,M}}$ in dark red dots obtained via the MISO method, $FTF_{\mathrm{u,PMT}}$ in dark red triangles extracted from PMT measurements, in the background, $FTF_{\mathrm{u,RH,2p}}$ in black dots with acoustically stiff jets serves as a reference; right: $FTF_{\mathrm{s,M}}$ in dark blue squares obtained via the MISO method, $FTF_{\mathrm{s,PMT}}$ in dark blue triangles extracted from PMT measurements, in the background, $FTF^{*}_{\mathrm{s,PMT}}$ in light gray diamonds serves as reference.

In the left column of Fig. 8.5, the upstream FTFs are shown, and good agreement is observed between $FTF_{\mathrm{u,PMT}}$ and $FTF_{\mathrm{u,M}}$ over the entire frequency range. However, minor deviations are observed at very low frequencies. Additionally, the phase of the PMT measurements shows similar behavior to the MISO FTFs. Based on the three frequency ranges shown in Fig. 8.1, it is apparent that in the range Ⓘ, $FTF_{\mathrm{u,PMT}}$ has the same monotonic trend as $FTF_{\mathrm{u,M}}$. In range Ⓘⓘ, the PMT approach is also sensitive to jet nozzle coupling, inducing the high side velocity fluctuations. As previously discussed, the same phase jump resulting

from jet flapping and the toroidal ring vortices is seen. In range Ⓘⅈⅈⅈ, the PMT phase shows minor scattering and remains the linear decreasing characteristics towards higher frequencies. The $FTF_{\mathrm{u,PMT}}$ appears more robust than the pure acoustic MISO method, owing to a better signal-to-noise ratio of the PMT signal and the calculated velocity fluctuations. However, at very low amplitudes, the phase values remain questionable.

In the right column of Fig. 8.5, the side FTFs are compared. For the side FTFs, the $FTF_{\mathrm{s,PMT}}$ also shows excellent agreement with the $|FTF_{\mathrm{s,M}}|$ for the amplitude. Minor deviations are observed around $f = 150\,\mathrm{Hz}$ and at 260 Hz. The $\angle FTF_{\mathrm{s,PMT}}$ shows the same linear decline and thus the same time delay as the $\angle FTF_{\mathrm{s,M}}$. The advantages of the PMT approach became more apparent when considering the various frequency ranges. In range Ⓘⅴ, the amplitude and phase of $FTF^{*}_{\mathrm{s,M}}$ based only on a side forcing exceeded the $FTF_{\mathrm{s,M}}$. In contrast, $FTF_{\mathrm{s,PMT}}$ matches almost perfectly. In range Ⓥ, where the upstream fluctuations were very low, all FTFs show similar good agreement. Finally, for range Ⓘⅵ, both FTFs based on the PMT show the same trend, while the MISO FTF is prone to scattering. In summary, the PMT approach is found to be more robust than the MISO method for calculating the FTFs.

Crossflow to Jet Coupling

The crossflow in RQL combustion systems is inherently unsteady due to coherent acoustic oscillations, as explained in the introduction. Previous studies by Wilde [11] indicated that low-frequency crossflow acoustics provide both asymmetric and axisymmetric excitation of the jets. The fluctuating upstream crossflow velocity from the primary zone u'_{u}, induces a asymmetric velocity response. On the other hand, the fluctuating upstream pressure p'_{u} induces a time-varying pressure drop across the jet nozzles, which leads to a fluctuating jet exit velocity u'_{s} that axisymmetrically excites the jets. This axisymmetric excitation of the jet is called jet nozzle coupling to emphasize the similarity with

behavior observed in liquid rocket instability research and causes periodic jet flapping. The coupling magnitude depends heavily on the JIC parameters, such as J, R, and S.

The upstream forcing excites the inverse diffusion flame through both a jet nozzle coupled mechanism and the direct action of the fluctuating upstream velocity, as shown in the bottom graph of Fig. 8.1. In most cases, the upstream to jet nozzle coupled mechanism dominates, and forcing the jets does not lead to significant upstream fluctuations, as illustrated in the bottom graph of Fig. 8.3. The jet nozzle coupling and the individual jet forcing from the side lead to a dynamic broadband flame response described by the FTF_s. Contrary, the dynamic flame response to upstream fluctuations, FTF_u, is only noticeable in the low-frequency range, as depicted in Fig. 8.5.

The magnitude and phase of the fluctuating jet exit velocity u'_s relative to the fluctuating upstream velocity u'_u is depending on the acoustic mode shape and the jet nozzle impedance Z_{jet}. The facility boundary conditions and the thermoacoustic properties of the primary zone injector influence the acoustic pressure and velocity mode shapes. Additionally, the jet nozzle impedance, which controls the fluctuating jet exit velocity induced by the fluctuating crossflow pressure, depends on the acoustic boundary conditions and the nozzle geometry. Thus, a different JIC configuration may exhibit a different JIC response to upstream forcing, which will be discussed in Section 8.4.

Low Frequency Limits of the FTFs

This section concerns the low-frequency limits of both FTFs. For the low-frequency limit $f \rightarrow 0$ of the upstream FTFs, the amplitude can be extrapolated towards $|FTF_u| \approx 1$. The phase becomes $\angle FTF_u \approx 0$, characteristic for non-premixed flames with stiff fuel injectors [70, 73]. Here the amplitude indicates a quasi-stationary thermal power modulation for the lower frequencies. The variance of the absolute values

results from the temperature measurements used in the MMM and the MISO method for T_{cold} and T_{hot}. The temperatures are not corrected for radiation effects. Thus, the resulting amplitude values of the MISO method $FTF_{\mathrm{u,M}}$ should be a little lower. This would shift $FTF_{\mathrm{u,M}}$ more towards $FTF_{\mathrm{u,PMT}}$.

The linear falling phase speaks for a constant convective time delay between the velocity fluctuations in the reference plane x_{u} and the heat release of the inverse diffusion flame.

For the side FTFs on the right of Fig. 8.5 the amplitude can be extrapolated towards $|FTF_{\mathrm{s}}| \approx 0$ for $f \to 0$. The side FTFs represent the flame reaction to u'_{s} at the position of air injection into the chamber. In the absence of significant modulation of the air flow, the entrainment of the inverse diffusion flame remains unaltered. As a result, the heat release and flame characteristics also remain unmodulated.

The phase of FTF_{s} is arbitrary if the amplitude approaches zero at the low-frequency limit. Nevertheless, it can be stated that both FTFs have the same trend for low frequencies. Additionally, it is worth mentioning that in Chapter 3 a constant offset of $\pi/2$ between the phase response of FTF_{u} and FTF_{s} is identified throughout the frequency range due to the linearity assumption, which necessitates perpendicular vectors. This is covered well by the phase response of both FTFs, $\angle FTF_{\mathrm{u}}$ and $\angle FTF_{\mathrm{s}}$.

8.2 Flame Response with Varying Momentum Flux Ratio

Figures 8.6 and 8.7 illustrate the FTFs corresponding to the flame response of the upstream and side velocity fluctuations, respectively, for the operating range OP1 - 4, as listed in Table 6.1. In the left column of each figure, the FTFs obtained from the pure acoustic MISO method are displayed, whereas the FTFs obtained using the hybrid PMT $OH^{\star}$ CL technique are shown in the right column.

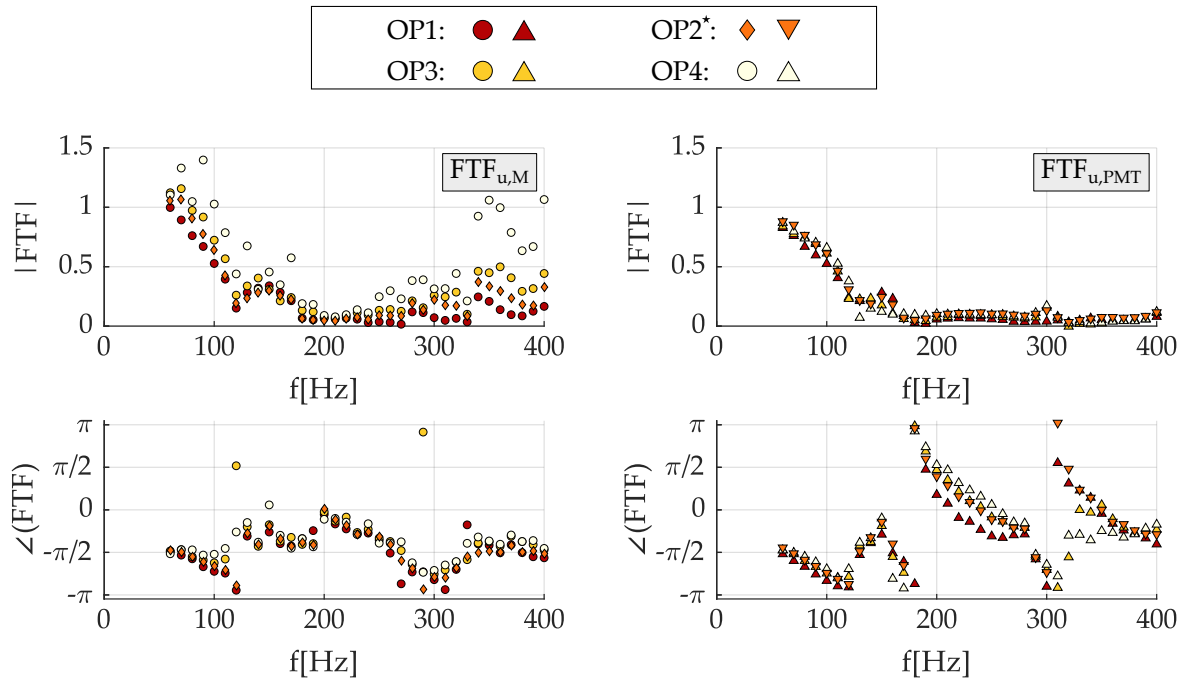

Figure 8.6: Flame transfer function for the operating range OP1 - 4; ordered by reactivity, with the most reactive OP1 in dark red and the least reactive OP4 in light yellow; left: $FTF_{\mathrm{u,M}}$ in dot markers obtained via the MISO method; right: $FTF_{\mathrm{u,PMT}}$ in triangle markers extracted from PMT measurements.

In Fig. 8.6, the trend of all FTF_{u} amplitudes is observed to be the same, with a global maximum at $f = 60\,\mathrm{Hz}$, followed by a local minimum around $f = 120\,\mathrm{Hz}$, and an increase in the regions of high jet nozzle coupling towards a local maximum at $f = 140 - 150\,\mathrm{Hz}$. Finally, the amplitudes are falling to values close to zero for higher frequencies. The phase response for OP1 - 4 also exhibits similar behavior and is consistent with the predicted gradient of the time delay model shown in the bottom part Fig. 7.7. However, OP4 demonstrates the highest deviation and spread due to the low heat release rate. Additionally, all FTFs in Fig. 8.6 conform to the low frequency limit of $|FTF_{\mathrm{u}}| \approx 1$, and the phase becomes $\angle FTF_{\mathrm{u}} \approx 0$.

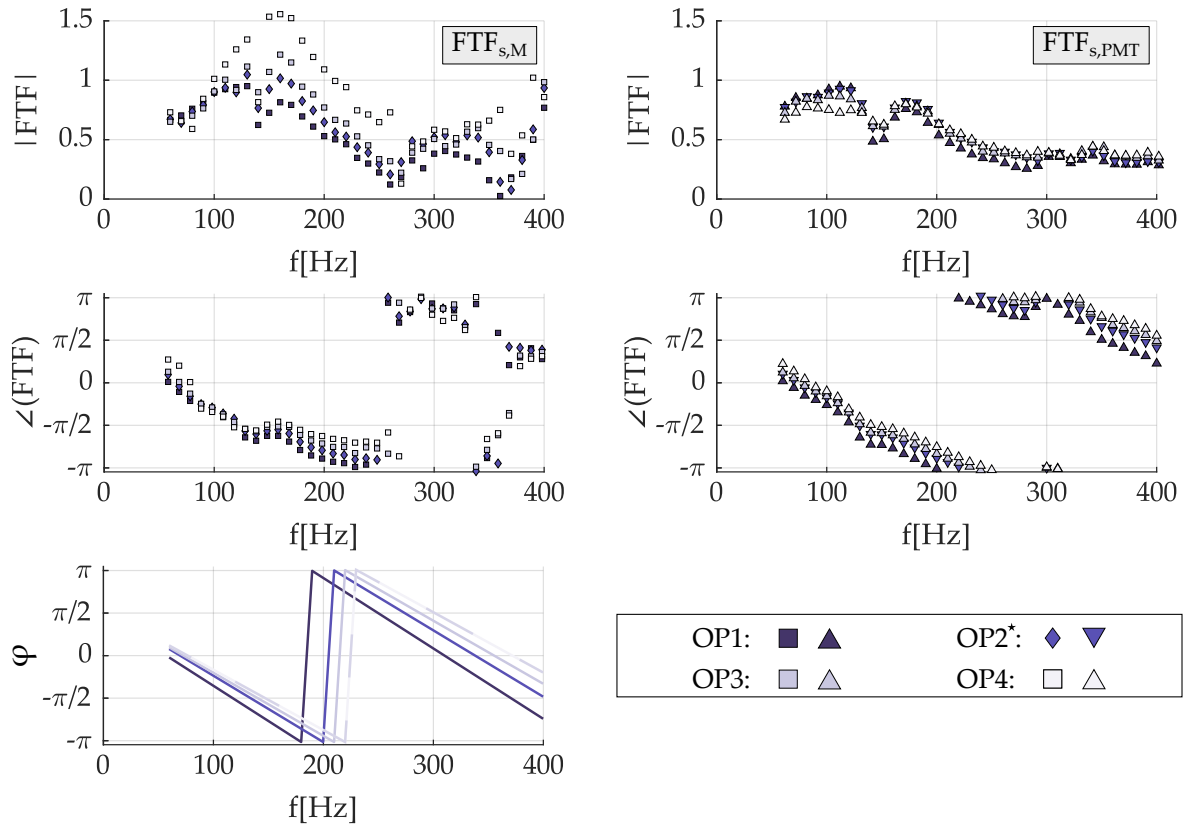

Figure 8.7: Flame transfer function for the operating range OP1 - 4; ordered by reactivity, with the most reactive OP1 in dark blue and the least reactive OP4 in light blue; left: $FTF_{\mathrm{s,M}}$ in square markers obtained via the MISO method; right: $FTF_{\mathrm{s,PMT}}$ in triangle markers extracted from PMT measurements; bottom left: phase angle φ given by the time delay model.

All $FTF_{\mathrm{s,M}}$ in Fig. 8.7 exhibit an increasing amplitude from OP1 to OP4. The amplitudes of $FTF_{\mathrm{s,PMT}}$ show a different behavior than the MISO ones, deviating by about -10% from the most to the least reactive OP. OP4 exhibits the highest deviation and scatter due to the low level of remaining heat release at this OP. Thus only a very low temperature increase from the cold to the hot case is observed. Therefore, the temperature measurement uncertainties lead to larger calculation errors in the MISO method compared with the optical method using the PMT.

The phase response shows a staggered behavior, with the steepest phase drop for OP1 towards the lowest for OP4, indicating a change in flame length towards shorter flames for less reactive OPs. All FTFs in Fig. 8.6 exhibit the low-frequency limit of $\angle FTF_{\mathrm{u}} \approx 0$.

Subsequently, the phase response is compared to predictions of the time delay model φ shown in the bottom left of Fig. 8.7. To cover the phase shift between the upstream and side FTFs in the time delay model, the phase difference of $|\Delta\varphi| \approx \pi/2$ from Chapter 4 is applied. The resulting time delay and phase for the side FTF indicate the same staggered phase graphs for OP1 - 4 as for the upstream FTFs in regions with significant amplification. Compared with the phase response of $FTF_{\mathrm{s,PMT}}$, very good agreement is observed. The measured phase drop becomes smaller for higher frequencies, which the time delay model could not cover.

Robustness

The behavior of the pure acoustic MISO FTFs indicated a stronger scattering towards less reactive operating points across the entire frequency range (Fig. 8.6 and 8.7). This observation is discussed in relation to OP4, where only 10% of additional heat release in the lean secondary zone follows fuel-rich combustion in the primary zone, leading to a small temperature increase from $T_{\mathrm{cold,OP4}} = 856\,\mathrm{K}$ to $T_{\mathrm{hot,OP4}} = 951\,\mathrm{K}$. As a result, the FTF becomes more vulnerable to measurement inaccuracies, particularly for less reactive OPs at very low levels of total equivalence ratio ϕ_{tot}.

To assess the dissimilarity between the cold **BSM** and hot **BFSM**, the Frobenuis norm is employed, which is normalized with the maximum deviation across all values. Fig. 8.8 depicts the results of this analysis for OP1 - 4. Higher values indicate a larger difference between **BSM** and **BFSM**, implying that flame heat release has a greater impact. Con-

Normalized Frobenuis norm: $$|A_{OP_i}|_{F,norm} = \sqrt{\sum_{n=1}^{3}\sum_{m=1}^{3}(BSM_{nm} - BFSM_{nm})^2}$$

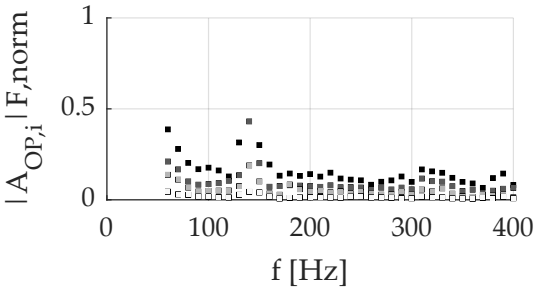

Figure 8.8: Normalized Frobenuis norm $|A_{\mathrm{OP_i}}|_{\mathrm{F,norm}}$ for each frequency between the individual **BSM** and **BFSM** matrices for the operating range.

versely, lower values suggest that the matrices are almost identical. OP4 scatters roughly around 1% for all frequencies. Given the small difference between the measurements with and without flame, the solution of the optimization problem becomes challenging, leaving the resulting data questionable. However, the hybrid PMT method is unaffected by such minor variations since it depends solely on the hot measurement. Consequently, it exhibits a more robust behavior, as demonstrated by $FTF_{\mathrm{u,PMT}}$ and $FTF_{\mathrm{s,PMT}}$, even for less reactive OPs. The amplitude and phase data for less reactive OPs with a slight temperature rise should be interpreted with caution.

8.3 Flame Response with Constant Momentum Flux Ratio

In OP5 - 7 the operating range was varied by adjusting the fuel mass flow rate in the primary stage while maintaining constant air mass flow ratios to ensure ideal mixing and entrainment conditions in the JIC configuration of the secondary zone. Figure 8.9 and 8.10 show the resulting FTFs obtained using the verified MISO method and the FTFs acquired through PMT measurements, which are thoroughly discussed.

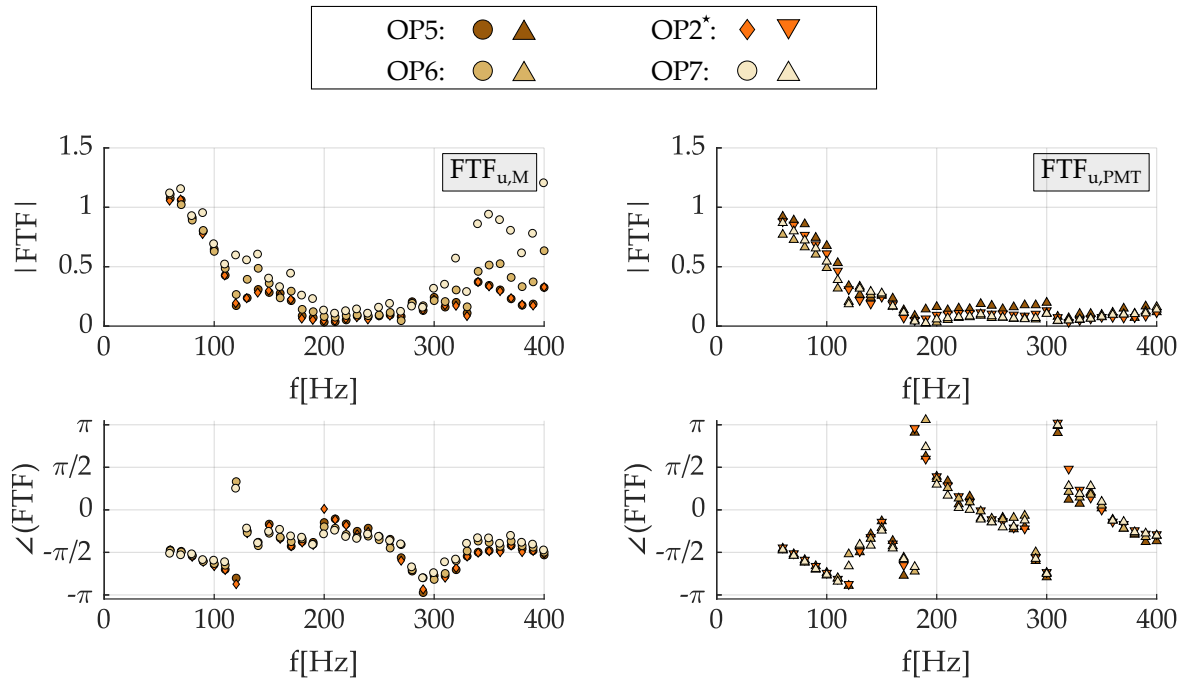

Figure 8.9: Flame transfer function for OP2* in orange and the operating range OP5 - 7; ordered by reactivity, with the most reactive OP5 in dark brown and the least reactive OP7 in light sand; left: $FTF_{\mathrm{u,M}}$ in dot markers obtained via the MISO method; right: $FTF_{\mathrm{u,PMT}}$ in triangle markers extracted from PMT measurements.

In Fig. 8.9 the FTFs showing the flame response to upstream velocity fluctuations for an equivalence ratio variation with constant air mass flow and momentum flux ratios are shown. Comparing the results to the 2-port measurements with stiff jets in Fig. 7.9 reveals similar trends. All FTF amplitudes show a global maximum and fall towards zero for higher frequency $f > 200\,\mathrm{Hz}$. A clear low-pass behavior is observed, and the jet nozzle coupling and the high side fluctuations still influence the FTFs in the range of $f = 120 - 180\,\mathrm{Hz}$. Again, the least reactive OP7 shows the highest scattering for the MISO $FTF_{\mathrm{u,M}}$.

On the right side, all $FTF_{\mathrm{u,PMT}}$ overlap with minor deviations in the low-frequency amplitudes. The phase response of both the MISO

and the PMT FTFs display a uniform linear pattern in regions with considerable amplitudes. For higher frequencies, however, where the FTF amplitude is close to zero, the accuracy of the phase response becomes suspect. Furthermore, since all mass flow ratios are kept constant while changing equivalence ratios, the response within the operating range remains unchanged in this regard. Consistent with the 2-port evaluation, reactivity-induced changes in flame position along with fluctuating convective velocities compensate each other and result in steady time delays, as already shown in the bottom left in Fig. 7.9.

Figure 8.10 presents the flame response to side fluctuations for the operating points OP2* and OP5 - 7. The MISO method results $FTF_{\mathrm{s,M}}$ are shown on the left. The amplitude behavior is similar to the one previously presented for OP1 - 4. The $FTF_{\mathrm{s,PMT}}$ results on the right side show a good agreement with the MISO FTFs. The amplitude response shows the same maxima and minima. An improvement for frequencies $f > 250\,\mathrm{Hz}$ compared to the $FTF_{\mathrm{s,M}}$ is found. Here, the PMT still shows constant amplitude and phase values. The overall deviation in amplitude is caused by the underlying **BSM**, **BFSM**, and temperature measurements.

In the frequency range of $f = 60 - 250\,\mathrm{Hz}$, the phase response $\angle FTF_{\mathrm{s,PMT}}$ for OP2* and OP5 - 7 is similar to the phase response of the MISO method $\angle FTF_{\mathrm{s,M}}$. All FTFs have a steady, declining phase response until scatter becomes noticeable at higher frequencies. With a constant momentum flux ratio J, the flame response to side fluctuation remains constant over the operating range, indicating that the quality and mixing process dominate the flame dynamics response and shift the phase depending on the flame length and convective velocity. The latter is a function of the air mass flow ratio. The matching phase response for OP2* and OP5 - 7 is also represented by the time delay model as shown in the bottom left of Fig. 8.10.

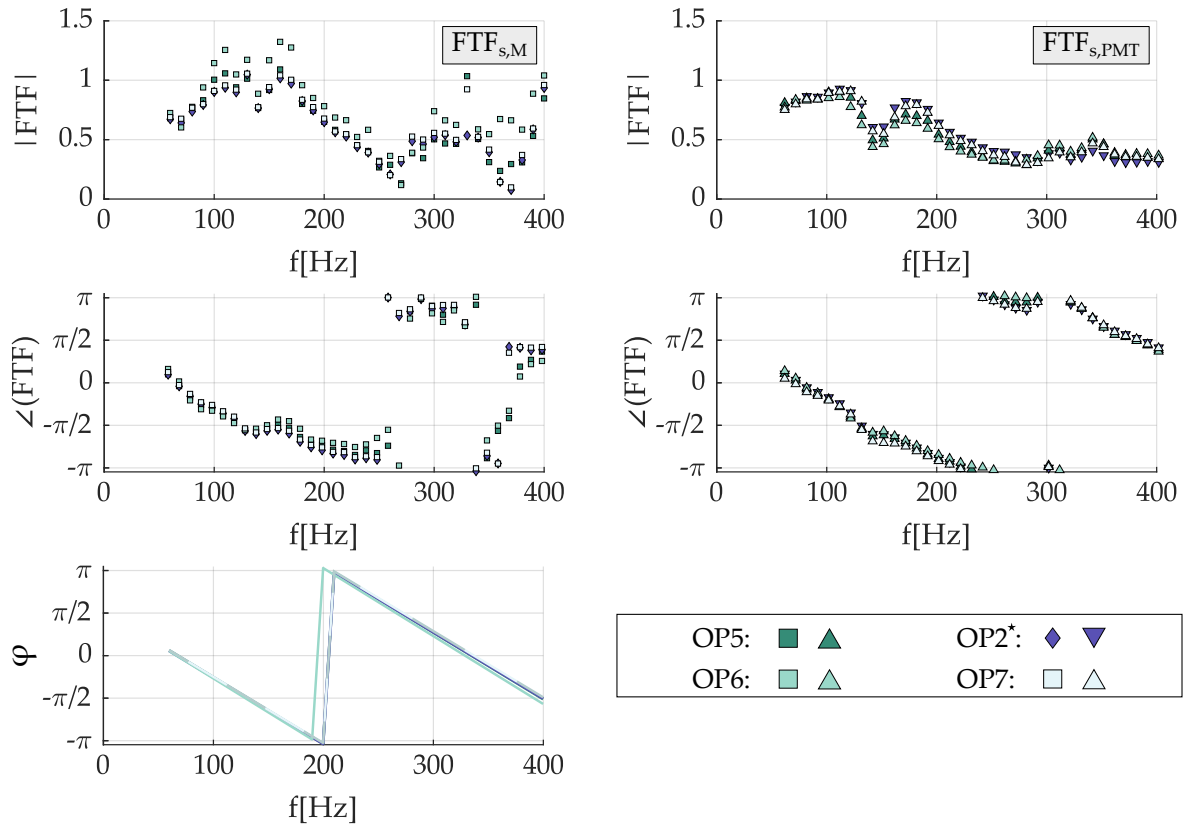

Figure 8.10: Flame transfer function for OP2* in purple and the operating range OP5 - 7; ordered by reactivity, with the most reactive OP5 in dark green and the least reactive OP7 in light green; left: $FTF_{s,M}$ in square markers obtained via the MISO method; right: $FTF_{s,PMT}$ in triangle markers extracted from PMT measurements; bottom left: phase angle φ given by the time delay model.

8.4 Flame Response for Different Jet Configurations

In order to investigate the impact of the momentum flux ratio J and the mixing quality on the flame responses, a series of experiments were conducted with varying jet diameters and arrangements while keeping the operating parameters of the test rig constant, as outlined in Table 6.1. The arrangements and configurations will only briefly be summarized below as details can be found in Table 5.1.

In the preliminary CFD design, the baseline configuration Ⓐ exhibited the best mixing quality. Two additional setups with one row of ports were designed to compare their performances with each other. Configuration Ⓑ has a larger jet diameter, which results in a lower momentum flux ratio. Configuration Ⓓ has a smaller jet diameter with a high pressure drop and was designed for a compact test rig arrangement of the primary and secondary zone. The higher crossflow velocities require a higher jet velocity to maintain good mixing quality. However, using those small mixing air jet diameters in the separated arrangement results in a very large momentum flux ratio $J_D \approx 195$, which causes an over-penetration of the jet in the secondary combustion chamber and leads to a significantly different flame shape. The mixing characteristics is worse than in the single row setups Ⓐ and Ⓑ. Configuration Ⓒ is the only two-row setup designed for ideal and fast mixing. The design constraints include the total jet cross-sectional area, which was chosen to be equal to Configuration Ⓐ: $A_{\text{tot,jet,C}} = A_{\text{tot,jet,A}}$. Maintaining the same cross-sectional area allows a comparison of the flame responses with different number of rows.

In Fig. 8.11 the FTFs representing the flame response to upstream velocity fluctuations for the different mixing air jet diameters and arrangements are given. With constant operating parameters of the test rig for each OP, similar amplitudes for the three configurations with moderate momentum flux ratios are observed. Despite the regime where strong jet nozzle coupling occurs, the individual amplitudes of $|FTF_{\text{u,M}}|$ and $|FTF_{\text{u,PMT}}|$ show very good agreement. The lower momentum flux ratio J_B compared to J_A leads to a longer flame and a downstream shift in the center of gravity. With lower convective velocities of Ⓑ, mixing and entrainment times increase. Consequently, the time delay τ_B is larger than τ_A giving a steeper phase response.

For the two-row configuration Ⓒ, good and rapid mixing was observed during the design process, resulting in an almost identical flame

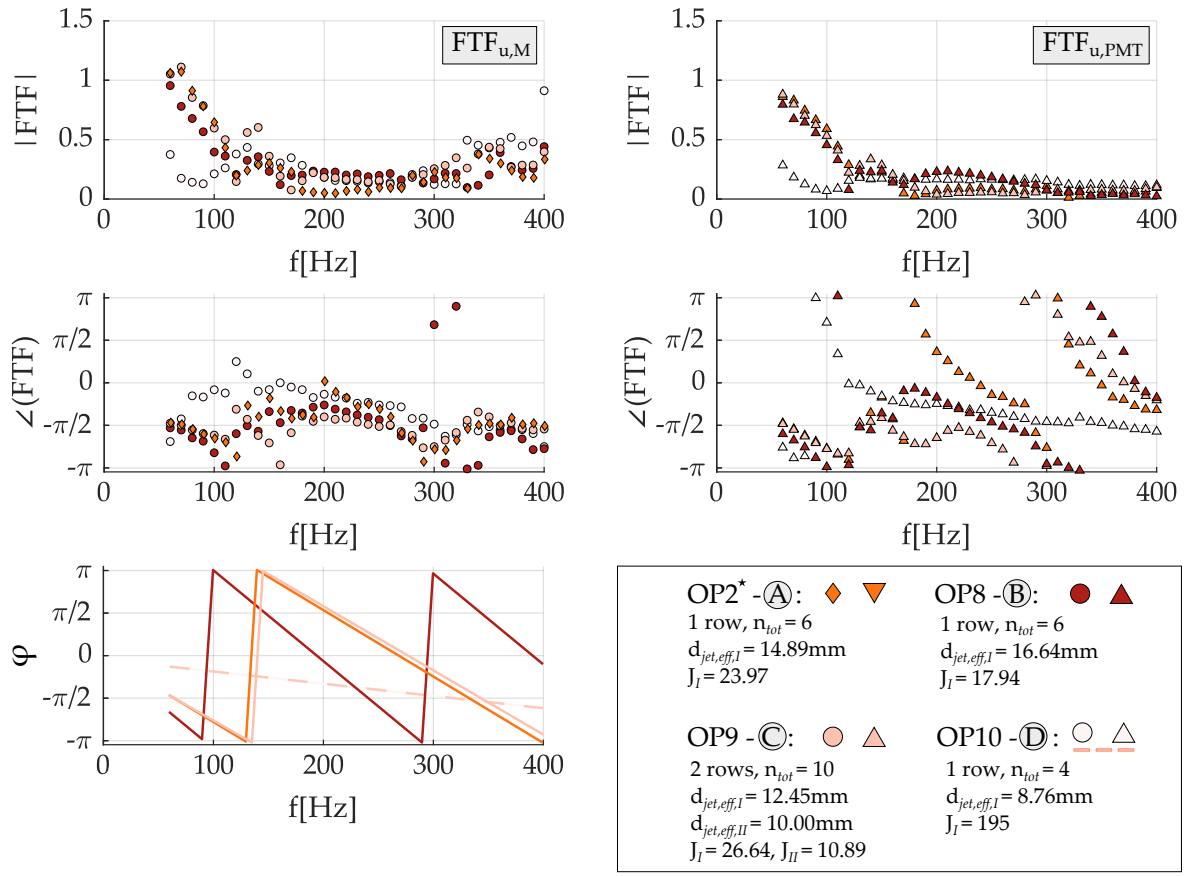

Figure 8.11: Flame transfer function for OP2* in orange and OP8 - 10; ordered by configuration, with OP8-Ⓑ in dark red, OP9-Ⓒ in light orange and OP10-Ⓓ in light skin; left: $FTF_{\mathrm{u,M}}$ in dot markers obtained via the MISO method; right: $FTF_{\mathrm{u,PMT}}$ in triangle markers from PMT measurements; bottom left: phase angle φ given by the time delay model.

position, which the time delay model confirms. Since the convective velocities for configuration Ⓐ and Ⓒ are identical, both time delays are assumed to be equal $\tau_{\mathrm{A}} = \tau_{\mathrm{C}}$. Comparing the corresponding FTF phase response in Fig. 8.11 confirms this, as identical results are found for both configurations.

Configuration Ⓓ has a large momentum flux ratio, resulting in steep and over-penetrating mixing air jets. This causes a change of flame shape

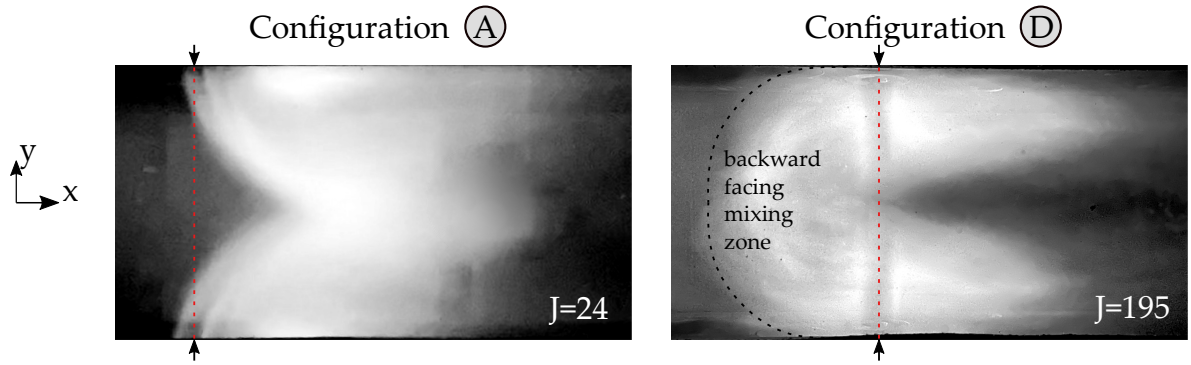

Figure 8.12: Instantaneous flame images taken with a digital camera of OP2*-Ⓐ and OP10-Ⓓ depicting the strong over-penetration of mixing air jets with high momentum flux ratio on the right.

and position compared to the ideal configuration Ⓐ. In Fig. 8.12, the flame images of configurations Ⓐ and Ⓓ demonstrate this difference. Unlike the characteristic JIC shape on the left, the high momentum flux ratio generates a turbulent, backward-facing mixing zone. Combustion occurs upstream of the reference plane, as demonstrated by images and time delay modeling. Due to the high jet and convective velocities paired with a short flame, Configuration Ⓓ is assumed to present much smaller delay times. This is confirmed by the phase response seen on the bottom right of Fig. 8.11 with the white-colored triangle markers and the dashed line in the bottom left graph.

Figure 8.13 presents the flame response to side fluctuations for the operating points OP2* and OP8 - 10. The amplitude and phase response of configuration Ⓐ and the two-row setup Ⓒ exhibit good consistency, similar to that observed for the upstream case $FTF_{\mathrm{u,M}}$. This outcome further underlines the importance of mixture quality and time influencing the flame response. Increasing the jet diameter and, thus, the total cross-sectional area of the jet reduces the mo-

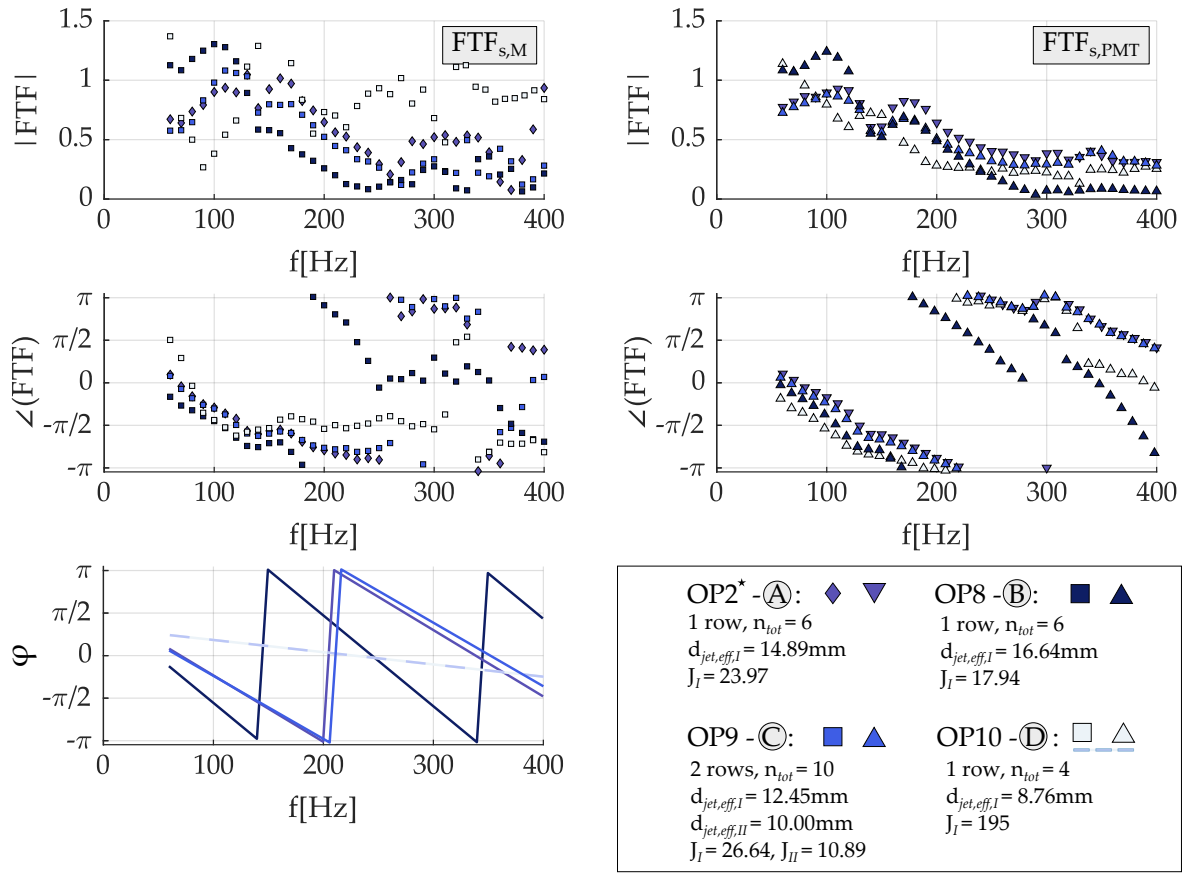

Figure 8.13: Flame transfer function for OP2* in purple and OP8 - 10; ordered by configuration, with OP8-Ⓑ in dark blue, OP9-Ⓒ in light blue and OP10-Ⓓ in white; left: $FTF_{\mathrm{s,M}}$ in square markers obtained via the MISO method; right: $FTF_{\mathrm{s,PMT}}$ in triangle markers extracted from PMT measurements; bottom left: phase angle φ given by the time delay model.

mentum flux ratio J, slows down the mixing, and shifts the flame downstream. With decreasing convective time for configuration Ⓑ, a higher time delay τ_{B} is found again, indicated by the steeper phase drop.

Remarkably, the amplitude response of configuration Ⓑ reveals higher values in the low-frequency range from $f = 60 - 120$ Hz than configuration Ⓐ and Ⓒ. Section 8.1 already emphasized that different JIC configurations may exhibit a different response to jet nozzle cou-

pling on the JIC parameters, such as J and d_{jet}. In this case, lower J configurations have larger u'_{s} and smaller $\bar{u}_{\text{s}}$, resulting in high values of $u'_{\text{s}}/\bar{u}_{\text{s}}$, and leading to the jet nozzle coupled response mechanism that tends to dominate in low J jets, resulting in higher FTF_{s} amplitudes.

In contrast, high J jets in Ⓐ exhibit less jet nozzle coupling and jet flapping than low J jets in Ⓑ. Identical upstream forcing results in much lower values of $u'_{\text{s}}/\bar{u}_{\text{s}}$ in high J cases due to larger mean velocity $\bar{u}_{\text{s}}$. Consequently, increasing the resistive part of the jet injector impedance Z_{jet} and reducing jet nozzle coupling results in smaller normalized induced side velocity fluctuations $u'_{\text{s}}/\bar{u}_{\text{s}}$. On the other hand, the magnitude of $u'_{\text{u}}/\bar{u}_{\text{u}}$ remains essentially unchanged in both configurations, making the upstream fluctuations relatively more important in high J jets than in low J jets.

9 Summary, Conclusion and Future Work

In the scope of this thesis, the lean secondary zone of an RQL combustion chamber was investigated in terms of low-frequency thermoacoustic instabilities. The experiments were conducted in a new atmospheric RQL combustor rig by spatially separating the rich primary zone from the lean burnout zone. Special emphasis was placed on acoustic velocity fluctuations coming from the end of the primary zone and the secondary mixing air jets. This leads to this thesis's primary objective: separating both influences and their effect on the heat release rate in the lean secondary zone and quantifying the behavior with flame transfer functions (FTF). For this purpose, a purely acoustic Multiple-Input-Single-Output (MISO) network system was derived to describe the secondary zone's dynamic behavior. The derived MISO method depicts the dynamic flame response with two individual FTFs depending on the corresponding velocity fluctuations at the end of the primary zone u'_{u} and the mixing air jets u'_{s}. Using two independent measurements - with and without flame - the two FTFs could be determined in a frequency range of $f = 60 - 400\,\mathrm{Hz}$. The resulting acoustic FTF_{u} and FTF_{s} were compared to FTFs based on a hybrid approach with a photomultiplier tube (PMT) using $\mathrm{OH}^{\star}$ chemiluminescence (CL) as measure for the heat release.

The derived MISO method could be verified by identifying two asymptotic cases where either velocity fluctuations could be neglected. First, acoustically stiff mixing air jets ensured no thermoacoustic interaction between the crossflow and the jet, generating no additional flame dynamics. In the second case, regions with upstream velocity fluctuations close to zero were evaluated during a side forcing cycle and used

for verification. The FTFs depending on upstream and side velocity fluctuations showed an excellent agreement with the verification data. This supports the linear superposition approach of the two FTFs in the acoustic MISO method in regions with velocity fluctuations in the linear regime.

Across the entire investigated operating range, the flame of the lean secondary zone reacts to acoustic velocity fluctuations from upstream FTF_u with heat release fluctuations in the low-frequency range of $f = 60 - 180\,\mathrm{Hz}$ and shows a clear low pass behavior. As a reaction to the velocity fluctuations from the side, FTF_s shows a wider, more broadband behavior than FTF_u, with regions of higher amplitudes from $f = 60$ - $200\,\mathrm{Hz}$. At higher frequencies, only the fluctuations from the side contribute a little to the heat release fluctuations.

The following findings emerged when comparing operating points with varying and constant momentum flux ratio J and changing equivalence ratio ϕ_{tot}:

- The FTFs measured with the purely acoustic MISO method and the ones from the hybrid PMT match in terms of their amplitude and phase values very well. However, the observed scattering in FTFs for operating points (OPs) with low levels of heat release was found to be related to minor differences between the underlying cold and hot measurements and the resulting temperature measurement uncertainty. These factors can contribute to higher uncertainties in FTFs for less reactive OPs, which can affect the accuracy of the measurements.
- Considering the flame response of OPs with varying momentum flux ratio J, the results showed that a steeper phase response was observed for highly reactive OPs. In contrast, a lower response was observed for less reactive OPs. The underlying mechanism for this effect was related to the radially inward entrainment of ambient fluid and the equivalent radially outward transport of jet fluid in the

shear layer by shear layer turbulence. The flame length was found to vary with the equivalence ratio. Specifically, a longer flame was observed for highly reactive OPs, while a shorter flame was observed for less reactive ones.

- Furthermore, the convective transport velocity of vortices along the shear layer into the flame was smaller for less reactive OPs due to the lower jet mass fraction and velocity. The time delay τ, which is the time difference between the acoustic excitation and the flame response, decreased towards less reactive OPs due to the more considerable change in relative flame length than convective transport velocity. This observation indicates a flatter phase response for less reactive OPs.

- In contrast, the phase response of FTFs for OPs with constant momentum flux ratio J was found to be independent of the equivalence ratio. This observation can be attributed to the compensation of the change in flame length by constant convective velocities in the jet shear layer, resulting in identical time delays across the operating range. The results of the present study are consistent with the predictions of the time delay model based on entrainment theory, which provides a theoretical framework for understanding the phase response of FTFs. These findings demonstrate the effectiveness of the time delay model in explaining the phase response of FTFs for the secondary zone systems, including those with constant momentum flux ratio J.

A series of experiments were conducted, varying the jet diameters and arrangements while maintaining constant operating parameters. Four different configurations were evaluated, including the baseline configuration, which exhibited the best mixing quality in the preliminary design. Additionally, two configurations with one row of ports were evaluated. One of the configurations had larger jet diameters, while the other had smaller jet diameters than the reference configuration. The two-row setup was designed for ideal and fast mixing, with a total jet

cross-sectional area equal to the baseline configuration. In summary, the following observations were made:

- The jet diameter and the resulting momentum flux ratio J were found to impact the flame shape, position, time delay, and phase response. Configurations with a larger diameter, thus lower J, resulted in longer flames and larger time delays with steeper phase responses. In contrast, configurations with a smaller jet diameter and high J led to shorter flames and minimal delay times.
- Different JIC configurations exhibited different acoustic responses to jet nozzle coupling on JIC parameters, such as d_{jet} and J, resulting in a different flame response to velocity fluctuations. In larger d_{jet} and low J configurations, higher values of normalized induced side velocity fluctuations were observed, resulting in higher amplitude responses in the low-frequency range compared to smaller d_{jet} and high J configurations. Conversely, smaller normalized induced side velocity fluctuations were observed in smaller d_{jet} and high J configurations, resulting in a lower amplitude response in the low-frequency range.

Considering the heat release distribution in both stages of typical RQL combustors, the secondary zone contributes only approximately $10 - 25\%$ to the total heat release, with most of the heat being released in the primary zone. The influence of the secondary zone on the overall system dynamics can be weighted according to its heat release rate relative to the primary zone, which leads to a relatively minor contribution of the secondary zone to the combined system dynamics.

The presented study poses the question regarding the extent to which the findings can be applied to a combined compact RQL combustor. In the initial stage, it is necessary to characterize the individual dynamic response of the primary zone. Following this, the compact arrangement can be examined using the MISO method derived in this thesis. Although the MISO method yielded good agreement with the $OH^{\star}$

chemiluminescence data in the case of the inverse diffusion flame, the latter is not a suitable representative for heat release fluctuations during non-premixed liquid fuel combustion. To verify the MISO method in the compact arrangement, the work conducted by Vogel et al. [99, 100] could offer an alternative approach. A comparison between separate measurements of the individual flame dynamics of both zones and the compact arrangement would reveal the contributions of the individual zones to the overall dynamic behavior.

The experimental setup employed in this research involved an atmospheric RQL facility, which is complex, and the lean secondary zone's setup is somewhat academic. In actual engine test rigs, measuring the acoustic field inside the secondary air ports is challenging. However, an analytical formulation of the mixing air jets impedance Z_{jet}, based on the geometrical parameters, could be used as an alternative. This would establish a relationship between the crossflow fluctuations of pressure and velocity inside the combustor and those inside the jets. With knowledge of the jet nozzle coupling, the flame dynamics response could be determined.

Appendix: Burner Flame Scattering Matrix from MISO Approach

$$\begin{bmatrix} \hat{g}_\mathrm{u} \\ \hat{g}_\mathrm{s} \\ \hat{f}_\mathrm{d} \end{bmatrix} = \mathbf{BFSM}_{3\mathrm{x}3}^{MISO} \begin{pmatrix} FTF_{\mathrm{u,M}}, FTF_{\mathrm{s,M}}, \dots \\ \omega, \zeta, \xi, \chi, R_\mathrm{n}, T_\mathrm{nm}, \dots \\ M_\mathrm{i}, \gamma, \bar{u}_\mathrm{i}, \bar{u}_\mathrm{s}, \bar{u}_\mathrm{u} \end{pmatrix} \begin{bmatrix} \hat{f}_\mathrm{u} \\ \hat{f}_\mathrm{s} \\ \hat{g}_\mathrm{d} \end{bmatrix}$$

$$\begin{aligned}
\mathbf{BFSM}_{11}^{MISO} = \; & \chi(\zeta FTF_{\mathrm{u,M}} T_{\mathrm{i,u}} \bar{u}_\mathrm{s} + \zeta FTF_{\mathrm{s,M}} R_\mathrm{u} T_{\mathrm{i,s}} \bar{u}_\mathrm{u} - \zeta FTF_{\mathrm{s,M}} \dots \\
& T_{\mathrm{i,u}} T_{\mathrm{u,s}} \bar{u}_\mathrm{u}) \bar{u}_\mathrm{i} + \chi(R_\mathrm{u} \bar{u}_\mathrm{s} \bar{u}_\mathrm{u} + \xi R_\mathrm{u} \bar{u}_\mathrm{s} \bar{u}_\mathrm{u} - R_\mathrm{i} R_\mathrm{u} \bar{u}_\mathrm{s} \bar{u}_\mathrm{u} + \dots \\
& T_{\mathrm{i,u}} T_{\mathrm{u,i}} \bar{u}_\mathrm{s} \bar{u}_\mathrm{u} + \xi R_\mathrm{i} R_\mathrm{u} \bar{u}_\mathrm{s} \bar{u}_\mathrm{u} - \xi T_{\mathrm{i,u}} T_{\mathrm{u,i}} \bar{u}_\mathrm{s} \bar{u}_\mathrm{u} + \dots \\
& \zeta M_\mathrm{i} R_\mathrm{u} \gamma \bar{u}_\mathrm{s} \bar{u}_\mathrm{u} + \zeta M_\mathrm{i} R_\mathrm{i} R_\mathrm{u} \gamma \bar{u}_\mathrm{s} \bar{u}_\mathrm{u} - \zeta M_\mathrm{i} T_{\mathrm{i,u}} T_{\mathrm{u,i}} \gamma \bar{u}_\mathrm{s} \bar{u}_\mathrm{u})
\end{aligned}$$

$$\begin{aligned}
\mathbf{BFSM}_{12}^{MISO} = \; & \chi(\zeta FTF_{\mathrm{s,M}} T_{\mathrm{i,u}} \bar{u}_\mathrm{u} - \zeta FTF_{\mathrm{s,M}} R_\mathrm{s} T_{\mathrm{i,u}} \bar{u}_\mathrm{u} + \zeta FTF_{\mathrm{s,M}} \dots \\
& T_{\mathrm{i,s}} T_{\mathrm{s,u}} \bar{u}_\mathrm{u}) \bar{u}_\mathrm{i} + \chi(T_{\mathrm{s,u}} \bar{u}_\mathrm{s} \bar{u}_\mathrm{u} + \xi T_{\mathrm{s,u}} \bar{u}_\mathrm{s} \bar{u}_\mathrm{u} - R_\mathrm{i} T_{\mathrm{s,u}} \bar{u}_\mathrm{s} \bar{u}_\mathrm{u} + \dots \\
& T_{\mathrm{i,u}} T_{\mathrm{s,i}} \bar{u}_\mathrm{s} \bar{u}_\mathrm{u} + \xi R_\mathrm{i} T_{\mathrm{s,u}} \bar{u}_\mathrm{s} \bar{u}_\mathrm{u} - \xi T_{\mathrm{i,u}} T_{\mathrm{s,i}} \bar{u}_\mathrm{s} \bar{u}_\mathrm{u} + \dots \\
& \zeta M_\mathrm{i} T_{\mathrm{s,u}} \gamma \bar{u}_\mathrm{s} \bar{u}_\mathrm{u} + \zeta M_\mathrm{i} R_\mathrm{i} T_{\mathrm{s,u}} \gamma \bar{u}_\mathrm{s} \bar{u}_\mathrm{u} - \zeta M_\mathrm{i} T_{\mathrm{i,u}} T_{\mathrm{s,i}} \gamma \bar{u}_\mathrm{s} \bar{u}_\mathrm{u})
\end{aligned}$$

$$\mathbf{BFSM}_{13}^{MISO} = 2\chi T_{\mathrm{i,u}} \bar{u}_\mathrm{s} \bar{u}_\mathrm{u}$$

$$
\begin{aligned}
\mathbf{BFSM}_{21}^{MISO} = \; & \chi(\zeta FTF_{\mathrm{u,M}}T_{\mathrm{i,s}}\bar{u}_{\mathrm{s}} - \zeta FTF_{\mathrm{u,M}}R_{\mathrm{u}}T_{\mathrm{i,s}}\bar{u}_{\mathrm{s}} + \zeta FTF_{\mathrm{u,M}} \ldots \\
& T_{\mathrm{i,u}}T_{\mathrm{u,s}}\bar{u}_{\mathrm{s}})\bar{u}_{\mathrm{i}} + \chi(T_{\mathrm{u,s}}\bar{u}_{\mathrm{s}}\bar{u}_{\mathrm{u}} + \xi T_{\mathrm{u,s}}\bar{u}_{\mathrm{s}}\bar{u}_{\mathrm{u}} - R_{\mathrm{i}}T_{\mathrm{u,s}}\bar{u}_{\mathrm{s}}\bar{u}_{\mathrm{u}} + \ldots \\
& T_{\mathrm{i,s}}T_{\mathrm{u,i}}\bar{u}_{\mathrm{s}}\bar{u}_{\mathrm{u}} + \xi R_{\mathrm{i}}T_{\mathrm{u,s}}\bar{u}_{\mathrm{s}}\bar{u}_{\mathrm{u}} - \xi T_{\mathrm{i,s}}T_{\mathrm{u,i}}\bar{u}_{\mathrm{s}}\bar{u}_{\mathrm{u}} + \ldots \\
& \zeta M_{\mathrm{i}}T_{\mathrm{u,s}}\gamma\bar{u}_{\mathrm{s}}\bar{u}_{\mathrm{u}} + \zeta M_{\mathrm{i}}R_{\mathrm{i}}T_{\mathrm{u,s}}\gamma\bar{u}_{\mathrm{s}}\bar{u}_{\mathrm{u}} - \zeta M_{\mathrm{i}}T_{\mathrm{i,s}}T_{\mathrm{u,i}}\gamma\bar{u}_{\mathrm{s}}\bar{u}_{\mathrm{u}})
\end{aligned}
$$

$$
\begin{aligned}
\mathbf{BFSM}_{22}^{MISO} = \; & \chi(\zeta FTF_{\mathrm{s,M}}T_{\mathrm{i,s}}\bar{u}_{\mathrm{u}} + \zeta FTF_{\mathrm{u,M}}R_{\mathrm{s}}T_{\mathrm{i,u}}\bar{u}_{\mathrm{s}} - \zeta FTF_{\mathrm{u,M}} \ldots \\
& T_{\mathrm{i,s}}T_{\mathrm{s,u}}\bar{u}_{\mathrm{s}})\bar{u}_{\mathrm{i}} + \chi(R_{\mathrm{s}}\bar{u}_{\mathrm{s}}\bar{u}_{\mathrm{u}} + \xi R_{\mathrm{s}}\bar{u}_{\mathrm{s}}\bar{u}_{\mathrm{u}} - R_{\mathrm{i}}R_{\mathrm{s}}\bar{u}_{\mathrm{s}}\bar{u}_{\mathrm{u}} + \ldots \\
& T_{\mathrm{i,s}}T_{\mathrm{s,i}}\bar{u}_{\mathrm{s}}\bar{u}_{\mathrm{u}} + \xi R_{\mathrm{i}}R_{\mathrm{s}}\bar{u}_{\mathrm{s}}\bar{u}_{\mathrm{u}} - \xi T_{\mathrm{i,s}}T_{\mathrm{s,i}}\bar{u}_{\mathrm{s}}\bar{u}_{\mathrm{u}} + \ldots \\
& \zeta M_{\mathrm{i}}R_{\mathrm{s}}\gamma\bar{u}_{\mathrm{s}}\bar{u}_{\mathrm{u}} + \zeta M_{\mathrm{i}}R_{\mathrm{i}}R_{\mathrm{s}}\gamma\bar{u}_{\mathrm{s}}\bar{u}_{\mathrm{u}} - \zeta M_{\mathrm{i}}T_{\mathrm{i,s}}T_{\mathrm{s,i}}\gamma\bar{u}_{\mathrm{s}}\bar{u}_{\mathrm{u}})
\end{aligned}
$$

$$
\mathbf{BFSM}_{23}^{MISO} = 2\chi T_{\mathrm{i,s}}\bar{u}_{\mathrm{s}}\bar{u}_{\mathrm{u}}
$$

$$
\begin{aligned}
\mathbf{BFSM}_{31}^{MISO} = \; & \chi(\zeta\xi FTF_{\mathrm{u,M}}\bar{u}_{\mathrm{s}} + \zeta\xi FTF_{\mathrm{u,M}}R_{\mathrm{i}}\bar{u}_{\mathrm{s}} - \zeta\xi FTF_{\mathrm{u,M}}R_{\mathrm{u}}\bar{u}_{\mathrm{s}} - \ldots \\
& \zeta\xi FTF_{\mathrm{s,M}}T_{\mathrm{u,s}}\bar{u}_{\mathrm{u}} - \zeta\xi FTF_{\mathrm{u,M}}R_{\mathrm{i}}R_{\mathrm{u}}\bar{u}_{\mathrm{s}} - \ldots \\
& \zeta\xi FTF_{\mathrm{s,M}}R_{\mathrm{i}}T_{\mathrm{u,s}}\bar{u}_{\mathrm{u}} + \zeta\xi FTF_{\mathrm{u,M}}T_{\mathrm{i,u}}T_{\mathrm{u,i}}\bar{u}_{\mathrm{s}} + \ldots \\
& \zeta\xi FTF_{\mathrm{s,M}}T_{\mathrm{i,s}}T_{\mathrm{u,i}}\bar{u}_{\mathrm{u}})\bar{u}_{\mathrm{i}} + 2\xi\chi T_{\mathrm{u,i}}\bar{u}_{\mathrm{s}}\bar{u}_{\mathrm{u}}
\end{aligned}
$$

$$
\begin{aligned}
\mathbf{BFSM}_{32}^{MISO} = \; & \bar{u}_{\mathrm{u}} + \zeta\xi FTF_{\mathrm{s,M}}R_{\mathrm{i}}\bar{u}_{\mathrm{u}} - \zeta\xi FTF_{\mathrm{s,M}}R_{\mathrm{s}}\bar{u}_{\mathrm{u}} - \zeta\xi FTF_{\mathrm{u,M}}T_{\mathrm{s,u}}\bar{u}_{\mathrm{s}} - \ldots \\
& \zeta\xi FTF_{\mathrm{s,M}}R_{\mathrm{i}}R_{\mathrm{s}}\bar{u}_{\mathrm{u}} - \zeta\xi FTF_{\mathrm{u,M}}R_{\mathrm{i}}T_{\mathrm{s,u}}\bar{u}_{\mathrm{s}} + \ldots \\
& \zeta\xi FTF_{\mathrm{u,M}}T_{\mathrm{i,u}}T_{\mathrm{s,i}}\bar{u}_{\mathrm{s}} + \zeta\xi FTF_{\mathrm{s,M}}T_{\mathrm{i,s}}T_{\mathrm{s,i}}\bar{u}_{\mathrm{u}})\bar{u}_{\mathrm{i}} + 2\xi\chi T_{\mathrm{s,i}}\bar{u}_{\mathrm{s}}\bar{u}_{\mathrm{u}}
\end{aligned}
$$

$$
\begin{aligned}
\mathbf{BFSM}_{33}^{MISO} = \; & \chi(\zeta\xi FTF_{\mathrm{s,M}}, (-\chi(\zeta FTF_{\mathrm{u,M}}T_{\mathrm{i,u}}\bar{u}_{\mathrm{s}} + \zeta FTF_{\mathrm{s,M}}T_{\mathrm{i,s}}\bar{u}_{\mathrm{u}}))\bar{u}_{\mathrm{i}} - \ldots \\
& \chi(\bar{u}_{\mathrm{s}}\bar{u}_{\mathrm{u}} - \xi\bar{u}_{\mathrm{s}}\bar{u}_{\mathrm{u}} - R_{\mathrm{i}}\bar{u}_{\mathrm{s}}\bar{u}_{\mathrm{u}} - \xi R_{\mathrm{i}}\bar{u}_{\mathrm{s}}\bar{u}_{\mathrm{u}} + \zeta M_{\mathrm{i}}\gamma\bar{u}_{\mathrm{s}}\bar{u}_{\mathrm{u}} + \ldots \\
& \zeta M_{\mathrm{i}}R_{\mathrm{i}}\gamma\bar{u}_{\mathrm{s}}\bar{u}_{\mathrm{u}}) \\
\zeta \triangleq \; & \left(\tfrac{T_{\mathrm{d}}}{T_{\mathrm{i}}} - 1\right) \\
\xi \triangleq \; & \tfrac{(\rho c)_{\mathrm{i}}}{(\rho c)_{\mathrm{d}}} \\
\chi \triangleq \; & 1/(\bar{u}_{\mathrm{s}}\bar{u}_{\mathrm{u}} + \xi\bar{u}_{\mathrm{s}}\bar{u}_{\mathrm{u}} - R_{\mathrm{i}}\bar{u}_{\mathrm{s}}\bar{u}_{\mathrm{u}} + \xi R_{\mathrm{i}}\bar{u}_{\mathrm{s}}\bar{u}_{\mathrm{u}} + \ldots \\
& \zeta FTF_{\mathrm{u,M}}T_{\mathrm{i,u}}\bar{u}_{\mathrm{i}}\bar{u}_{\mathrm{s}} + \zeta FTF_{\mathrm{s,M}}T_{\mathrm{i,s}}\bar{u}_{\mathrm{i}}\bar{u}_{\mathrm{u}} + \zeta M_{\mathrm{i}}\gamma\bar{u}_{\mathrm{s}}\bar{u}_{\mathrm{u}} + \ldots \\
& \zeta M_{\mathrm{i}}R_{\mathrm{i}}\gamma\bar{u}_{\mathrm{s}}\bar{u}_{\mathrm{u}})
\end{aligned}
$$

Previous Publications

Significant parts of this Ph.D. thesis have been published by the author beforehand in conference proceedings and journal papers. All these publications are registered according to the valid doctoral regulations and are listed below. However, not all of them are quoted explicitly everywhere as they are part of this present work being official documents. Whether these publications were referenced, depended on maintaining comprehensibility and providing all necessary context.

1. Renner, J., March, M., Do, T. A., Merk, M., Hirsch, C., and Sattelmayer, T., 2023. Flame transfer functions of the lean burnout zone of an RQL combustion chamber - Dynamic response to primary zone and mixing port velocity fluctuations. *International Journal of Spray and Combustion Dynamics, 0*(0), Online First.

2. Renner, J., March, M., Hirsch, C., and Sattelmayer, T., 2022. Flame dynamics in the lean burnout zone of an RQL combustion chamber-response to primary zone velocity fluctuations. *International Journal of Spray and Combustion Dynamics, 14*(3-4), pp. 238–250.

3. March, M., Renner, J., Hirsch, C., and Sattelmayer, T., 2021. Design and validation of a novel test-rig for RQL flame dynamics studies. In *Proceedings of the ASME Turbo Expo*, Virtual, GT2021-58602.

Supervised Student Theses

Associated with this Ph.D. thesis, a number of student theses were supervised by the author of the present work. These theses were created and written at the Lehrstuhl für Thermodynamik, Technische Universität München in the years 2019 to 2022 under the close supervision of the author. Parts of these supervised theses may be incorporated into the present thesis. The author would like to express his gratitude to all formerly supervised students for their support of this research project.

Name	Thesis title, type, submission date
Tobias Jeron	Experimentelle Untersuchung der akustischen Anregung von Sekundärluftjets in RQL-Brennkammern, Bachelor's Thesis, June 25th, 2019.
Axel Schmid	Numerisches Setup zur Anregung und Auswertung der mageren Zonen eines RQL Brennkammer Prüstandes, Semester Thesis, July 29th, 2019.
Jan-Andre Rosenkranz	Numerische Optimierung von Mischung und Verbrennung der mageren Zone eines RQL Brennkammer Prüfstandes, Master's Thesis, November 27th, 2019.
Magnus von Reinersdorff	Charakterisierung der mager gestuften Verbrennung an einem RQL Brennkammer Prüfstand für verschiedene Brennstoffe, Semester Thesis, June 25th, 2021.
Thuy An Do	Aktive Beeinflussung der akustischen Randbedingungen in einem RQL Brennkammerprüfstand, Semester Thesis, July 29th, 2021.
Thuy An Do	Flame Dynamics in RQL Combustion Chambers - A modeling approach to characterize the dilution zone, Master's Thesis, August 1st, 2022.
Dominik König	Flame Dynamics in RQL Combustion Chambers - A Flame Structure Analysis of the Dilution Zone with Proper Orthogonal Decomposition (POD), Master's Thesis, December 1st, 2022.

Bibliography

[1] European Commission, 2011. Flightpath 2050: Europe's vision for aviation. *Advisory Council for Aeronautics Research in Europe.*

[2] Yin, F., and Rao, A. G., 2020. A review of gas turbine engine with inter-stage turbine burner. *Progress in Aerospace Sciences, 121*, p. 100695.

[3] Samuelsen, G. S., Brouwer, J., Vardakas, M. A., and Holdeman, J. D., 2013. Experimental and modeling investigation of the effect of air preheat on the formation of NOx in an RQl combustor. *Heat Mass Transfer, 49*(2), pp. 219-231.

[4] Karagozian, A. R., 2010. Transverse jets and their control. *Progress in Energy and Combustion Science, 36*(5), pp. 531-553.

[5] Karagozian, A. R., 2014. The jet in crossflow. *Physics of Fluids, 26*(10), p. 101303.

[6] Mahesh, K., 2013. The interaction of jets with crossflow. *Annual Review of Fluid Mechanics, 45*(1), pp. 379-407.

[7] Holdeman, J. D., 2001. *Low emissions RQL flametube combustor component test results*. Report No. NASA/TM-2001-210678.

[8] Rosfjord, T. J., Padget, F. C., and Tacina, R. R., 2001. *Experimental assessment of the emissions control potential of a rich/quench/lean combustor for high speed civil transport aircraft engines*. Report No. NASA/TM-2001-12572.

[9] Eckstein, J., Freitag, E., Hirsch, C., and Sattelmayer, T., 2006. Experimental study on the role of entropy waves in low-frequency

oscillations in a RQL combustor. *Journal of Engineering for Gas Turbines and Power, 128*(2), pp. 264-270.

[10] Cai, J., Ichihashi, F., Mohammad, B., Tambe, S., Kao, Y.-H., and Jeng, S.-M., 2010. Gas turbine single annular combustor sector: Combustion dynamics. In *48th AIAA Aerospace Sciences Meeting and Exhibit*. Orlando, Florida, USA, AIAA 2010-21.

[11] Wilde, B. R., 2014. *Dynamics of variable density ratio reacting jets in unsteady, vitiated crossflow*. PhD Thesis, Georgia Institute of Technology, Atlanta, Georgia, USA.

[12] Nair, V., Wilde, B., Emerson, B., and Lieuwen, T., 2019. Shear layer dynamics in a reacting jet in crossflow. *Proceedings of the Combustion Institute, 37*(4), pp. 5173-5180.

[13] Holdeman, J. D., 1993. Mixing of multiple jets with a confined subsonic crossflow. *Progress in Energy and Combustion Science, 19*(1), pp. 31-70.

[14] Margason, R. J., 1993. Fifty years of jet in cross flow research. In *AGARD*.

[15] Smith, S. H., and Mungal, M. G., 1998. Mixing, structure and scaling of the jet in crossflow. *Journal of Fluid Mechanics, 357*, pp. 83-122.

[16] Liscinsky, D. S., 1993. Experimental investigation of crossflow jet mixing in a rectangular duct. In *29th Joint Propulsion Conference and Exhibit*. Monterey, California, USA.

[17] Lefebvre, A. H., and Ballal, D. R., 2010. *Gas turbine combustion: Alternative fuels and emissions*. Taylor & Francis, Boca Raton.

[18] Fric, T. F., and Roshko, A., 1994. Vortical structure in the wake of a transverse jet. *Journal of Fluid Mechanics, 279*, pp. 1-47.

[19] Meyer, K. E., Pedersen, J. M., and Özcan, O., 2007. A turbulent jet in crossflow analysed with proper orthogonal decomposition. *Journal of Fluid Mechanics, 583*, pp. 199-227.

[20] Poinsot, T. J., Trouve, A. C., Veynante, D. P., Candel, S. M., and Esposito, E. J., 1987. Vortex-driven acoustically coupled combustion instabilities. *Journal of Fluid Mechanics, 177*, pp. 265-292.

[21] Kelso, R. M., Lim, T. T., and Perry, A. E., 1996. An experimental study of round jets in cross-flow. *Journal of Fluid Mechanics, 306*, pp. 111-144.

[22] New, T. H., Lim, T. T., and Luo, S. C., 2006. Effects of jet velocity profiles on a round jet in cross-flow. *Experiments in Fluids, 40*(6), pp. 859-875.

[23] Huerre, P., and Monkewitz, P. A., 1990. Local and global instabilities in spatially developing flows. *Annual Review of Fluid Mechanics, 22*(1), pp. 473-537.

[24] Megerian, S., Davitian, J., de B. Alves, L. S., and Karagozian, A. R., 2007. Transverse-jet shear-layer instabilities. Part 1. Experimental studies. *Journal of Fluid Mechanics, 593*, pp. 93-129.

[25] Davitian, J., Hendrickson, C., Getsinger, D., M'Closkey, R. T., and Karagozian, A. R., 2010. Strategic control of transverse jet shear layer instabilities. *AIAA Journal, 48*(9), pp. 2145-2156.

[26] Bagheri, S., Schlatter, P., Schmid, P. J., and Henningson, D. S., 2009. Global stability of a jet in crossflow. *Journal of Fluid Mechanics, 624*, pp. 33-44.

[27] Getsinger, D. R., Hendrickson, C., and Karagozian, A. R., 2012. Shear layer instabilities in low-density transverse jets. *Experiments in Fluids, 53*(3), pp. 783-801.

[28] Emerson, B., O'Connor, J., Juniper, M., and Lieuwen, T., 2012. Density ratio effects on reacting bluff-body flow field characteristics. *Journal of Fluid Mechanics, 706*, pp. 219-250.

[29] Juniper, M. P., Li, L. K., and Nichols, J. W., 2009. Forcing of self-excited round jet diffusion flames. *Proceedings of the Combustion Institute, 32*(1), pp. 1191-1198.

[30] Mahalingam, S., Cantwell, B. J., and Ferziger, J. H., 1991. Stability of low-speed reacting flows. *Physics of Fluids, 3*(6), pp. 1533-1543.

[31] Schmitt, D., Kolb, M., Weinzierl, J., Hirsch, C., and Sattelmayer, T., 2013. Ignition and flame stabilization of a premixed jet in hot crossflow. In *Proceedings of the ASME Turbo Expo*. San Antonio, Texas, USA, GT2013-94763.

[32] Johari, H., Pacheco-Tougas, M., and Hermanson, J. C., 1999. Penetration and mixing of fully modulated turbulent jets in crossflow. *AIAA Journal, 37*(7), pp. 842-850.

[33] Eroglu, A., and Breidenthal, R. E., 2001. Structure, penetration, and mixing of pulsed jets in crossflow. *AIAA Journal, 39*(3), pp. 417-423.

[34] Narayanan, S., Barooah, P., and Cohen, J. M., 2003. Dynamics and control of an isolated jet in crossflow. *AIAA Journal, 41*(12), pp. 2316-2330.

[35] Johari, H., 2006. Scaling of fully pulsed jets in crossflow. *AIAA Journal, 44*(11), pp. 2719-2725.

[36] Marr, K. C., Clemens, N. T., and Ezekoye, O. A., 2012. Mixing characteristics and emissions of strongly-forced non-premixed and partially-premixed jet flames in crossflow. *Combustion and Flame, 159*(2), pp. 707-721.

[37] Kremer, D. M., am Ende, M. T., Mustakis, J. G., and am Ende, D. J., 2007. A numerical investigation of a jet in an oscillating crossflow. *Physics of Fluids, 19*(9), p. 095103.

[38] Zhang, L., and Yang, V., 2017. Flow dynamics and mixing of a transverse jet in crossflow–part ii: Oscillating crossflow. *Journal of Engineering for Gas Turbines and Power, 139*(8), pp. 269-277.

[39] Nair, V., Sirignano, M., Emerson, B. L., and Lieuwen, T. C., 2022. Combustion and flame position impacts on shear layer dynamics in a reacting jet in cross-flow. *Journal of Fluid Mechanics, 942*, pp. 219-250.

[40] Hauser, M., Lorenz, M., and Sattelmayer, T., 2011. Influence of transversal acoustic excitation of the burner approach flow on the flame structure. *Journal of Engineering for Gas Turbines and Power, 133*(4), pp. 569-577.

[41] Hofmeister, T. E., 2021. *Influence of acoustically induced vorticity perturbations on high-frequency thermoacoustic instabilities in gas turbine combustors.* PhD Thesis, Technical University of Munich, Munich.

[42] Lieuwen, T. C., 2021. *Unsteady combustor physics*. Cambridge University Press, Cambridge.

[43] Dowling, A. P., 1995. The calculation of thermoacoustic oscillations. *Journal of Sound and Vibration, 180*(4), pp. 557-581.

[44] Rienstra, S. W., and Hirschberg, A., 2004. *An introduction to acoustics*. Eindhoven University of Technology, Eindhoven.

[45] Chu, B.-T., and Kovásznay, L. S. G., 1958. Non-linear interactions in a viscous heat-conducting compressible gas. *Journal of Fluid Mechanics, 3*(5), pp. 494-514.

[46] Ehrenfried, K., 2004. *Strömungsakustik: Skript zur Volesung*. Mensch-und-Buch Verlag, Berlin.

[47] Bothien, M. R., 2009. *Impedance Tuning: A Method for Active Control of the Acoustic Boundary Conditions of Combustion Test Rigs.* PhD Thesis, Technical University of Berlin, Berlin.

[48] Foellinger, O., Doerrscheidt, F., and Klittich, M., 1978. *Regelungstechnik. Einführung in die Methoden und ihre Anwendung*. Elitera Verlag, Berlin.

[49] Munjal, M. L., 1987. *Acoustics of ducts and mufflers: With application to exhaust and ventilation system design*. John Wiley & Sons, New York.

[50] Munjal, M. L., and Doige, AG, 1990. Theory of a two source-location method for direct experimental evaluation of the four-pole

parameters of an aeroacoustic element. *Journal of Sound and Vibration, 141*(2), pp. 323-333.

[51] Fischer, A., 2004. *Hybride, thermoakustische Charakterisierung von Drallbrennern.* PhD Thesis, Technical University of Munich, Munich.

[52] Alemela, P. R., 2009. *Measurement and scaling of acoustic transfer matrices of premixed swirl flames.* PhD Thesis, Technical University of Munich, Munich.

[53] Polifke, W., van der Hoek, J., and Verhaar, B., 1997. *Everything you always wanted to know about f and g*. Technical University of Munich, Munich.

[54] Bade, S., 2014. *Messung und Modellierung der thermoakustischen Eigenschaften eines modularen Brennersystems für vorgemischte Drallflammen.* PhD Thesis, Technical University of Munich, Munich.

[55] Zahn, M., 2018. *Vorhersage und Optimierung des thermoakustischen Stabilitätsverhaltens von Ringbrennkammern unter Einsatz passiver Dämpfer.* PhD Thesis, Technical University of Munich, Munich.

[56] Freitag, E., 2009. *On the measurement and modelling of flame transfer functions at elevated pressure.* PhD Thesis, Technical University of Munich, Munich.

[57] Hauser, M., 2014. *Zum Einfluss transversaler akustischer Anregung auf die Dynamik turbulenter vorgemischter Drallflammen.* PhD Thesis, Technical University of Munich, Munich.

[58] Polifke, W., and Lawn, C., 2007. On the low-frequency limit of flame transfer functions. *Combustion and Flame, 151*(3), pp. 437-451.

[59] Lieuwen, T., and Zinn, B. T., eds., 1998. The role of equivalence ratio oscillations in driving combustion instabilities in low NOx gas

turbines. *Symposium (International) on Combustion, 27*(2), pp. 1809-1816.

[60] Schuermans, B., Bellucci, V., Guethe, F., Meili, F., Flohr, P., and Paschereit, C. O., 2004. A detailed analysis of thermoacoustic interaction mechanisms in a turbulent premixed flame. In *Proceedings of the ASME Turbo Expo*. Vienna, Austria, GT2004-53831.

[61] Chu, B.-T., 1953. On the generation of pressure waves at a plane flame front. *Symposium (International) on Combustion, 4*(1), pp. 603-612.

[62] Schuermans, B., Polifke, W., and Paschereit, C. O., eds., 1999. Modeling transfer matrices of premixed flames and comparison with experimental results. In *Proceedings of the ASME Turbo Expo*. Indianapolis, Indiana, USA, 99-GT-132.

[63] Polifke, W., Paschereit, C. O., and Döbbeling, K., 2001. Constructive and destructive interference of acoustic and entropy waves in a premixed combustor with a choked exit. *International Journal of Acoustics and Vibration, 6*(3), pp. 135-146.

[64] Strobio Chen, L., Steinbacher, T., Silva, C., and Polifke, W., 2016. On generation of entropy waves by a premixed flame. In *Proceedings of the ASME Turbo Expo*. Seoul, South Korea, GT2016-57026.

[65] Gant, F., Cuquel, A., and Bothien, M. R., 2022. Autoignition flame transfer matrix: Analytical model versus large eddy simulations. *International Journal of Spray and Combustion Dynamics, 14*(1-2), pp. 72-81.

[66] Stadlmair, N. V., 2018. *Influence of water injection on the thermoacoustic stability of a lean-premixed combustor.* PhD Thesis, Technical University of Munich, Munich.

[67] Lavrentjev, J., and Åbom, M., 1996. Characterization of fluid machines as acoustic multi-port sources. *Journal of Sound and Vibration, 197*(1), pp. 1-16.

[68] Karlsson, M., and Åbom, M., 2010. Aeroacoustics of T-junctions - an experimental investigation. *Journal of Sound and Vibration, 329*(10), pp. 1793-1808.

[69] Holmberg, A., Karlsson, M., and Åbom, M., 2015. Aeroacoustics of rectangular T-junctions subject to combined grazing and bias flows - an experimental investigation. *Journal of Sound and Vibration, 340*, pp. 152-166.

[70] Bade, S., Wagner, M., Hirsch, C., Sattelmayer, T., and Schuermans, B., 2014. Influence of fuel-air mixing on flame dynamics of premixed swirl burners. In *Proceedings of the ASME Turbo Expo*. Düsseldorf, Germany, GT2014-25381.

[71] Stadlmair, N., and Sattelmayer, T., 2016. Measurement and analysis of flame transfer functions in a lean-premixed, swirl-stabilized combustor with water injection. In *54th AIAA Aerospace Sciences Meeting and Exhibit*. San Diego, California, USA, AIAA 2016-1157.

[72] de Rosa, A. J., Peluso, S. J., Quay, B. D., and Santavicca, D. A., 2016. The effect of confinement on the structure and dynamic response of lean-premixed, swirl-stabilized flames. *Journal of Engineering for Gas Turbines and Power, 138*(6), p. 061507.

[73] Kaufmann, J., Vogel, M., Papenbrock, J., and Sattelmayer, T., 2022. Comparison of the fame dynamics of a premixed dual fuel burner for kerosene and natural gas. *International Journal of Spray and Combustion Dynamics, 14*(1-2), pp. 176-185.

[74] Bothien, M., Lauper, D., Yang, Y., and Scarpato, A., 2019. Reconstruction and analysis of the acoustic transfer matrix of a reheat flame from large-eddy simulations. *Journal of Engineering for Gas Turbines and Power, 141*(2), p. 021018.

[75] Goldberg, D. E., 1989. *Genetic algorithms in search, optimization, and machine learning*. Addison-Wesley Longman Publishing, Boston.

[76] Hasselbrink, E. F., and Mungal, M. G., 2001. Transverse jets and jet flames. Part 1. Scaling laws for strong transverse jets. *Journal of Fluid Mechanics, 443*, pp. 1-25.

[77] Lawn, C. J., 2009. Lifted flames on fuel jets in co-flowing air. *Progress in Energy and Combustion Science, 35*(1), pp. 1-30.

[78] Loew, E.-M., 2016. *Analyse von Verbrennungsvorgängen im selbstzündungsdominierten Regime mittels Mischungsstatistik.* PhD Thesis, Technical University of Munich, Munich.

[79] He, G., Guo, Y., and Hsu, A. T., 1999. The effect of Schmidt Number on turbulent scalar mixing in a jet-in-crossflow. In *Proceedings of the ASME Turbo Expo*. Indianapolis, Indiana, USA, 99-GT-137.

[80] Paschereit, C. O., Schuermans, B., Polifke, W., and Mattson, O., 1999. Measurement of transfer matrices and source terms of premixed flames. *Journal of Engineering for Gas Turbines and Power, 124*(2), pp. 239-247.

[81] Fischer, A., Hirsch, C., and Sattelmayer, T., 2006. Comparison of multi-microphone transfer matrix measurements with acoustic network models of swirl burners. *Journal of Sound and Vibration, 298*(1-2), pp. 73-83.

[82] Bechert, D. W., 1980. Sound absorption caused by vorticity shedding, demonstrated with a jet flow. *Journal of Sound and Vibration, 70*(3), pp. 389-405.

[83] Eckstein, J., 2004. *On the mechanisms of combustion driven low-frequency oscillations in aero-engines.* PhD Thesis, Technical University of Munich, Munich.

[84] Åbom, M., 1992. A note on the experimental determination of acoustical two-port matrices. *Journal of Sound and Vibration, 155*(1), pp. 185-188.

[85] Åbom, M., and Bodén, H., 1988. Error analysis of two-microphone measurements in ducts with flow. *The Journal of the Acoustical Society of America, 83*(6), pp. 2429-2438.

[86] Lawson, C. L., 1995. *Solving least squares problems*. Society for Industrial and Applied Mathematics, Philadelphia.

[87] Dahlquist, G., 2008. *Numerical methods in scientific computing*. Society for Industrial and Applied Mathematics, Philadelphia.

[88] Kathan, R., 2013. *Verlustmechanismen in Raketenbrennkammern.* PhD Thesis, Technical University of Munich, Munich.

[89] Sujith, R. I., Waldherr, G. A., and Zinn, B. T., 1995. An exact solution for one-dimensional acoustic fields in ducts with an axial temperature gradient. *Journal of Sound and Vibration, 183*(4), pp. 389-402.

[90] Kumar, B. M., and Sujith, R. I., 1997. Exact solution for one-dimensional acoustic fields in ducts with a quadratic mean temperature profile. *The Journal of the Acoustical Society of America, 101*(6), pp. 3798-3799.

[91] Karthik, B., Kumar, B. M., and Sujith, R. I., 2000. Exact solutions to one-dimensional acoustic fields with temperature gradient and mean flow. *The Journal of the Acoustical Society of America, 108*(1), pp. 38-43.

[92] Mimani, A., and Munjal, M. L., 2012. Acoustical analysis of a general network of multi-port elements – an impedance matrix approach. *International Journal of Acoustics and Vibration, 17*(1), p. 23.

[93] Glav, R., and Åbom, M., 1997. A general formalism for analysing acoustic 2-port networks. *Journal of Sound and Vibration, 202*(5), pp. 739-747.

[94] Holmberg, A., Åbom, M., and Bodén, H., 2011. Accurate experimental two-port analysis of flow generated sound. *Journal of Sound and Vibration, 330*(26), pp. 6336-6354.

[95] Schuermans, B., 2005. *Modeling and control of thermoacoustic instabilities.* PhD Thesis, École Polytechnique Fédérale de Lausanne, Lausanne.

[96] Lauer, M., and Sattelmayer, T., 2009. On the adequacy of chemiluminescence as a measure for heat release in turbulent flames with mixture gradients. *Journal of Engineering for Gas Turbines and Power, 132*(6), p. 061502.

[97] García-Armingol, T., Ballester, J., and Smolarz, A., 2013. Chemiluminescence-based sensing of flame stoichiometry: Influence of the measurement method. *Measurement, 46*(9), pp. 3084-3097.

[98] García-Armingol, T., Hardalupas, Y., Taylor, A., and Ballester, J., 2014. Effect of local flame properties on chemiluminescence-based stoichiometry measurement. *Experimental Thermal and Fluid Science, 53*, pp. 93-103.

[99] Vogel, M., Bachfischer, M., Kaufmann, J., and Sattelmayer, T., 2021. Experimental investigation of equivalence ratio fluctuations in a lean premixed kerosene combustor. *Experiments in Fluids, 62*(5), pp. 1-14.

[100] Vogel, M., Bachfischer, M., Kaufmann, J., and Sattelmayer, T., 2022. Optical equivalence ratio measurement of a dual fuel burner for natural gas and kerosene. *Fluids, 7*(2), p. 43.

[101] Morrell, M., Seitzman, J., Wilensky, M., Lubarsky, E., Lee, J., and Zinn, B., 2001. Interpretation of optical emissions for sensors in liquid fueled combustors. In *39th Aerospace Sciences Meeting and Exhibit, American Institute of Aeronautics and Astronautics*, p. 787.

[102] Schuermans, B., Guethe, F., Pennell, D., Guyot, D., and Paschereit, C. O., 2010. Thermoacoustic modeling of a gas turbine using transfer functions measured under full engine pressure. *Journal of Engineering for Gas Turbines and Power, 132*(11), pp. 503-514.

[103] Lyra, S., Wilde, B., Kolla, H., Seitzman, J., Lieuwen, T. C., and Chen, J. H., 2014. *Structure and stabilization of hydrogen-rich transverse jets in a vitiated turbulent flow.* No. SAND2014-16144R. Sandia National Lab, Livermore, California, USA.

[104] Kolb, M., Ahrens, D., Hirsch, C., and Sattelmayer, T., 2013. Quantification of mixing of a reacting jet in hot cross flow using mie scattering. In *Lasermethoden in der Strömungsmesstechnik*.

[105] Dayton, J. W., Linevitch, K., and Cetegen, B. M., 2019. Ignition and flame stabilization of a premixed reacting jet in vitiated crossflow. *Proceedings of the Combustion Institute, 37*(2), pp. 2417-2424.

[106] Schulz, O., Piccoli, E., Felden, A., Staffelbach, G., and Noiray, N., 2019. Autoignition-cascade in the windward mixing layer of a premixed jet in hot vitiated crossflow. *Combustion and Flame, 201*, pp. 215-233.

[107] Balachandran, R., Ayoola, B., Kaminski, C., Dowling, A., and Mastorakos, E., 2005. Experimental investigation of the nonlinear response of turbulent premixed flames to imposed inlet velocity oscillations. *Combustion and Flame, 143*(1-2), pp. 37-55.

[108] Armitage, C. A., Balachandran, R., Mastorakos, E., and Cant, R. S., 2006. Investigation of the nonlinear response of turbulent premixed flames to imposed inlet velocity oscillations. *Combustion and Flame, 146*(3), pp. 419-436.

[109] Palies, P., Durox, D., Schuller, T., and Candel, S., 2011. Nonlinear combustion instability analysis based on the flame describing function applied to turbulent premixed swirling flames. *Combustion and Flame, 158*(10), pp. 1980-1991.

[110] Schimek, S., Moeck, J. P., and Paschereit, C. O., 2011. An experimental investigation of the nonlinear response of an atmospheric swirl-stabilized premixed flame. *Journal of Engineering for Gas Turbines and Power, 133*(10), p. 101502.